Ferrofluid Flow Phenomena

by

Thomas A. Franklin

Submitted to the Department of Electrical Engineering and Computer Science
in partial fulfillment of the requirements for the degree of
Master of Science in Electrical Engineering and Computer Science
at the

MASSACHUSETTS INSTITUTE OF TECHNOLOGY

June 2003

Signature of Author:.....
Department of Electrical Engineering and Computer Science
May 9, 2003

Certified by:.....
Markus Zahn
Professor of Electrical Engineering and Computer Science
Thesis Supervisor

Accepted by:.....
Arthur C. Smith
Chairman, Department Committee on Graduate Students

Ferrofluid Flow Phenomena

by

Thomas A. Franklin

Submitted to the Department of Electrical Engineering and Computer Science
on May 9, 2003 in Partial Fulfillment of the
Requirements for the Degree of Master of Science in
Electrical Engineering and Computer Science

ABSTRACT

An investigation of ferrofluid experiments and analysis is presented in three parts: a characterization of ferrofluid properties, a study of ferrofluid flow in tubing and channel systems, and a study of ferrofluid free surface sheet flows.

The characterization of ferrofluid samples is completed through analysis of magnetization curves measured with a vibrating sample magnetometer. Determination is made of the ferrofluid particle size range, saturation magnetization, low-field magnetic permeability, and magnetic volume fraction. The experimental results are well described by the Langevin theory of paramagnetism. A detailed discussion of the demagnetization factor within the ferrofluid sample is also included.

Ferrofluid flow through circular tubing in a laminar regime is examined as a function of the applied magnetic field magnitude, direction, and frequency. Gradients within the applied magnetic field create a magnetic contribution to the pressure drop across a length of tubing. Experiments of ferrofluid flow through a rectangular channel with a free surface when driven by a rotating spatially uniform magnetic field exhibit an anti-symmetric flow profile across the channel width, with a net zero flow rate, consistent with theoretical work of previous research.

The first known investigation of ferrofluid free surface sheet flows resulting from a ferrofluid jet impacting a small circular plate is presented. Two distinct magnetic field orientations relative to the incident jet and resulting sheet are examined, producing markedly different results. A magnetic field oriented perpendicular to the jet flow is found to deform the jet cross-section from circular toward an elliptical shape thereby causing the sheet to also change from circular to elliptical, but with the long axis of the sheet oriented perpendicularly to the long axis of the jet cross-section. In the case of a magnetic field applied everywhere perpendicular to the sheet flow a significant decrease in sheet radius is observed. The cause of the decrease in sheet radius is a magnetic field induced decrease in ferrofluid pressure as well as a magnetic field enhanced convective Kelvin-Helmholtz instability. A thorough theoretical development describes the observed phenomena.

Thesis Supervisor: Markus Zahn
Title: Professor of Electrical Engineering and Computer Science

Contents

Acknowledgements

Many more people than can be listed here deserve a lot of thanks for helping in the completion of this work. Thanks especially to my advisor, Markus Zahn, for his help and input on all of my work, as well as his wide range of advice. I am grateful for the amount of time he spent reading and correcting this thesis. He also teaches some wonderful courses. Thank you to John Bush for his considerable effort with the sheet experiments, as well as for teaching a great fluid dynamics class. I am grateful for the help of Adam Rosenthal, Xiaowei (Tony) He, Carlos Rinaldi, Wayne Ryan, and Anders Helgeson, as well as the many other members of my lab group.

The use of two separate VSM machines was provided by Dr. Caroline Ross, and Dr. Robert O'Handley. Also, David Bono offered many helpful discussions regarding interpretation of the data. Adam Rosenthal and Xiaowei He assisted in collection of the mass density data. José Bico helped in the collection of the surface tension data. The use of the cone viscometer was provided by Suraj Deshmukh.

A special thanks to Dr. Raj and colleagues from Ferrotec Corporation for supplying the various ferrofluids used in this work, and to the National Science Foundation for support through Grant # CTS-0084070.

Thank you to all of my family.

Thanks so very much to Elise for constant support and an incredible ability to listen to all my ideas and questions. It has always been fun!

Chapter 1

Introduction to Ferrofluids

1.1 Background

Ferrofluids are stable colloidal suspensions consisting of single-domain magnetic particles coated with a surfactant and immersed in a carrier fluid. The particles are commonly magnetite and of order 10 nm in diameter, while the carrier liquid is typically an oil or water base. Ferrofluids are of particular interest since there are no known naturally occurring magnetic liquids, and in distinction from magnetohydrodynamics the flow phenomena occur without the need for electrical current, and thus in the absence of corresponding Lorentz forces. Developed in the 1960s, the suspensions exhibit strong magnetic behavior while retaining fluid characteristics under the influence of a strong magnetizing field [1]. One common method for production of ferrofluids is to grind micron-sized magnetite particles for 500-1000 hours in a ball mill in the presence of the surfactant and carrier fluid until the particles reach the desired nanometer-range size [2]. A more efficient method of production is to chemically precipitate the particles, with the necessary chemical reaction given by [2]

$$2\mathrm{Fe}^{3+} + \mathrm{Fe}^{2+} + 8\mathrm{OH}^{-} = \mathrm{FeOFe_2O_3} + 4\mathrm{H_2O}. \tag{1.1}$$

Ferrofluids have been used in applications ranging from liquid seals, dampers, and drug-delivery agents, to sink-float systems for separation of materials. The fluids are generally opaque and frequently very difficult to clean from surfaces they may contact, although recent work reports the synthesis of optically transparent and colored ferrofluids [3, 4]. Most current applications employ static magnetic fields although the effects of alternating and rotating fields are being used to investigate future applications. Of particular interest is the possibility of using ferrofluids in microelectromechanical systems (MEMS)[5], the subject of current research by this author, which motivates much of the work discussed in this thesis.

The magnetic particles within ferrofluids are modeled as a collection of non-interacting magnetic dipoles. The typical diameter of a single particle is 10 nanometers (nm) when the shape is estimated as a sphere, although there can be a range of sizes from 5 to 15 nm [6]. Ferrofluids are stable colloids because the Brownian motion of the particles enables them to resist gravitational settling over time periods of days to years depending on the exact particle size and the physical properties of the carrier fluid. In theory, the particles are also free of agglomeration due to the electrostatic and steric hindrance provided by the surfactant, although in practice lesser quality fluids are prone to the formation of longer chains when exposed to a magnetic field, as can be identified with an electron microscope scan [6]. Current research interest of ferrofluids is driven in part by the many phenomena ferrofluids display when exposed to various alternating current (ac) and direct current (dc) produced magnetic fields. Examples of these ferrohydrodynamic phenomena include reduced or enhanced magneto-viscosity, and forward and reverse pumping in rotating magnetic fields [7, 8]. Additional phenomena include ferrofluid peaking [9], fingering [10, 11] and labyrinth [12] pattern formations occuring when ferrofluid surfaces are exposed to magnetic fields of

different spatial orientations [1, 13]. Recent work by researchers at MIT in the Laboratory for Electromagnetic and Electronic Systems (LEES) has also uncovered new behavior and pattern formations of magnetically induced rotating ferrofluid layers in a Hele-Shaw geometry which confines the flow to two dimensions in the small gap between flat parallel plates [14].

1.2 Ferrofluids and Nanoscience

Ferrofluids are the subject of increased scientific interest in the last several years, and yet there remains a lack of extensive research and application of ferrofluids in situations where they are exposed to external alternating and rotating magnetic fields. Furthermore, although many new uses of ferrofluid have been proposed in areas as varied as biomedical devices and nanomaterial manipulation, few of the proposals have met with wide-scale implementation, and as such most technological uses include the traditional applications of liquid seals, dampers, and heat transfer agents. Meanwhile, many researchers continue to study the production of the nanoparticles and fluids with the intent of tailoring the colloid properties for specific applications.

A growing number of researchers have begun to appreciate the potential for ferrofluid applications in the quickly emerging fields of microelectromechanical systems (MEMS) and nanoelectromechanical systems (NEMS), due to the 10 nm spherical diameter of the permanently magnetized particles. This size scale naturally makes ferrofluids a viable option for adaptation to MEMS and NEMS devices.

1.3 Ferrofluids in Time-Varying Magnetic Fields

1.3.1 Ferrofluid Torque Production

The behavior of ferrofluids in alternating and rotating magnetic fields can be vastly different than in dc fields because there exists a phase lag between the magnetization of the ferrofluid particles and the applied magnetic field, so that unlike the dc case the magnetization is not collinear with the applied magnetic field. This non-alignment of the magnetic field and magnetic moment results in a body torque on the ferrofluid. The body torque results in the magnetic stress tensor having a non-symmetric part. Physically, the ferrofluid particles individually experience a magnetic torque, $\vec{\Gamma} = \mu_o \vec{M} \times \vec{H}$, given by the cross product of the particle's permanent magnetization and the time-varying magnetic field. The ensuing dynamics are dependent upon the speed with which the particles can rotate into alignment with the field, known as the magnetic relaxation characteristic, and the frequency of the applied magnetic field. The net torque generated within the ferrofluid due to the torque on the individual particles may be measured with the use of an appropriate shear rate viscometer [15, 16]. Under appropriate conditions the fluid may co-rotate or counter-rotate with an applied rotating field [16]. Additionally, consideration must be given to the boundary conditions on the rotating magnetic particles at a solid boundary. Thus, a large part of theoretical ferrohydrodynamics is now directed toward developing and understanding the ferrofluid relaxation equations, boundary conditions, and the role of surface and volume torques.

1.3.2 Microfluidic Devices Utilizing Ferrofluids in Time-Varying Magnetic Fields

The rich behavior of ferrofluids in time-varying magnetic fields suggests potential applications to the field of microfluidic devices. The ability to control flow direction and velocity may find application in microfluidic pumps and microfluidic mixers, functioning without the need for mechanical parts. Researchers at Harvard have already shown that magnetic nanoparticles, similar to those in ferrofluids, can respond to the magnetic fields created by microfabricated wires [17]. Since fabrication of wires is commonplace in MEMS devices the implementation of magnetic fields to control fluid motion may prove advantageous over the complication of fabricating mechanical valves and channels. With the recent development of MEMS magnetic induction motors the possibility of creating time-varying fields on a MEMS scale has become a reality that may prove useful in ferrofluid manipulation [18].

1.4 Overview of Thesis

Through the use of several experimental investigations and the corresponding theory the current work examines ferrofluid dynamics. Although the experiments described are conducted on the macro-scale, the intent of much of this work is to evaluate possible applications of ferrofluids to nanotechnology, and comments along this line are given when appropriate.

Chapter 1 has provided a brief overview of ferrofluid history along with several basic definitions needed to understand the material presented in the later chapters. Chapter 2 covers the experimental magnetization results and characterization of the ferrofluid samples used throughout the course of the work. The experimental data are used to calculate the magnetic particle diameter range, magnetic permeability, magnetic volume fraction, and

saturation magnetization using electromagnetic and paramagnetic Langevin theory. Three methods of calculating the sample demagnetization factor based on the experimental data are investigated and shown to produce inconsistent results due to the requirement for extremely high accuracy of the experimental data. Chapter 3 then details an investigation into ferrofluid behavior when confined to flow through circular tubing exposed to dc and 60 Hz oscillating magnetic fields oriented parallel and transverse to the tube axis. The collected data indicate that a spatially symmetrical applied magnetic field does not change the flow rate, while a gradient field can reduce or increase the pressure drop required to maintain a particular flow rate. These results are in contrast to previously reported work [19]. A qualitative investigation of a free surface channel flow is also described, which indicates that wall effects play a large role in the flow dynamics, with a resulting counter-flow in each half of the channel that creates a zero net flow rate, in accordance with theoretical predictions [20]. Chapter 4 presents data from the first known experiments of ferrofluid free surface sheet flows, and provides new examples of visually striking ferrofluid flow patterns. Qualitative as well as quantitative experimental data is compared to predictions derived from ferrohydrodynamic theory. Finally, Chapter 5 discusses future work and potential applications of ferrofluids based on the results of this thesis. The appendices are used to include tables and figures of experimental data described in this thesis, as well as to provide operating instructions for a few of the instruments employed in the data collection.

Units and Symbols

This thesis generally uses SI units, but on occasion employs other unit systems which are more conventionally used. Unit conversions are provided where appropriate, along with tables of units in Appendix D. A warning about the symbols used: some symbols represent

different parameters in different sections. Note the context in which the symbol is being used.

Chapter 2

Ferrofluid Magnetization

Magnetization data for five ferrofluid samples was collected using a vibrating sample magnetometer (VSM, ADE Technologies model 880 Digital Measurement System). Calculations of fluid parameters and computer aided data fitting are completed assuming the Langevin relationship for paramagnetic behavior to be the governing equation of ferrofluid magnetization. Corrections to the Langevin equation as suggested by previous researchers are considered but do not significantly change the analysis. It is concluded that magnetization curves provide a reasonably accurate method in which to determine the saturation magnetization, magnetic particle volume fraction, magnetic permeability, and magnetic particle diameter range of a ferrofluid sample. Comparison between theoretical and calculated demagnetizing factors for the sample holder shows the need for extremely accurate measurements of fluid parameters, notably particle size.

2.1 Introduction

When a paramagnetic or ferromagnetic material is stressed by a magnetic field the magnetic dipoles within the material will attempt to align their magnetic dipole moment parallel to

the direction of the applied field. Ferromagnetic materials display a strong magnetic interaction between neighboring molecules, while paramagnetic materials display only weak interactions between neighboring material molecules. Paramagnets have a negligible magnetic field in the absence of applied magnetic fields. In either case, when exposed to an external magnetic field the dipoles are aligned and the material is thus described as being magnetized, meaning that it produces a net magnetic field in addition to the applied external magnetic field. A measure of the magnetization of a material as a function of the applied magnetic field can be represented in a magnetization curve. Experimental magnetization data for five ferrofluid samples obtained from Ferrofluidics Corporation (now Ferrotec Corporation) were completed along with analysis to determine the magnetic particle diameter range, magnetic permeability, magnetic volume fraction, saturation magnetization, and demagnetization factors of each sample. The samples, four fluids and one wax with a melting point of 70^o C, are compared to the Langevin equation for paramagnetic behavior, which details the magnetization of a paramagnetic sample stressed by an external magnetic field with simultaneous thermal realignment. The samples tested and their nominal saturation magnetization values are: 400 Gauss EFH1 hydrocarbon-based, 400 Gauss NF 1634 Isopar M-based, 162 Gauss MSG W11 water-based, NBF 1677 'display cell' fluorocarbon-based, and 550 Gauss NF 1273 wax ferrofluid. In reference to NF 1634, the liquid carrier Isopar, chemical name coparaffinate, is similar to kerosene, and is obtained by oxidizing petroleum hydrocarbons [21, p. 325]. The saturation magnetization values listed are those given by Ferrofluidics Corporation and are more accurately measured and described in section 2.6.

2.2 Magnetization Theory

Theoretical magnetization curves for ferrofluid samples are derived from the assumption that ferrofluids consist of a collection of individual, non-interacting, magnetic dipoles. The final form for the magnetization as a function of magnetic field, known as the Langevin relation for paramagnetic behavior, is found beginning with the torque $\vec{\Gamma}$ and the energy W of a magnetic dipole with moment $\vec{m}$ at an angle θ to a magnetic field $\vec{H}= H_o\hat{z}$ [22, p. 354]

$$\vec{\Gamma}= \mu_o \vec{m} \times \vec{H}= \mu_o m H \sin\theta \tag{2.1}$$

where $\mu_o = 4\pi \times 10^{-7}$ Henry/m is the magnetic permeability of free space, and θ is the angle between the magnetic dipole moment and the magnetic field. The energy of the particle is equal to the mechanical work required to rotate the particle through the angle θ

$$W = \int_0^\theta \Gamma d\theta = -m\mu_o H[\cos\theta - 1]. \tag{2.2}$$

Although the dipole moment tends to align itself with the field there is an additional thermal energy which counteracts this behavior and provides a randomizing spatial orientation. From thermodynamics the situation can be described using Boltzmann statistics which take the form

$$n = \hat{n}e^{-W/kT} \tag{2.3}$$

in which n is the number density of dipoles, $k = 1.38 \times 10^{-23}$ J/K is Boltzmann's constant, and T is the temperature in kelvin. Substitution of (2.2) in (2.3) leads to the number density of dipoles, n, with the energy given by (2.2)

$$\begin{aligned} n &= \hat{n}e^{-m\mu_o H/kT}e^{m\mu_o H\cos\theta/kT} \\ \Longrightarrow n &= n_o e^{m\mu_o H\cos\theta/kT} \end{aligned} \tag{2.4}$$

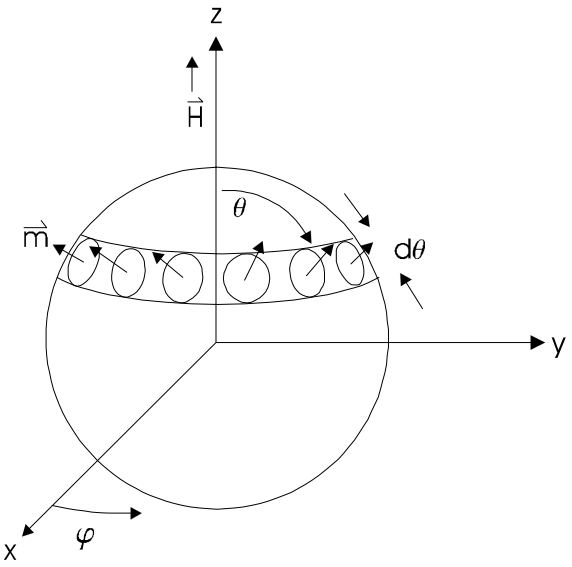

Figure 2.1: All dipoles within the volume of a sphere contribute to the net magnetization of a body.

where $n_o = \hat{n}e^{-m\mu_o H/kT}$ represents the amplitude of the number density of magnetic dipoles when the magnetic field is zero. Integrating over a sphere of radius R enclosing many magnetic dipoles and dividing by the volume of the sphere gives the average number density of dipoles as

$$N = \frac{1}{\frac{4}{3}\pi R^3}\int_{\theta=0}^{\pi}\int_{\varphi=0}^{2\pi}\int_{r=0}^{R} n_o e^{m\mu_o H\cos\theta/kT} r^2\sin\theta dr d\varphi d\theta = \frac{n_o}{\alpha}\sinh\alpha \tag{2.5}$$

where φ is the angle from the x-axis in the x-y plane, and $\alpha = (m\mu_o H)/kT$.

The net magnetization will be parallel to the direction of the applied magnetic field as shown in Figure 2.1, since it is recognized that the magnetization in the x and y directions will average to zero over the sphere. The differential expression for the z-directed magnetization, M_z, is

$$dM_z = \frac{mn}{\frac{4}{3}\pi R^3}\cos\theta r^2\sin\theta dr d\theta d\varphi. \tag{2.6}$$

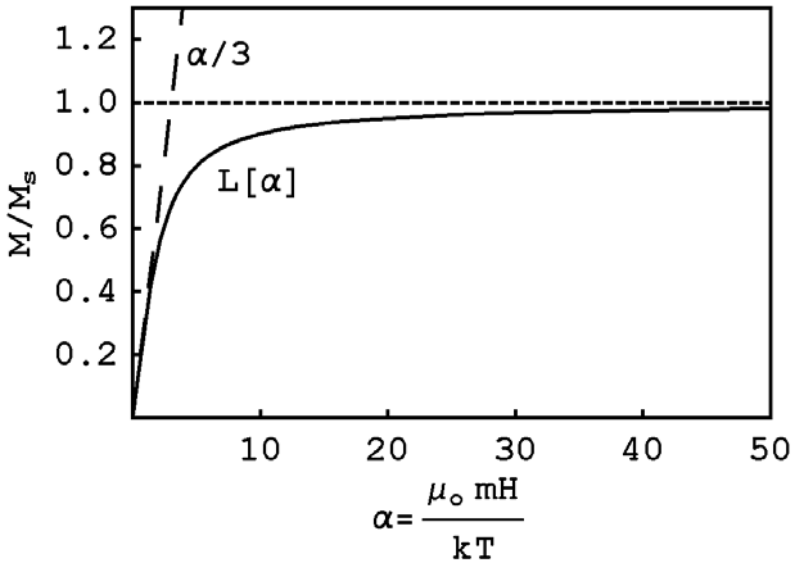

Figure 2.2: The theoretical Langevin equation of (2.7) is plotted with low and high-field asymptotes (dashed lines).

Using n as defined in (2.4) and integrating (2.6) over the volume of the sphere results in

$$\frac{M}{\phi M_d} = \frac{M}{M_s} = L(\alpha) = \coth(\alpha) - \frac{1}{\alpha} \tag{2.7}$$

where M and H both point in the $\hat{z}$ direction, ϕ is the volume fraction of magnetic solid to carrier liquid and surfactant, M is the magnetization, $M_d = \dfrac{m}{V}$ is the domain magnetization of the bulk magnetic particle with volume V and magnetic dipole moment m, and $M_s = \phi M_d$ is the saturation magnetization of the ferrofluid which corresponds to all dipoles being aligned with the field. Eq. (2.7) is known as the Langevin equation for paramagnetic behavior. We use $V = \frac{1}{6}\pi d^3$ where d is the diameter of the magnetic particle which is assumed spherical. For magnetite, $\mu_o M_d$ is 5600 Gauss = 0.56 Tesla, or equivalently $M_d = 446$ kA/m [1]. The Langevin function is plotted in Figure 2.2 and has both low-field and high-field asymptotes

written respectively as

$$\lim_{\alpha \ll 1} L(\alpha) = \frac{M}{M_s} \approx \frac{\alpha}{3} = \frac{\pi}{18} \frac{\mu_o M_d H d^3}{kT} \tag{2.8}$$

$$\lim_{\alpha \gg 1} L(\alpha) = \frac{M}{M_s} \approx 1 - \frac{1}{\alpha} = \left(1 - \frac{6}{\pi} \frac{kT}{\mu_o M_d H d^3} \right). \tag{2.9}$$

In (2.8) the magnitude of the dipole moment, $m = \frac{1}{6} M_d \pi d^3$, has been rewritten in terms of the domain magnetization and the particle volume, assuming a spherical particle, where d represents the magnetic diameter of the particle. It is also useful to note that $M_s = \phi M_d$ can be used to relate the domain and saturation magnetization.

The low-field limit, (2.8), describes a linear relationship between the magnetization, M, and the field, H. Examination of (2.8) shows the same approximation is accurate at high temperatures. The initial slope of the magnetization curve, χ, is the magnetic susceptibility and is given as

$$\chi = \frac{M}{H} = \frac{\pi}{18} \frac{\mu_o M_s M_d d^3}{kT} = \frac{\pi}{18} \frac{\mu_o \phi M_d^2 d^3}{kT}. \tag{2.10}$$

The susceptibility describes the magnitude of magnetic response shown by a magnetic material at low field strengths. A large value of χ corresponds to strongly magnetic material, while a small value corresponds to a weakly magnetic material. Free space has a value of $\chi = 0$. The magnetic susceptibility is related to the more frequently used magnetic permeability by

$$\mu = (1 + \chi)\mu_o. \tag{2.11}$$

The magnetic susceptibility defined in (2.10) can be rewritten as

$$\chi = \frac{\pi}{18} \phi \frac{\mu_o M_d^2 d^3}{kT} = \frac{q}{T} \Longrightarrow q = \frac{\pi}{18} \phi \frac{\mu_o M_d^2 d^3}{k} \tag{2.12}$$

where several parameters are combined into q so as to focus on the inverse temperature dependence. Shliomis, however, proposed a correction to (2.12), claiming that dipole interactions must be included when the magnetic volume fraction of the sample is large, approximately 10% or greater [23],

$$\frac{\chi(2\chi+3)}{\chi+1} = \frac{\pi}{6}\phi\frac{\mu_o M_d^2 d^3}{kT}. \tag{2.13}$$

The methodology leading to the form of this correction is similar to a Debye-Onsager theory of polar liquids [24]. In the limit $\chi \ll 1$ (2.13) simplifies to (2.12).

Analysis of (2.10) also lends itself to determination of the particle size within the colloid by rearranging to solve for d. This can be helpful since M_s, T, and χ can be found experimentally, and all other parameters are known constants. Therefore, by determining the value of χ experimentally we can determine the magnetic particle diameter, assuming the shape of the particle to be spherical [1]

$$d = \left[\frac{18\chi kT}{\mu_o M_s M_d \pi}\right]^{\frac{1}{3}}. \tag{2.14}$$

Calculation of the particle diameter in this manner corresponds to the particle diameter of magnetic material. When discussing ferrofluids there are two different values of particle size to consider. The first is the magnetic particle size, which describes the size of the magnetically active portion of a solid particle. The second is the physical solid particle size, which consists of the magnetic particle as well as a layer of surfactant. The surfactant generally adds 2 nm to the radius of the magnetic particle alone [25]. When considering a sample with a particle size distribution, as is found in ferrofluids, it is the largest particle sizes that most contribute to the value of χ.

The high-field limit of the Langevin equation, (2.9), can be used to approximate the

diameter of the smaller particles. Alternatively, a low temperature can also be used to work within the same regime. The high-field region is also known as the saturation region because it describes the approach to a saturation value of magnetization at which point most of the dipoles have aligned with the magnetic field. The temperature dependence of the saturation magnetization, $M_s = \phi M_d$, is assumed negligible in this thesis because most of the experiments are done at or near room temperature. Furthermore, the magnetic volume fraction is calculated from (2.7) as

$$\phi = \frac{M_s}{M_d}. \tag{2.15}$$

Thus, a single magnetization curve can provide information on the magnetic permeability, μ, in the low-field Langevin regime; saturation magnetization, M_s; the magnetic volume fraction, ϕ, and the range of particle diameter d of the ferrofluid.

The low and high-field asymptotes of the Langevin equation therefore produce estimates of the upper and lower bounds of the particle diameter range within the fluid [1]. The magnetization behavior of the low-field regime is dominated by the largest particles, while that of the high-field regime is dominated by the smallest particles.

2.3 Magnetic Relaxation Theory

The particle size range within ferrofluids is important since magnetic relaxation mechanisms are strongly dependent on particle size. The two dominant mechanisms through which the ferrofluid particle magnetic moment may align with the applied magnetic field are Brownian motion, which is the physical rotation of the particle into alignment with the field, and Néel relaxation, which is characterized by the movement of the particle magnetic moment relative to the crystal axis. These two processes are sketched in Figure 2.3. The characteristic

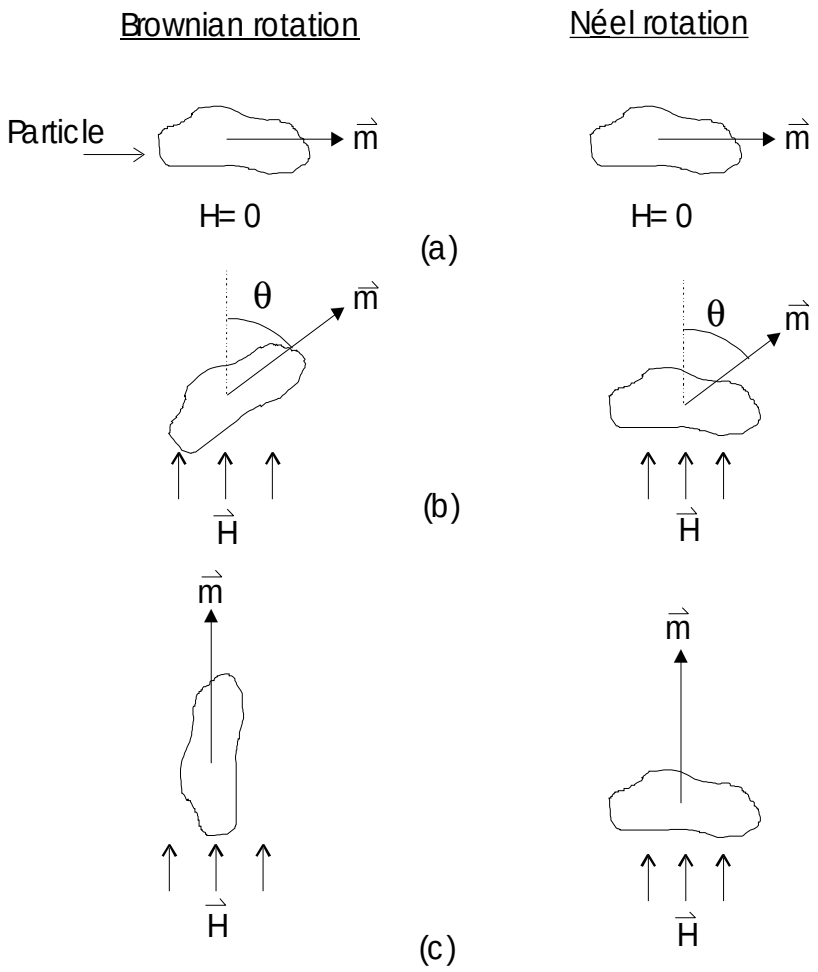

Figure 2.3: Brownian relaxation compared to Néel relaxation for a magnetic particle with magnetic dipole moment $\vec{m}$ (a) with no applied magnetic field, (b) relaxing under the influence of an applied magnetic field at angle θ to $\vec{m}$, and (c) after relaxation is complete so that $\vec{m}$ is parallel with $\vec{H}$. Throughout this thesis we assume that ferrofluid particles are spherical; the particles depicted here are non-spherical for ease of visualizing the relaxation processes.

relaxation times for each are [1]

$$\tau_B = \frac{3V_B\eta_o}{kT} \text{ Brownian relaxation time} \tag{2.16}$$

$$\tau_N = \frac{1}{f_o}e^{\frac{KV_N}{kT}} \text{ Néel relaxation time} \tag{2.17}$$

for which η_o, f_o , and K are the carrier fluid dynamic viscosity, the frequency constant of Néel relaxation, and the anisotropy constant of the particle, respectively. The two particle volumes V_B and V_N are given by

$$V_B = \frac{4}{3}\pi(R+\delta)^3 \text{ Brownian particle size} \tag{2.18}$$

$$V_N = \frac{4}{3}\pi R^3 \text{ Néel particle size.} \tag{2.19}$$

In (2.18) δ represents the thickness of the adsorbed surfactant layer, and $R = d/2$ is the magnetic particle radius. The relaxation times defined in (2.16) and (2.17) are typically on the order of $10^{-5} - 10^{-9}$ seconds [1].

The effective relaxation time for ferrofluid particles can be derived by considering that both the Brownian and Néel processes act simultaneously. When both mechanisms play a role in the relaxation process the effective time constant is

$$\frac{1}{\tau_{eff}} = \frac{1}{\tau_B} + \frac{1}{\tau_N} \Longrightarrow \tau_{eff} = \frac{\tau_B\tau_N}{\tau_B + \tau_N}. \tag{2.20}$$

A plot of the three relaxation times as a function of particle diameter is shown in Figure 2.4, which indicates that the smallest time constant dominates the physical process of relaxation. For small particles Néel relaxation is faster than Brownian, and so the Néel time constant

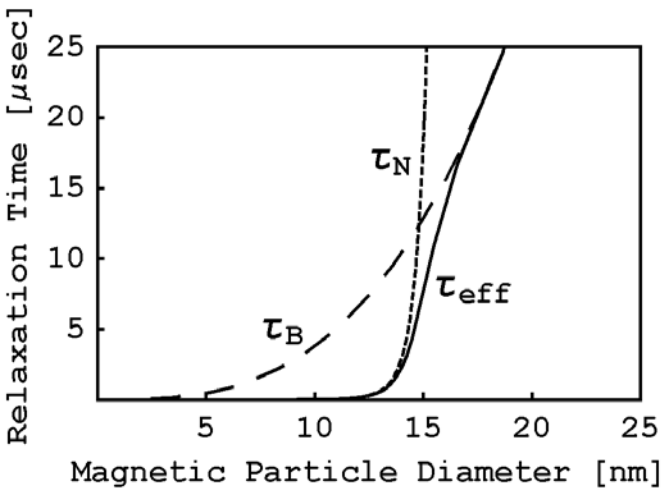

Figure 2.4: The Brownian, Néel, and effective relaxation time constants as a function of spherical magnetic particle diameter. The plots correspond to EFH1 hydrocarbon-based ferrofluid, with the corresponding fluid parameters: the fluid mass density $\rho = 1169$ kg/m^3, the dynamic viscosity $\eta_o = 10$ cP, the anisotropy constant $K = 23,000$ J/m for magnetite, the temperature $T = 300$ K, and the frequency constant, $f_o = 10^9$ Hz. The Brownian plot assumes zero surfactant thickness, $\delta = 0$.

dominates τ_{eff}. For large particles the Brownian relaxation is faster than Néel relaxation, and so the Brownian time constant dominates τ_{eff}.

2.4 Demagnetization Theory

2.4.1 Internal Magnetic Field

All equations discussed to this point take the magnetic field, $\vec{H}$, to be the field inside the ferrofluid sample. Experimentally, however, the VSM produces an applied external field, $\vec{H}_e$, in the air gap in which the sample is placed, and so it is necessary to determine the value of the field inside the sample by relating it to the applied field. More specifically, the VSM operates by applying an external static magnetic field in which the sample is mechanically

forced to vibrate, therefore producing an induction field $\vec{B}= \mu_o \left(\vec{H} + \vec{M} \right)$ which is measured by a pair of sensing coils. The magnetic field inside the magnetic material differs from the applied field by inclusion of a sample-shape dependent scalar demagnetization factor D

$$\vec{H_i}=\vec{H_e} - \vec{M} \cdot D \tag{2.21}$$

where $\vec{H_i}$ is the field inside the material, $\vec{H_e}$ is the externally applied field, and $\vec{M}$ is the magnetization.

2.4.2 Demagnetization Factor

A theoretical demagnetization factor was estimated for the ferrofluid magnetization measurements by approximating the cylindrical sample container to be an oblate ellipsoid with two equal major axes, s, both n times a minor axis b. The ratio $n = s/b$ is equal to 2.4 for the sample container used in the VSM measurements as illustrated in Figure 2.5(a). The applied field is assumed parallel to one of the major axes as shown in Figure 2.5(b). A calculated demagnetization factor can then be determined using the corresponding equation adapted from Bozorth [26, p. 849], which is derived from geometrical considerations

$$D = \frac{1}{2} \left[\frac{n^2}{(n^2-1)^{3/2}} \arcsin \frac{\sqrt{n^2-1}}{n} - \frac{1}{n^2-1} \right]. \tag{2.22}$$

A plot of (2.22) is given in Figure 2.6. It is noted that as the major axis, s, of the ellipsoid becomes infinite, so too does $n = s/b$, with the demagnetizing factor decreasing toward zero. The demagnetization factor summed over three orthogonal axes must equal 1. The simplest demonstration of this principle is to consider a sphere, which has symmetry over all three axes and thus a demagnetizing factor of 1/3 in each direction. This result can be recovered

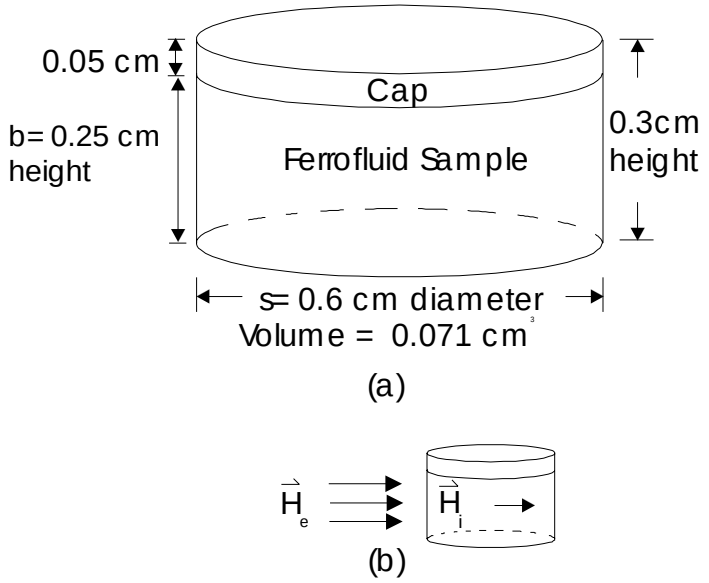

Figure 2.5: (a) The plastic sample container used in magnetization experiments (inner dimensions). (b) The approximate oblate ellipsoid geometry of the container as seen by the applied magnetic field, $\vec{H}_e$.

from (2.22) in the limit as $n \to 1$. In the present discussion $n = 2.4$, so that (2.22) gives an approximate value of $D \approx 0.211$.

2.4.3 Experimental Measurement of D

Three methods for calculating D using the experimental magnetization data were investigated. The methodology exploits the fact the D is dependent on sample shape while being independent of temperature, T. The calculation of D from experimentally measured quantities, described in section 2.10, was found to be unsuccessful due to a high sensitivity of the developed calculations on physical parameters, such as the particle diameter, which was only known to ± 1 nm. In the future, with more accurate experimental measurements than those currently available, the theory developed here may prove useful.

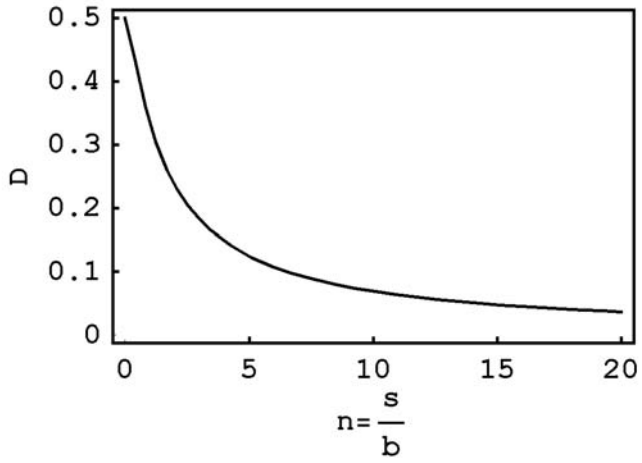

Figure 2.6: Dependence of the demagnetization factor on n, the ratio of major axis, s, to minor axis, b, for an oblate ellipsoid given by (2.22).

Magnetization Measurements at Two Temperatures

We begin from (2.10)

$$\chi = \frac{M}{H_i} \tag{2.23}$$

$$\chi_e = \frac{M}{H_e} \tag{2.24}$$

where H_i and H_e are the internal and external magnetic fields, and are related by (2.21). The value of χ, as discussed until now, represents the true magnetic susceptibility of the material, while χ_e is the value corresponding to the uncorrected magnetic field values and has no physical significance. However, χ_e is useful since it can be taken directly from the experimentally measured magnetization curve of M vs. H_e. Combining (2.23) and (2.24) and using (2.21) χ and χ_e can be related by

$$\chi = \frac{\chi_e}{1 - \chi_e \cdot D}. \tag{2.25}$$

Using (2.25) in (2.12) we obtain

$$\frac{\chi_e}{1-\chi_e \cdot D} = \frac{q}{T}. \tag{2.26}$$

Assuming negligible changes in q over the range of temperatures examined allows comparison of data taken at two separate temperatures, resulting in calculation of D as follows

$$\frac{\left(\frac{\chi_{e1}}{1-\chi_{e1}\cdot D}\right)}{\left(\frac{\chi_{e2}}{1-\chi_{e2}\cdot D}\right)} = \frac{\left(\frac{q}{T_1}\right)}{\left(\frac{q}{T_2}\right)} \Longrightarrow D = \frac{\frac{T_1}{\chi_{e2}} - \frac{T_2}{\chi_{e1}}}{T_1 - T_2}. \tag{2.27}$$

Eq. (2.27) is useful since it only requires knowledge of easily measurable quantities, and does not require an extensive knowledge of the material being examined.

Using the Measured χ_e

Alternatively, D can be found by solving (2.26) directly as long as all of the parameters in q are known

$$D = \frac{1}{\chi_e} - \frac{T}{q}. \tag{2.28}$$

Large Magnetic Volume-Fraction Correction

A third method for calculating D is to use Shliomis' correction for the low-field magnetic susceptibility, (2.13), combined with (2.25), resulting in a quadratic equation in D

$$D^2\left[\frac{3q}{T}\chi_e^2\right] + D\left[\chi_e^2\left(3-\frac{3q}{T}\right) - \frac{6q}{T}\chi_e\right] + \left[-2\chi_e^2 + \chi_e\left(\frac{3q}{T}-3\right) + \frac{3q}{T}\right] = 0. \tag{2.29}$$

Values of D are computed in the following section with each of the above three methods.

2.5 VSM Measurement Results

Experimental trials were completed for three of the four liquid ferrofluid samples (NF 1634 Isopar M, MSG W11, and NBF 1677), in which the magnetization was recorded over the entire magnetic field range from negative to positive saturation, and over the low-field range to determine the magnetic susceptibility. In the saturation regime trials the applied magnetic field was set in the negative saturation range and increased in steps of 200 Oersteds (Oe = A/m) to positive saturation, and then stepped back down to negative saturation. In the low-field regime, data was taken from -10 Oe to 10 Oe in steps of 1 Oe. For the wax ferrofluid, NF 1273, only the low-field trials were carried out since the sample container leaked after the trial and was not able to be refilled. For these four ferrofluid samples, the low-field data was taken at three separate, though not identical, temperatures to facilitate comparison to Langevin theory and in calculation of demagnetization factors with (2.27)-(2.29). The magnetization measurement of EFH1 ferrofluid was completed several months after the other four samples, and so the method was modified based on the knowledge obtained from working with the other four samples. Specifically, magnetization data of EFH1 was taken from zero magnetic field up to positive saturation. Negative magnetic field values were not tested since the previous samples showed no signs of hysteresis. The magnetic field step size was 1 Oe in the low-field range, progressing to a step size of 20 Oe in the middle-field range, and finishing with a step size of 200 Oe in the saturation range. Thus, with a single measurement, all the data needed to calculate the magnetic parameters of the fluid was collected.

The measured fluid mass densities of each sample are shown in Table 2.1. The density values were determined experimentally by filling a calibrated container with a known volume

Measured Mass Densities of Fluid Samples		
Fluid Sample	**Density** (g/cm^3)	**Error** ($\pm\%$)
NF 1634 Isopar M (400 Gauss)	1.18	6.0
MSG W11 water-based (162 Gauss)	1.204	1.0
NF 1273 wax ferrofluid (550 Gauss)	1.41	4.0
NBF 1677 Display Ferrofluid (fluorocarbon-based)(400 Gauss)	1.97	4.0
EFH1 hydrocarbon-based (400 Gauss)	1.169	1.0

Table 2.1: Measured mass densities of the fluid samples used in collection of the magnetization data. The nominal saturation magnetization values of each sample are also given. The experimental errors in the mass measurements and volume measurements needed for the calculation of the densities were combined into the listed error in density. The method of combining the errors is explained in Appendix B.3

of the sample and weighing the mass of the filled container using an electronic scale (Denver Instrument Company Model S-110). By subtracting off the mass of the empty container the sample mass and volume are known, allowing calculation of the density using $\rho = \frac{\text{Mass}}{\text{Volume}}$. The values listed in Table 2.1 with an error of 1% were measured using a larger sample volume than the other fluids, thus giving a smaller volume measurement error which produces a smaller error in the density calculation. These results are therefore listed to one decimal place greater accuracy than are the samples measured using a smaller volume. All ferrofluid density values fell within the broad range listed in the ferrofluid data sheets provided by Ferrofluidics Corporation. Also included in Table 2.1 are the nominal saturation magnetization values provided by Ferrofluidics Corporation as used to identify the fluids.

The VSM provides the magnetization values in units of the electromagnetic unit (e.m.u.). The sample volume in cubic centimeters is necessary in conversion of the magnetic moment from e.m.u into Gauss, as follows [27]

$$\frac{\text{e.m.u}}{\text{volume in cubic centimeters}} 4\pi = \text{Gauss}. \tag{2.30}$$

In preparation of collecting the magnetization data, each sample container was filled and the mass of the fluid was measured using the previously mentioned Denver Instruments electronic scale. Using the appropriate density value from Table 2.1 the volume of the sample was calculated and was used in (2.30) to determine the magnetization in units of Gauss from e.m.u. The decision to use this calculated volume as opposed to the sample container volume seen in Figure 2.5 (a) was made due to difficulty in completely filling the small containers for each measurement. Typically a tiny amount of air would still be present in the container after placing the ferrofluid inside.

2.6 Saturation Magnetization $\mu_o M_s$

The nominal saturation magnetization value of each fluid is provided by Ferrotec. These values are listed in Table 2.2. The reader should be aware that for the rest of the thesis the saturation magnetization is generally listed as $\mu_o M_s$ since the units of this quantity are Gauss, a preference of the author. The rigorously correct definition of the saturation magnetization is simply M_s in SI units of A/m.

2.6.1 Maximum Measured Magnetization

The maximum measured magnetization value is close to the saturation value, $\mu_o M_s$, corresponding to the magnetization at the largest applied magnetic field. Table 2.2 lists this magnetization value for each fluid, along with the corresponding magnetic field, and temperature of the trial. The magnetic field values listed are the applied field, H_e, and not the field within the sample, H_i, although the difference is small since $H_e \gg MD$ in (2.21). In saturation the magnetization is independent of the magnetic field magnitude, and so the correction

	$\mu_o M_s$ (Gauss)				
Fluid Sample	**Nominal (Gauss)**	**Estimated (Gauss)**	**Max. Measured M (Gauss)**	T **(K)**	H_e **(kGauss)**
NF 1634 Isopar M	400	444.2	421.3	299	8.0
MSG W11 water-based	162	203.2	187.3	299	14.0
NF 1273 wax ferrofluid	550	NA	NA	NA	NA
NBF 1677 fluorocarbon-based	400	404.9	394.1	323	8.0
EFH1 hydrocarbon-based	400	386.6	365.2	room(≈300)	10.0

Table 2.2: Saturation magnetization values for the ferrofluid samples. The nominal value is given by Ferrotec. The estimated value is determined by the method of section 2.6.2. The maximum measured magnetization is the magnetization value at the maximum applied magnetic field H_e, and the corresponding temperature, T. No experimental data was available for NF 1273.

from external to internal field is not important. The maximum measured magnetization was temperature dependent, as shown by the data in Table 2.3.

2.6.2 Estimated Saturation Magnetization

A better estimated value of $\mu_o M_s$ can be calculated from the high-field limit to the Langevin equation, given in (2.9). This is a linear relationship which can be written as

$$\mu_o M = c + \frac{b}{\mu_o H_i} \tag{2.31}$$

where $c = \mu_o M_s$ is the offset of the line and $b = \dfrac{-6kT\mu_o M_s}{\pi M_d d^3}$ is the slope. The theoretical demagnetization factor of $D = 0.211$ was used with (2.21) to calculate H_i and the experimental data was fit to (2.31) to determine the value of $c = \mu_o M_s$. For MSG W11, NF 1634,

Fluid Sample	**Maximum Measured $\mu_o M_s$ Gauss**	T **K**	H_e **kGauss**
NF 1634 Isopar M	421.3	299	8.0
	419.1	323	8.0
	402.7	374	8.0
MSG W11 water-based	187.3	299	14.0
	183.4	323	14.0

Table 2.3: The temperature dependence of the maximum measured magnetization.

and NBF 1677 the lowermost 30 data points near negative saturation, and uppermost 29 data points near positive saturation were used simultaneously in the fit. The reason for 29 points is that the top point near positive saturation is measured once by the VSM, while near negative saturation the nearest point is measured at the beginning and end of the trial, giving 30 points. For EFH1 only the uppermost 15 data points were fit since no data was taken for a negative magnetic field. These fitted values of $\mu_o M_s$ are listed in Table 2.2 as the 'Estimated' value. Throughout this thesis the maximum measured magnetization values, not the estimated saturation values, are used in calculations and in normalizing plots of M/M_s.

2.7 Magnetic Volume Fraction ϕ

The magnetic volume fraction of each sample was calculated using (2.15) with the value of $\mu_o M_d = 5600$ Gauss, or equivalently $M_d = 446$ kA/m, for magnetite. The values are listed in

Fluid Sample	**Maximum Measured $\mu_o M_s$ Gauss**	T **K**	H_e **kGauss**	ϕ **%**
NF 1634 Isopar M	421.3	299	8.0	7.5
MSG W11 water-based	187.3	299	14.0	3.3
NF 1273 wax ferrofluid	NA	NA	NA	9.8*
NBF 1677 fluorocarbon-based	394.1	323	8.0	7.0
EFH1 hydrocarbon-based	365.2	room(≈300)	10.0	6.5

Table 2.4: The calculated magnetic volume fraction of the ferrofluid samples, using (2.15). The calculations used the maximum measured magnetization values as $\mu_o M_s$ at the indicated magnetic field strength and temperature. *The value of ϕ for NF 1273 was calculated using the nominal saturation magnetization of $\mu_o M_s = 550$ Gauss.

Table 2.4. The maximum measured magnetization values from Table 2.2 are used as $\mu_o M_s$ for calculating ϕ. As with fluid density, measured values of the volume fraction are within the broad range provided by the supply company, Ferrofluidics Corporation. In the case of the wax ferrofluid, data was not taken at the saturation field because the sample leaked and could not be refilled after the low-field data was taken. Thus, the value of $\mu_o M_s$ for the wax ferrofluid is assumed to be that provided by the company and the volume fraction is computed using this value.

Fluid Sample	T **K**	χ **Dimensionless**
NF 1634		
Isopar M	295	2.181
	323	1.862
	348	1.636
MSG W11		
water-based	299	0.669
	323	0.596
	343	0.543
NF 1273		
wax ferrofluid	300	2.586
	323	2.545
	353	2.500
NBF 1677		
fluorocarbon-based	300	3.033
	323	2.674
	374	2.074
EFH1		
hydrocarbon-based	room	1.552

Table 2.5: Calculated magnetic susceptibility of the ferrofluid samples at the indicated temperatures. The values of χ were determined with a least-squares linear fit in Mathematica.

2.8 Determination of Magnetic Susceptibility χ

To calculate the magnetic susceptibility as given in (2.10) it was necessary to convert external magnetic field values to the corresponding internal field value using (2.21) along with the theoretical demagnetization value of $D = 0.211$. A least-squares linear fit of the M vs. H_i experimental data was then completed using the 'Fit' command in Mathematica. The y-intercept of the fit was allowed to float so as to take into account the slight offset of the magnetization values at zero applied magnetic field. The slope of these fits was taken as χ. These values, shown in Table 2.5, are given for each low-field trial.

The display cell fluid, NBF 1677, shows a higher magnetic susceptibility than does the Isopar M ferrofluid, NF 1634, whereas the order of saturation magnetization values for these fluids was reversed. This indicates that the display cell fluid has larger particles, which dominate the low-field regime magnetization behavior, producing a higher susceptibility. It is also noted that in all cases the susceptibility value tends to decrease with an increase in temperature, as would be expected from the Langevin theory of (2.10).

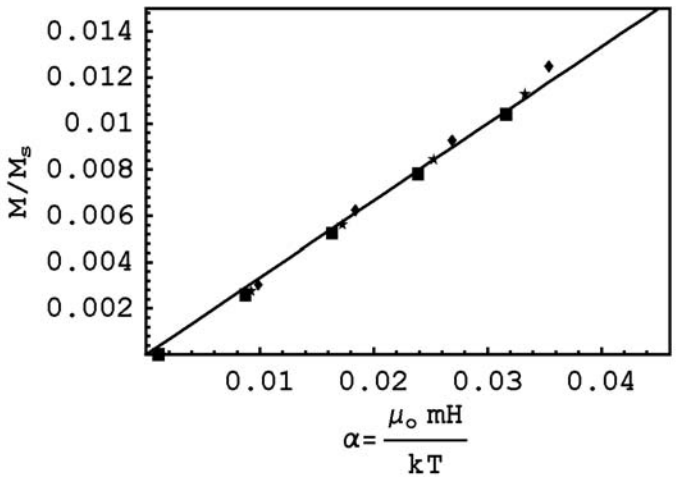

Figure 2.7: Measured low-field data for MSG W11 water-based ferrofluid is represented by diamonds at 26^o C, stars at 50^o C, and squares at 70^o C. The theoretical Langevin function is plotted as a solid line. The parameter α for the experimental data best fits the theory using a particle size of 12 nm, corresponding to d_{max} given in Table 2.6. The slope of the fit line is $\approx 1/3$.

All collected data appear to follow the $1/T$ relationship expected from Langevin theory, as seen in Figures 2.7 and 2.8. Plotting all the data against the argument of the Langevin function, α, required specification of a particle diameter and demagnetization factor for each data set. The value of D was chosen as 0.211 and the particle diameter for each

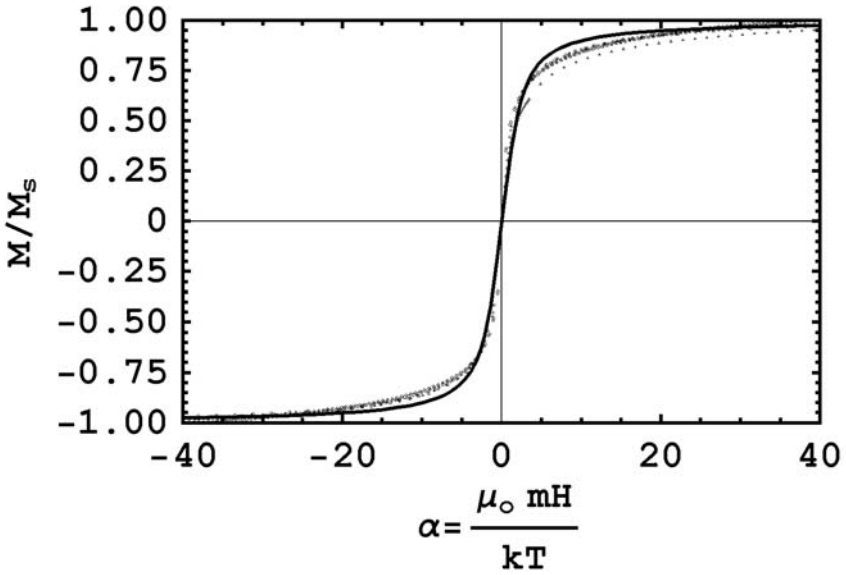

Figure 2.8: Measured magnetization (dots) for four ferrofluids containing magnetite particles ($M_d = 446$ kA/m or equivalently $\mu_o M_d = 0.56$ Tesla) plotted with the theoretical Langevin curve (solid line). The data consist of Ferrotec Corporation ferrofluids: NF 1634 Isopar M at 25.4^o C, 50.2^o C, and 100.4^o C all with fitted particle size of 11 nm; MSG W11 water-based at 26.3^o C and 50.2^o C with fitted particle size of 8 nm; NBF 1677 fluorocarbon-based at 50.2^o C with fitted particle size of 13 nm, and EFH1 hydrocarbon-based (positive α only) at 27^o C with fitted particle size of 11 nm. All data falls on or near the universal Langevin curve indicating superparamagnetic behavior. The parameter α for the data sets was calculated using d_{avg} in Table 2.6

sample was d_{avg} as shown in Table 2.6. The method for determining the particle sizes is discussed below. Slight deviations from the $1/T$ pattern may be due to the samples not being in thermal equilibrium. Several conversations with the VSM manufacturer indicated that the sample positioning within the VSM can affect the heating of the sample, which is accomplished by heated gas flow around the container. The company representative said the sample temperature may differ from the machine-reported value by as much as five degrees centigrade. To test this, a thermocouple was placed in the approximate location of

the sample holder and various temperatures were set on the VSM. The thermocouple and VSM frequently reported temperatures differing by up to ten degrees centigrade. It therefore seems likely that the sample temperature was not exactly as reported by the VSM for trials at elevated temperatures.

2.9 Determination of Magnetic Particle Diameter

Ferrofluids contain particles covering a range of sizes. As mentioned in the discussions of ferrofluid magnetization and particle relaxation, ferrofluid behavior is dependent on the size of the particles. Determining the range of particle sizes within the fluid is therefore useful. Magnetic particle diameters were determined in several ways. The first and ultimately most consistent method was to fit the low-field, saturation-field, and full range experimental data to the Langevin curve and the appropriate asymptotes in Mathematica.

2.9.1 Minimum Particle Diameter

The minimum ferrofluid particle diameters were determined by the same method as was employed in finding the estimated saturation magnetization in section 2.6.2, in other words fitting the experimental data to (2.9) using the form of (2.31). The parameter $b = \dfrac{-6kT\mu_o M_s}{\pi M_d d^3}$ was determined, which can be rearranged to solve for d. These values are listed as d_{min} in Table 2.6.

2.9.2 Average Particle Diameter

The full positive range of magnetization data, from zero applied field to saturation, was fit to the complete Langevin equation given by (2.7). The argument of the Langevin function was

Fluid Sample	d_{min} **(nm)**	d_{avg} **(nm)**	d^{*}_{max} **(nm)**	d^{**}_{max} **(nm)**	d^{***}_{max} **(nm)**
NF 1634 Isopar M	7.7	11.0	14.1	13.9	12.8
MSG W11 water-based	5.5	7.9	12.2	12.4	11.8
NF 1273 wax ferrofluid	NA	NA	13.4	13.6	12.4
NBF 1677 fluorocarbon-based	9.7	12.6	15.9	16.0	14.6
EFH1 hydrocarbon-based	6.9	10.6	13.3	13.1	12.2

Table 2.6: The particle diameter range of the ferrofluid samples. The value of d_{min} is calculated as described in section 2.9.1. The value of d_{avg} is determined by the best-fit of the positive region experimental data range to the Langevin theory, as described in section 2.9.2. These values were used to determine the parameter α in Figure 2.8. * The value is determined by a best-fit of the low-field experimental data to the Langevin equation. ** The value is calculated from (2.14). *** The value is calculated from (2.13). The accuracy of the measurements only justifies reporting particle diameters to the nearest nm, however, to highlight the distinction between the different methods used the values are reported to a single decimal place.

defined as a function of magnetization and applied magnetic field data pairs. The function was then fit to the experimental data pairs in Mathematica using a nonlinear curve fit and the 'BestFitParameters /. NonlinearRegress' command while leaving the particle diameter as a dependent variable. Mathematica then returns the particle diameter which produces the best least-squares fit to the experimental data. These fitted values are listed as d_{avg} in Table 2.6. These values are expected to be an average particle diameter since data in both the low-field and saturation regimes is included. However, since the majority of experimental

data points are from the near-saturation region these values may be slightly smaller than the true average. Completing the computer-aided fit required specifying a demagnetizing factor, for which the value of 0.211 was used. The accuracy of the experimental data does not merit reporting the particle diameter to one decimal place, which would indicate only a 1% error, and calculations in the rest of this chapter use particle sizes rounded to the nearest nanometer. However, the values are reported to one decimal place in Table 2.6 because it is worthwhile to see how similar the particle sizes were between samples, as well as the differences between the various methods of calculating the particle diameter. A representative full-range field fit is shown in the upper frame of Figure 2.9. The plots for the other fluid samples are found in Appendix A.

These fits were also performed for the entire physical range of demagnetizing factors, from 0 to 1 which allowed bracketing of the particle diameters. In all cases the spread of particle diameters at the respective low or high field limit was no more than four nm. For the Isopar M based fluid all three sets of temperature dependent data were fit in the saturation-field regime and each produced a particle size of 11 nm. Values for the wax ferrofluid assumed $\mu_o M_s$ of 550 Gauss. It is noted that for all samples the theoretical fit at saturation does not match the experimental data exactly. The reason is because the fitting method requires specification of a value of saturation magnetization, which acts as an asymptote below which the theoretical curve will remain. These values were taken from the 'Max. Measured M' column in Table 2.2, which are known to be slightly less than the actual saturation magnetization value. Thus the theoretical fit lines lie slightly below the experimental data in the saturation region. This slight inaccuracy of fitting at saturation likely causes a slight error in the overall fit, the degree of which could not be quantified. In

the future it may be wise to use both the 'Estimated' and 'Max. Measured M' values from Table 2.2 to determine the difference in the resulting fits.

2.9.3 Maximum Particle Diameter

Experimental Data Fit

The maximum particle diameter was found in three ways, the values of which are all listed in Table 2.6. The first was to fit (2.7) to the first 16 data points (0-15 Gauss applied field) of the low-field experimental data. As with fitting the entire data range to calculate average particle diameters, in this case the low-field experimental data pairs were fit using a nonlinear curve fit and the 'BestFitParameters /. NonlinearRegress' command in Mathematica while leaving the particle diameter as a dependent variable. A representative low-field fit is shown in the bottom frame of Figure 2.9.

Langevin Low-field Asymptote

A second method of determining the maximum diameter is to calculate the value using (2.14). The values of χ and T needed for this calculation were taken from Table 2.5.

Shliomis Correction

A third determination of maximum particle diameter was calculated based on (2.13). These values are listed in Table 2.6. As mentioned, (2.13) is a correction to the low-field Langevin behavior that takes into account dipole interactions. The equation is meant to be used for fluids with $\phi > 10\%$. Thus, as seen in Table 2.6 the correction makes a noticeable change in the particle diameter only for the fluids with a relatively large magnetic volume fraction.

All methods of determining the particle size suggest that the NBF 1677 display fluid

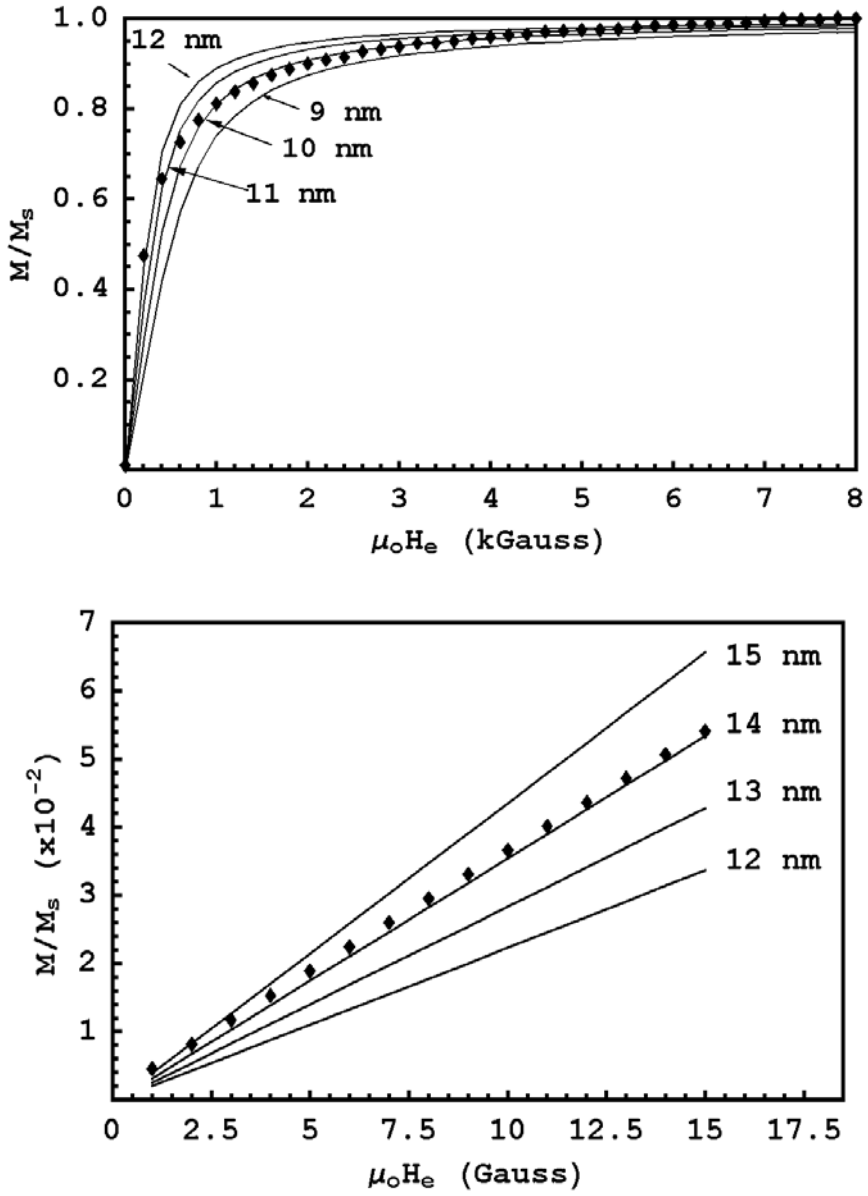

Figure 2.9: (Top) Theoretical Langevin fit of measured NF 1634 Isopar M based ferrofluid magnetization data for various particle sizes using $D = 0.211$. Data (diamonds) taken at 25.4^o C indicates a best-fit average particle diameter of d_{avg} ∼11nm. (Bottom) Theoretical Langevin fit of measured NF 1634 Isopar M based low-field magnetization data for various particle sizes using $D = 0.211$. Data (diamonds) taken at 21.6^o C indicates a best-fit largest particle diameter of d_{max} ∼14nm.

has the largest particles, followed by NF 1634 Isopar M-based, NF 1273, EFH1, and MSG W11 water-based ferrofluid. Again, calculations for the wax ferrofluid assumed $\mu_o M_s$ of 550 Gauss as provided by Ferrotec.

The data shown in Table 2.6 verifies that the saturation-field response is dominated by the smaller particles and that the low-field response is dominated by the larger particles.

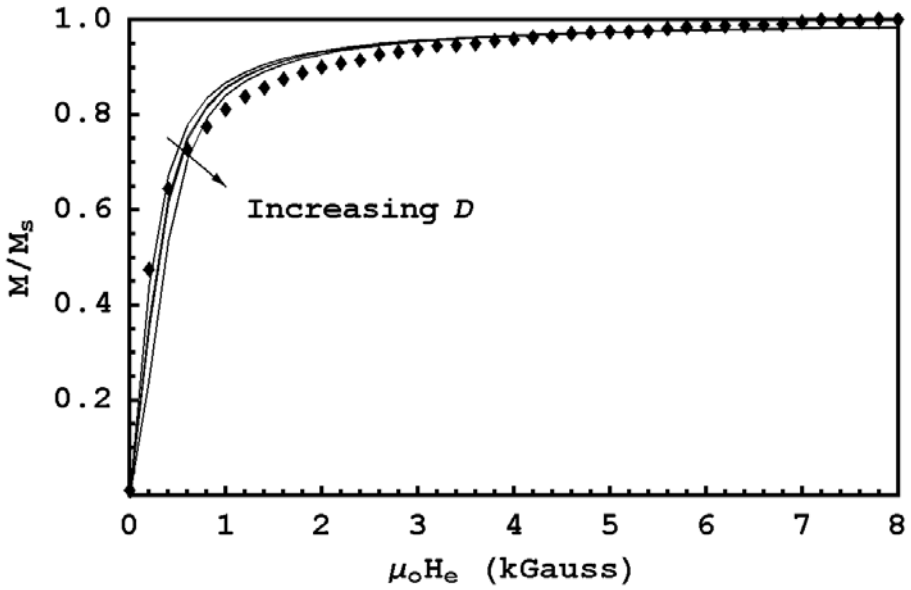

Figure 2.10: Fit of NF 1634 Isopar M saturation-field data (diamonds) to various values of demagnetizing factor; D=0, 0.211, 0.25, and 0.5. The fit lines for D =0.211 and 0.25 are almost indistinguishable. The particle size is assumed 11 nm for generating the theoretical lines.

2.10 Effects of the Demagnetizing Factor

As previously discussed in section 2.4 the estimated demagnetization factor for the sample can be found theoretically and experimentally. The approximate theoretical value of D = 0.211 has been used in calculations up until this point, however it should be stressed that the

Fluid Sample	Temperature K	χ_e	Demagnetization Factor D
NF 1634			
Isopar M	295 (T1)	1.494	-0.144 (T1,T2)
	323 (T2)	1.337	-0.172 (T1,T3)
	348 (T3)	1.216	-0.211 (T2,T3)
NF 1273			
wax ferrofluid	300 (T1)	1.673	0.519 (T1,T2)
	323 (T2)	1.656	0.524 (T1,T3)
	353 (T3)	1.637	0.529 (T2,T3)

Table 2.7: Calculated demagnetization factors of samples using (2.27) for the indicated temperature pairs. The actual calculations were done with temperature values to 2 decimal places as given by the VSM; the listed temperatures are rounded since the accuracy of the temperature readings does not merit reporting to two decimal places as discussed in section 2.8.

ferrofluid sample container was merely modeled as an oblate ellipsoid. Several alternative methods for determining a value of the demagnetizing factor that would be more specific to each individual sample were explained in section 2.4.3 but proved unfruitful due to the apparent sensitivity of the equations used to estimated parameters such as the particle size. The first method, as with particle size calculations, was to fit the Langevin equation to the positive magnetic field experimental data using a nonlinear fit in Mathematica. A particle size was designated and the experimental data pairs fit to the Langevin function using the demagnetizing factor as a dependent variable. Fits were done in both the full range and low-field regimes, and required specifying a particle size. The particle size was set at several increments from 5 to 15 nm. Values of D were often unphysical, being negative or greater than one. The difficulty in sensitivity is demonstrated in Figure 2.10 for NF 1634 Isopar M-based ferrofluid in which the experimental data at some values of H lie above all the fit curves, and at other values of H lie completely below the fit curves. It was not possible to

determine the demagnetizing factor in this way.

In addition to the determination of d and D separately by fitting, the experimental data was again fit in Mathematica using both d and D as unknowns simultaneously, yet this never produced physical results for both parameters.

Fluid Sample	d **nm**	**Demagnetization Factor D Calculated with (2.28)**	**Demagnetization Factor D Calculated with (2.29)**
NF 1634 Isopar M	11.0	-0.26	-0.04
	14.1	0.23	0.15
MSG W11 water-based	7.9	-4.03	-2.16
	12.2	0.15	0.60

Table 2.8: Calculated demagnetization factors of two ferrofluid samples using (2.28) and (2.29) at the listed particle size value. The other parameters needed for the calculations were: NF 1634- $\chi_e = 1.494$, $T = 295$, $\mu_o M_s = 421.3$; MSG W11- $\chi_e = 0.586$, $T = 299$, $\mu_o M_s = 187.3$.

The demagnetization factor could also be calculated directly via (2.27), (2.28), and (2.29). These values, as with the values produced by fitting, were frequently not physical. The results are listed in Tables 2.7 and 2.8. It is possible that the samples were not in thermal equilibrium, or that the assumption of q, defined in (2.12), being constant in (2.27) is not valid over the temperature range investigated because M_d, ϕ, or d may change with temperature. This conclusion is supported by the data of Table 2.3 which shows that the maximum measured magnetization, taken as $\mu_o M_s = \mu_o \phi M_d$, varies slightly with temperature. Future work should determine whether the estimated values of $\mu_o M_s$ described in section 2.6.2 are temperature dependent. Demagnetization values calculated with (2.28) exhibited as much as

a 50% change when altering the particle diameter by just 1 nm. This suggests the equation is simply too sensitive to particle size values to be used with the collected data.

2.11 Discussion

Magnetization curves of ferrofluids using a VSM are reasonably accurate in obtaining sample properties such as magnetic permeability, minimum, average, and maximum magnetic particle diameters, magnetic volume fraction, and saturation magnetization.

The experimental results support the theory that the magnetic susceptibility, defined when $\alpha \ll 1$, is dominated by larger particles, while the magnetization curve is dominated by smaller particles in the saturation regime, $\alpha \gg 1$, where $\alpha = \mu_o mH/kT$ is the argument of the Langevin function. As such, the data verify that the magnetic susceptibility is particle size dependent, with fluids containing larger particles exhibiting higher susceptibilities than those with smaller particles. The results further allow the calculation of the magnetic particle diameter range of the ferrofluid sample. However, the diameter values could only be determined within ± 1 nm, indicating that currently available direct imaging measurement methods may prove more useful. A drawback of these methods, however, is the difficulty in distinguishing the magnetic particle core from the surfactant layer.

Knowledge of the demagnetization factor of ferrofluid samples is best obtained through theoretical work based on geometrical considerations of the ferrofluid container. Calculation of such a value from experimental data is shown to require high accuracy of the measured parameters, most notably particle diameter. Still, the methods suggested may prove useful in the future when experimental systems allow for highly accurate measurements of the physical parameters.

Future work should consider a method for verifying whether or not the fluid samples are in thermal equilibrium. Data taken over larger temperature ranges than those presented may also provide useful information in verification of Langevin theory. An accurate method for determining demagnetizing factors experimentally should also receive attention. Consideration of the temperature dependence of domain magnetization and volume fractions should be examined when applying some of the equations presented.

Chapter 3

Ferrofluid Flow Through a Closed Tube

Now that the fluid characterization is complete we turn to a set of experiments involving ferrofluid flow through a tube. The work is motivated both by previous results reported by Energy International, as well as the desire to relate the results to the potential design and implementation of a ferrofluid pump that would be free of mechanical components. The results also lead to an investigation of open channel flow, again with the purpose of designing ferrofluid pumps.

3.1 Pressure Drop without a Magnetic Field

An initial investigation into the pressure drop across a length of tubing with mechanically driven flow and no applied magnetic field was undertaken with several magnetic and non-magnetic fluids for the purpose of establishing a baseline for later work studying magnetic fluids in the presence of applied magnetic fields. In order to theoretically model the experiments of this chapter several fluid parameters must be determined both experimentally and

Measured Mass Densities of Fluid Samples		
Fluid	**Density** (g/cm^3)	**Error** ($\pm\%$)
Tap Water	0.986	1.0
MSG W11	1.204	1.0
EFH1	1.169	1.0
Glycerol/Tap Water 1:2 volume ratio	1.050	1.0
Glycerol/Tap Water 3:1 volume ratio	1.177	1.0

Table 3.1: Mass densities of the fluid samples used during experimentation of pump-driven flow. The experimental errors in the mass measurements and volume measurements needed for the calculation of the densities were combined into the listed error in density. The method of combining the errors is explained in Appendix B.3

theoretically, including fluid density, viscosity, Reynolds number, and entrance length.

3.1.1 Fluid Density

The densities of the fluid samples being tested were previously measured and described in Chapter 2. They are restated in Table 3.1 along with the values of tap water and two glycerol/tap water mixtures, all three of which served as non-magnetic controls for the experiments of this chapter.

3.1.2 Fluid Viscosity

Viscosity is a gauge of the resistance of fluid flow to shear forces. A fluid with a high viscosity, such as honey, exhibits a strong resistance to flow and dissipates a relatively large amount of internal energy due to friction between the shearing fluid layers. Alternatively, low viscosity fluids (such as water) flow easily and lose a relatively small amount of energy to viscous dissipation. The fluid dynamic viscosity is represented by the symbol η.

Measured Fluid Dynamic Viscosities I					
Fluid	η **(cP)**	**Spindle Speed (r.p.m.)**	**Torque (% Full Scale)**	**T (^{o}C)**	**Error (cP)**
MSG W11	7.26	100	12.1	25.8	$\pm$0.6
EFH1	10.4	100	17.4	25.9	$\pm$0.6
Glycerol/Tap Water 1:2 volume ratio	5.82	100	9.7	25.6	$\pm$0.6
Glycerol/Tap Water 3:1 volume ratio	40.0	20-100	$> 10\%$	NA	$\pm$2.6*

Table 3.2: Viscosity of fluid samples measured using a Brookfield DV-I+ shear viscometer. The value for each of the first three samples was obtained from a single measurement, while the value for the glycerol/tap water 3:1 volume ratio mixture was obtained from the average of 6 individual measurements. The errors listed are given by the instrument error, which is 1% of the full scale viscosity range, and can be calculated as shown on page 34 of the user manual [28]. The full scale torque of the instrument is 67.3μN-m. *The error cited is the standard deviation of the six individual measurements.

Rotating Shear Viscometer

The viscosity of the five fluid samples used in this set of experiments was experimentally determined using several methods, often producing conflicting values. First, a rotating shear viscometer was used (Brookfield DV-I+) producing the results shown in Table 3.2. The apparatus consists of a metallic company-calibrated spindle (LV #1) which is placed inside a beaker containing the fluid to be tested. The spindle is programmed to rotate at a set speed by the user, and a torque spring calculates the torque required by the viscometer to keep the spindle in steady motion at the given speed. The torque is converted to a digital viscosity readout by the instrument, in units of centipoise (cP) as well as % torque of full scale (the maximum torque which the spring can measure, 67.3 μN-m). A detailed procedure for using the viscometer is given in Appendix B.1.

Two cases represented in Table 3.2 require explanation. First, no viscosity measurement

of tap water was completed because the viscometer is not accurate for viscosities of such a low value, however the accepted value is 1 cP at 20^oC [29]. More specifically, the viscometer is listed as being accurate only above 10% torque of full scale, a requirement not met when testing water. This is also the reason that only a single spindle speed measurement was made for MSG W11, EFH1, and the glycerol/tap water 1:2 volume ratio mixture. When using spindle speeds below the maximum allowable 100 rotations per minute (r.p.m.) these fluids did not meet the 10 % torque requirement. Secondly, the measurement of the glycerol/tap water mixture in a 3:1 volume ratio was done at several spindle rotation speeds, and the viscosity value listed is determined from the average of the six individual trials. Also, one of the six trials used the LV #2 company-calibrated spindle, which differs from the LV #1 in that the area of shearing is smaller. The LV #2 is thus recommended for highly viscous fluids that may exceed the instrument's maximum torque reading capability with the LV #1 spindle. It should further be noted that Ferrotec supplied viscosity data for the MSG W11 and EFH1 ferrofluids. The data sheets report 3 cP at 27^oC for MSG W11 and less than 9 cP for EFH1 at the same temperature. The collected data in Table 3.2 is clearly not in agreement with the value for MSG W11, but is reasonable for the value of EFH1.

One likely source of error with the experimental data is that the shearing action of the spindle creates turbulence within the fluid sample for ratios of spindle speed (r.p.m.) to viscosity (cP) greater than 4 [30]. The data in Table 3.2 make clear that this ratio was exceeded for the trials involving MSG W11, EFH1, and the glycerol/tap water 1:2 volume ratio mixture. The extent of the turbulence, and its effect, is not known, although it would be expected to produce an erroneously high viscosity value.

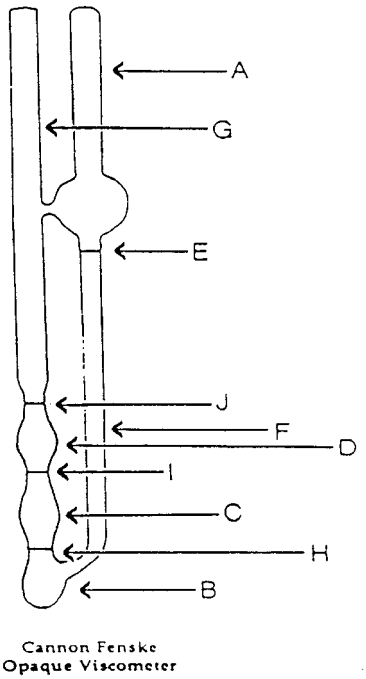

Figure 3.1: Schematic of the Cannon-Fenske viscometer, ASTM size 100. Taken from the data sheets provided by VWR International. The proper use procedure is given in Appendix B.2.

Cannon-Fenske Opaque Kinematic Viscometer

The viscosity values of the MSG W11 and EFH1 ferrofluid samples were also measured using a Cannon-Fenske opaque kinematic viscometer. The procedure for using a Cannon-Fenske viscometer is given in Appendix B.2. The viscometer range was listed as 3-15 centiStokes (cS). CentiStokes are a unit of kinematic viscosity and can be converted to the dynamic viscosity units of cP as follows

$$1 \text{ cP} = 1 \text{ cS} \times \rho \tag{3.1}$$

in which ρ is the mass density of the fluid in g/cm^3. The viscometer gives two readings per trial, one corresponding to the lower bulb, C, and another to the upper bulb, D, as shown in Figure 3.1. Three trials were completed for MSG W11, giving a total of six measurements. Two trials were completed for EFH1 giving a total of four measurements. The values reported in Table 3.3 are averages of these data points. Further trials were not completed because of the extreme difficulty in cleaning the viscometer after using the EFH1 ferrofluid.

Measured Fluid Dynamic Viscosities II			
Fluid	**Viscosity (cP)**	**Temperature (^{o}C)**	**Error ($\pm$ %)**
MSG W11 (3 cP)	2.80	20	< 2
EFH1 (<9 cP)	9.76	19	< 2

Table 3.3: Viscosity of fluid samples measured with a Cannon-Fenske opaque kinematic viscometer. The samples are identified by name and the nominal viscosity provided by Ferrotec. The errors are based on a one second error in the timing of the trials, a company listed 0.35 % error in the instrument calibration, and the error in the density values of the fluids.

Rotating Cone Viscometer

The viscosity of MSG W11 was also measured using a rotating cone viscometer (TA Instruments model AR 1000-N rheolyst). A thin layer of ferrofluid is placed on a metallic plate, and the cone brought within close range of the plate, thus forming a good seal with the fluid. The cone is then rotated at several different shear rates with a viscosity value being determined by the instrument for each rate. The different shear rates are examined because some fluids, called non-Newtonian fluids, have a shear rate dependent viscosity. In contrast the viscosities of Newtonian fluids are independent of shear rate. The average value for MSG W11 was 4.2 cP over the range of shear rates from 15-2000 rotations per second, with a standard deviation of 0.2 cP, indicating the ferrofluid is Newtonian. A measurement

of EFH1 ferrofluid was also attempted, but the fluid would not remain in place between the plate and cone. This is not unheard of with the type of instrument employed. The solution to the problem is to utilize a different measurement geometry than the cone-plate method used here. Unfortunately, an alternative geometry was not available in this case.

Chosen Fluid Dynamic Viscosities	
Fluid	η **(cP)**
Tap Water	1.0
MSG W11	4.2
EFH1	10.0
Glycerol/Tap Water	
1:2 volume ratio	5.82
Glycerol/Tap Water	
3:1 volume ratio	40.0

Table 3.4: The chosen dynamic viscosity values to be used in all calculations of this thesis.

Chosen Fluid Viscosities

In light of the wide spread of some measured viscosity values for individual fluids presented thus far, best guess values for the viscosity were made. For EFH1 the viscosity is taken to be 10 cP based on the approximate average of the Brookfield viscometer and Cannon-Fenske viscometer readings. This value is only slightly outside the range provided by Ferrotec. For MSG W11 the value is taken as 4.2 cP as given by the cone viscometer, which is also approximately halfway between the values given by the Brookfield and Cannon-Fenske viscometers, but not in agreement with the Ferrotec data sheets. However, the stability of the measurement over such a wide range of shear rates makes the value more credible. For the two glycerol/tap water solutions the viscosity is that given in Table 3.2 since it is the only value available. These numbers will be used in later calculations and are summarized in

Table 3.4.

3.1.3 Surface Tension

Although not expressly used in the equations of this chapter, the property of surface tension is used later in the thesis, and is presented now to complete the description of the ferrofluids. In general, fluids form an interface when in the presence of other liquids or gases. This is because the molecules of the fluid are more attracted to each other than they are to the molecules of the foreign substance. There is necessarily a force required to hold the fluid interface together. Surface tension is a measure of this force, and has units of force per length.

The surface tension of EFH1 hydrocarbon-based ferrofluid and MSG W11 water-based ferrofluid were measured at room temperature with a digital tensiometer (Krüss model K10ST). The simple procedure includes filling a standard glass container with approximately 10 ml of ferrofluid and then lowering into the ferrofluid a thin, perfectly wetting (contact angle of zero), platinum plate suspended by the tensiometer spring. When wetted, the plate experiences a vertically directed downward force from the surface tension of the fluid. The tensiometer measures the force required to keep the plate at a constant vertical height within the fluid, and thus calculates the surface tension by normalizing the total force to the plate length. As a check of the system, a measurement was made with distilled water. The result was a viscosity value of 72.3 dyne/cm, which is close to the published value of 72.8 dyne/cm at 20^o C [31, p.597], indicating that the measurements are sufficiently accurate for our purposes. The complete results are summarized in Table 3.5.

Measured Surface Tension		
Fluid	**Surface Tension (dyne/cm)**	**Estimated Error (± dyne/cm)**
Distilled Water	72.3	0.3
MSG W11	41.3	0.3
EFH1	25.8	0.3

Table 3.5: The measured surface tension values of three fluid samples. A single measurement at room temperature was made for each fluid. The listed error corresponds to the observed fluctuation of the reading with time.

3.1.4 Reynolds Number and Entrance Length

The dynamics of fluid flow in a tube are dependent on a dimensionless group called the Reynolds Number

$$\text{Reynolds Number} = Re = \frac{\rho U d}{\eta} = \frac{U d}{\nu} = \frac{\text{inertial force}}{\text{viscous force}} \tag{3.2}$$

in which U is the mean fluid velocity, d is the tubing diameter, η is the dynamic viscosity, and $\nu = \eta/\rho$ is the kinematic viscosity. Flow with a Reynolds number below some critical value is termed laminar, and is characterized by non-intersecting streamlines. Flow above the critical Reynolds number is termed turbulent, and is marked by vortices and mixing of adjacent streamlines. In actuality there is a range of Reynolds numbers signifying a transition from laminar flow to fully developed turbulent flow. Yet, the generally accepted critical Reynolds number value for pipe flow transition from laminar to turbulent is 2300 [32, p. 310]. The analysis of the laminar and turbulent regimes, as well as the physical behavior of each system, are significantly different. Since our experiments typically operate with $Re < 2300$ we assume that our system lies within the laminar regime for even the largest flow rates studied, as generally supported by Figure 3.2, except for tap water and MSG W11 at the larger flow rates.

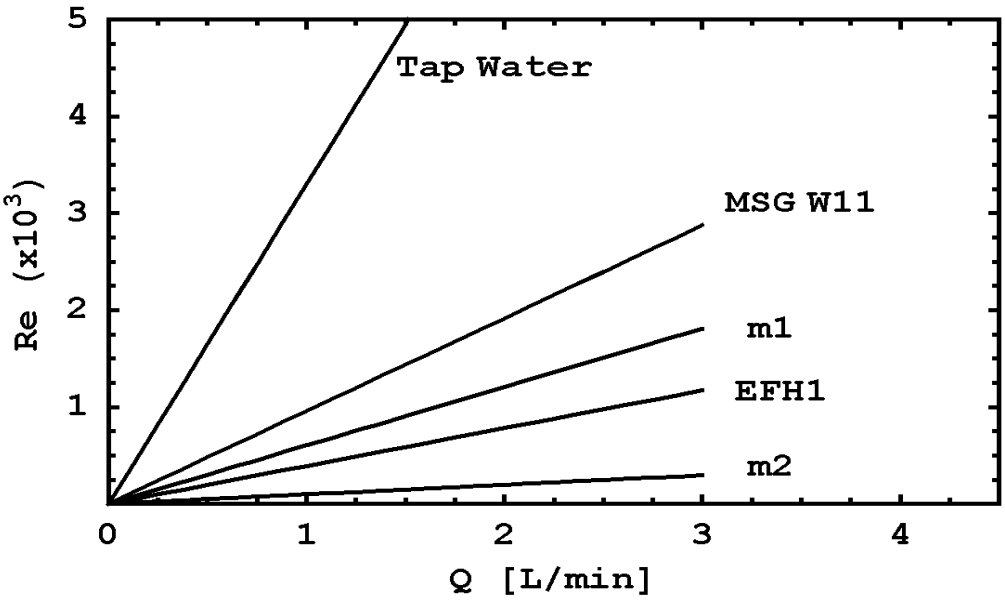

Figure 3.2: Reynolds number as a linear function of volumetric flow rate for the experimental fluids. The inside diameter of the tubing is 1/4 inch, and the densities and viscosities of the fluids are given in Tables 3.1 and 3.4. The designations 'm1' and 'm2' represent the glycerol/tap water 1:2 volume ratio mixture, and glycerol/tap water 3:1 volume ratio mixture, respectively.

The entrance length prescribes the distance required for flow at an inlet to reach its fully developed state of either laminar or turbulent flow. As given by White [32, p. 312] the entrance length for laminar flow in a circular pipe of diameter d is

$$L_e \approx 0.06Re \times d. \tag{3.3}$$

The entrance lengths for the experiments of this chapter are plotted in Figure 3.3 and are considered in the design of the following experiments.

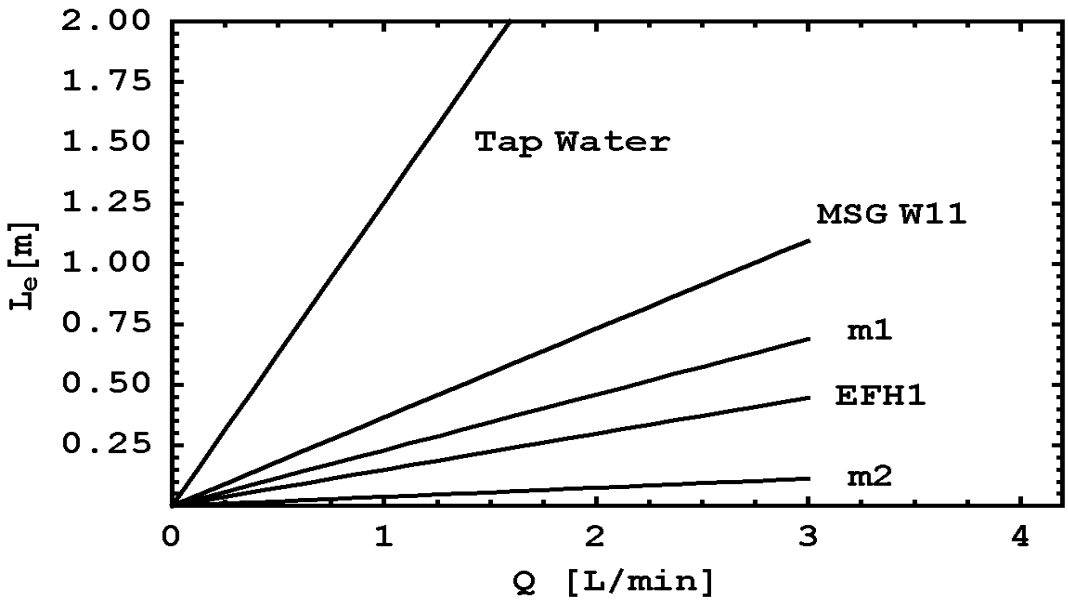

Figure 3.3: The entrance length, L_e, of a circular-pipe flow system as a function of flow rate, based on (3.3). The inside tubing diameter is 1/4 inch and the densities and viscosities of the fluids are given in Tables 3.1 and 3.4. The designations 'm1' and 'm2' represent the glycerol/tap water 1:2 volume ratio mixture, and glycerol/tap water 3:1 volume ratio mixture, respectively.

3.1.5 Flow In the Absence of An Applied Magnetic Field

A simple flow loop was constructed consisting of pump-driven flow (Cole-Parmer Gear Pump model 75211-10) through flexible tubing (1/4 inch I.D. flexible vinyl VWR Brand) with a straight section of tubing of length $l = 34$ cm. A flow meter (AW Company model JVA-20kl analog output) recorded the flow rate and two pressure transducers (Omega PX 236 Series 0-100 p.s.i. analog output) recorded the pressure drop across l. Such a system consisting of viscous laminar flow has a linear relationship between pressure drop and flow rate

$$\Delta p = \frac{8\eta l Q}{\pi r^4} \tag{3.4}$$

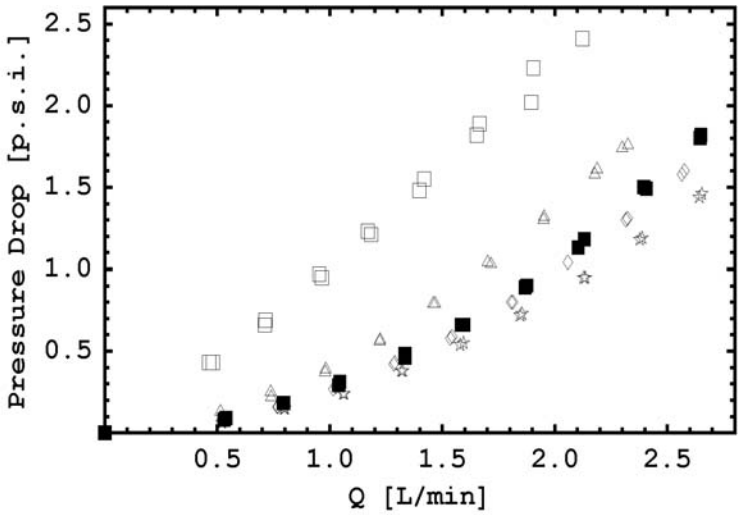

Figure 3.4: Experimental data of pressure drop versus flow rate for 5 fluid samples. Each sample is representative of 2 individual trials. The samples are; stars-tap water, diamonds-m1 (glycerol/tap water in 1:2 volume ratio), boxes-m2 (glycerol/tap water in 3:1 volume ratio), triangles-EFH1 hydrocarbon-based ferrofluid, and solid boxes-MSG W11 water-based ferrofluid.

for which Δp is the pressure drop, η is the dynamic viscosity, l is the distance of flow, Q is the volumetric flow rate, and $r = d/2$ is the tubing radius [32, p.324]. Two trials were completed for each of the five fluid samples tested and the results shown in Figure 3.4. An important aspect of Figure 3.4 is that only the data for the glycerol/tap water 3:1 volume ratio mixture is linear for most of its flow range. The other data sets are all non-linear for most of the flow range. In trying to understand this unexpected result all the data was fitted to an equation valid for turbulent flow with $4000 < Re < 10^5$ [32, p.329], written in English units as

$$\Delta p \approx 0.241 L \rho^{3/4} \eta^{1/4} d^{-4.75} Q^{1.75} \tag{3.5}$$

for which L is the length of tubing, and d is the tubing diameter, in ft, Δp is in lbf/ft^2, ρ is in lb/ft^3, η is in slug/ft-sec, and Q is in ft^3/sec. Since all the experimental parameters were measured to reasonable accuracy, e.g. the length of flow, the mass density, and the tubing radius, this task reduced to fitting (3.5) to the experimental data using a variable viscosity. Yet the quality of the fitting was only good with viscosity values on the order of 10^3 cP which is physically unreasonable. From this we infer that the flow is not turbulent, as expected from Figure 3.2, and therefore (3.5) is not applicable.

A second potential explanation for the nonlinear flow behavior is that the length of tubing from the inlet to the first pressure transducer was too short, i.e. shorter than the entrance length and as such the flow did not achieve its fully developed laminar profile before reaching the first pressure transducer. This was taken into consideration however, and the length of tubing before P_1 was believed to be longer than the theoretical entrance length values shown in Figure 3.3 except possibly for tap water and MSG W11 at the larger flow rates where the theoretical entrance length is larger than the experimental tube length from the reservoir to the first pressure transducer.

The instrumentation could also have lead to erroneous data, but both the pressure transducers, as well as the flow meter, were calibrated before experimentation and are not believed to be a source of error contributing to the anomaly.

Although the flow rate data did not match the expected laminar flow theory of (3.4), the results were reproducible and the accuracy of the instrumentation checked. The data was thus accepted as accurate for the physical situation and reliable to serve as the baseline for comparison to flow rate experiments with a magnetic field.

3.2 Gradient-Magnetic-Field Test

As a check of the flow loop system to be developed we conducted a gradient-magnetic-field test. A length of tubing (1/4 inch I.D. vinyl VWR Brand) was outfitted with two pressure transducers (Omega PX 236 Series 0-100 p.s.i. analog output) for the purpose of measuring the pressure drop along the length of the tube. The governing theory for this investigation is the ferrohydrodynamic Bernoulli equation, which is the fluid mechanical Bernoulli equation augmented with a magnetic field term. Bernoulli's equation can be derived from a force balance within a fluid system, and in the form of (3.6) is applicable only for inviscid, non-rotational, steady, incompressible flows [29]. The formulation in the absence of body forces, except for gravity, is commonly written as

$$P + \rho g z + \frac{1}{2}\rho v^2 = \text{constant} \tag{3.6}$$

in which P is the pressure at the point of interest, ρ is the fluid mass density, g is the gravitational acceleration taken to be in the $-\hat{z}$ direction, z is the vertical height of the point of interest relative to a reference point, and v is the fluid velocity. The ferrohydrodynamic Bernoulli equation takes into account magnetic forces on the fluid, and thus contains an extra term [1, 33]

$$P + \rho g z + \frac{1}{2}\rho v^2 - \mu_o \bar{M} H = \text{constant}. \tag{3.7}$$

In (3.7) $\bar{M}$ represents the average magnetization of the fluid at that value of H and is defined as [1]

$$\bar{M} = \frac{1}{H}\int_0^H M_s L(\alpha) dH \tag{3.8}$$

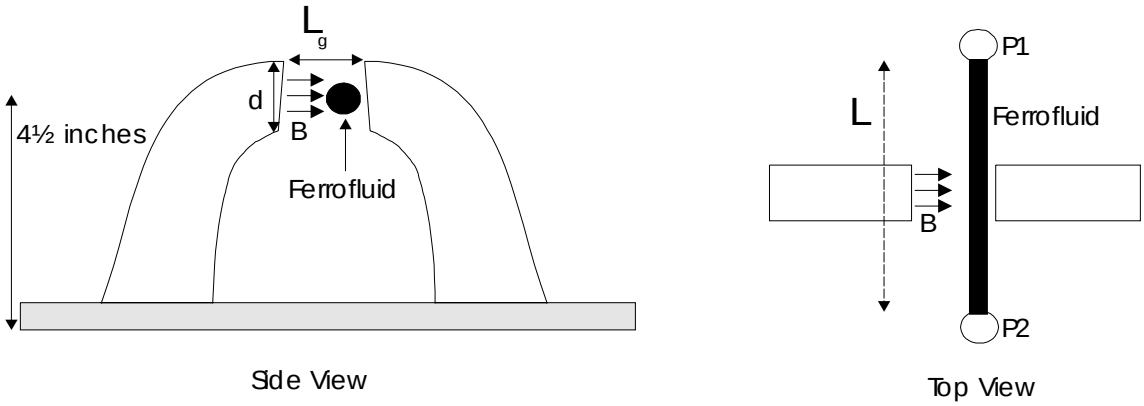

Figure 3.5: The experimental configuration used to examine the Ferrohydrodynamic Bernoulli Equation of (3.7). The center gap distance L_g is 42 mm and the diameter of the circular pole pieces is 39 mm. The approximate magnetic field strength at the center of one of the pole faces is 1.5 kGauss. The length of ferrofluid filled tubing is $L = 34$ cm. Additional tubing (not shown) connects P_1 and P_2 to the inlet and outlet, respectively, of a pump.

where M_s is the saturation magnetization of the ferrofluid, and $L(\alpha)$ is the Langevin equation of (2.7) describing ferrofluid magnetization. Eq. (3.8) has the limiting cases

$$\bar{M} = \begin{cases} M_s, & \text{if } H \text{ is large (saturation)} \\ \dfrac{\chi H}{2}, & \text{if } H \text{ is small} \end{cases} \tag{3.9}$$

where χ is the magnetic susceptibility of (2.10).

With (3.7) in mind the experimental setup in Figure 3.5 was designed. A closed loop tubing system is investigated. The section of ferrofluid filled tubing between points P_1 and P_2 is held taut, and at a constant height z_o of 4.75 inches above the table. The two pressure transducers (P_1 and P_2) are separated by a length L of 34 cm. A permanent magnet with air gap distance L_g of 4.2 cm separating the two pole faces, each of circular diameter d equal to 3.9 cm, was used as the magnetic field source. A schematic of the magnet is shown in

Figure 3.5.

The straight section of tubing is placed so as to fit between the two pole faces, while being positioned off center horizontally, as illustrated in Figure 3.5. The reason for positioning the tube off center is that the magnetic field magnitude near the pole faces is greater than at a distance $L_g/2$, and thus by skewing the placement of the tube toward a pole face we apply the strongest field possible from the magnet. The field created by the magnet was measured by hand with a gaussmeter (F.W. Bell model 7030). The field within the gap L_g ranged from 1.4 kGauss to 2.1 kGauss due to fringing field effects, although the value at the center of the pole face, where the tubing is positioned, is approximately 1.5 kGauss. It was also noted that at a distance of approximately 8 cm from the edge of the pole faces the field value had dropped to roughly 30 Gauss. The spatial variation of H is what induces a body force on the ferrofluid. During experimentation the magnet is placed at 5 positions along the length L, specifically 0, $L/4$, $L/2$, $3L/4$, and L. In the data that follows, these positions are recorded as 0 cm, 8.5 cm, 17 cm, 23.5 cm, and 34 cm, respectively.

Three different fluids were used during experimentation; tap water, MSG W11 water-based ferrofluid, and EFH1 hydrocarbon-based ferrofluid. Three different flow rates were examined for each fluid, but only the case of static flow is strictly valid for theoretical comparison to (3.7) due to the inviscid assumption used in Bernoulli's equation. Thus we begin by describing the static flow experiment, where v in (3.7) can be set to zero. By applying (3.7) to the experimental setup the gravity dependent and velocity dependent terms will be the same at the points P1 and P2, and thus cancel. This leads to the relationship

$$\begin{aligned} P_1 - \mu_o \bar{M}_1 H_1 &= P_2 - \mu_o \bar{M}_2 H_2 \\ \Rightarrow P_1 - P_2 &= \Delta P = \mu_o (\bar{M}_1 H_1 - \bar{M}_2 H_2) \end{aligned} \tag{3.10}$$

Pressure Drop for Zero Flow Rate		
Fluid	**Position of Magnet (cm)**	**ΔP (p.s.i.)**
Tap Water	0.0	0.00
	8.5	0.00
	17.0	-0.01
	25.5	0.00
	34.0	0.00
MSG W11	0.0	-0.15
	8.5	0.00
	17.0	0.00
	25.5	0.00
	34.0	0.16
EFH1	0.0	-0.26
	8.5	0.03
	17.0	0.04
	25.5	0.06
	34.0	0.46

Table 3.6: The measured pressure drop between two points of tubing containing stationary fluid exposed to a dc magnetic field at various positions between the points of interest. The magnetic field strength is approximately 1.5 kGauss at the positions indicated. There was an initial offset value, $\Delta P \approx 0.5$ p.s.i., before experimentation began which was subtracted from all reported values.

where $\bar{M}$ is defined in (3.8).

The results shown in Table 3.6 demonstrate that tap water is not affected by the external magnetic field, as would be expected since water can not be magnetized, but that the two ferrofluids tested do show a noticeable effect. The listed values of ΔP constitute a change in pressure drop between P_1 and P_2 from the case of zero applied magnetic field. The lack of symmetry noticed for EFH1 is likely due to the difficulties in applying the same magnetic field at the points P_1 and P_2.

The experimental data can be compared with theoretical predictions by computing the

value of the term $\mu_o \bar{M} H$. We begin with the computation of $\bar{M}$ using (3.8)

$$\bar{M} = \frac{1}{H}\int_0^H M_s L(\alpha) dH = \frac{M_s}{H}\int_0^H \left[\coth(\alpha) - \frac{1}{\alpha}\right] dH \tag{3.11}$$

where

$$\alpha = \frac{m\mu_o H}{kT} = \frac{\mu_o M_d H V}{kT} \tag{3.12}$$

in which M_d is the domain magnetization of the magnetic material, $V = \frac{1}{6}\pi d^3$ is the spherical ferrofluid particle volume, k is Boltzmann's constant, and T is the temperature. Explicitly writing the magnetic particle volume allows α to be written as

$$\alpha = \frac{\pi \mu_o M_d H d^3}{6kT}. \tag{3.13}$$

The integral of (3.11) can be evaluated as

$$\frac{1}{H}\int_0^H M_s L(\alpha) dH = \frac{M_s}{H}\int_0^H \left[\coth(\alpha) - \frac{1}{\alpha}\right] dH \tag{3.14}$$

$$= \frac{6M_s kT}{\pi \mu_o M_d d^3 H}\left[\ln\sinh\left(\frac{\pi \mu_o M_d d^3 H}{6kT}\right) - \ln H\right]\Bigg|_0^H \tag{3.15}$$

$$= \frac{M_s 6kT}{\pi \mu_o M_d d^3 H}\left(\ln\left(\frac{\sinh\left[\frac{\pi \mu_o M_d d^3 H}{6kT}\right]}{H}\right)\right)\Bigg|_0^H \tag{3.16}$$

$$= \frac{M_s 6kT}{\pi \mu_o M_d d^3 H}\ln\left(\frac{6kT\sinh\left[\frac{\pi \mu_o M_d d^3 H}{6kT}\right]}{\pi \mu_o M_d d^3 H}\right). \tag{3.17}$$

Realizing that the expression evaluated at $H = 0$ can be simplified by using

$$\sinh(x) \approx x \qquad x \ll 1 \tag{3.18}$$

and canceling appropriate terms as well as using (3.10) leads to the final form of the magnetic field induced pressure drop

$$\Delta P = \frac{M_s 6kT}{\pi M_d d^3}\left(\left[\ln\left(\frac{\sinh\left[\frac{\pi \mu_o M_d d^3 H_1}{6kT}\right]}{H_1}\right)\right] - \left[\ln\left(\frac{\sinh\left[\frac{\pi \mu_o M_d d^3 H_2}{6kT}\right]}{H_2}\right)\right]\right) \tag{3.19}$$

where H_1 is the magnetic field value at P_1 and H_2 is the value at P_2. For the three most common experimental cases (3.19) can be simplified as

$$\Delta P = \frac{M_s 6kT}{\pi M_d d^3}\left(\left[\ln\left(\frac{\sinh\left[\frac{\pi\mu_o M_d d^3 H_1}{6kT}\right]}{H_1}\right)\right] - \left[\ln\left(\frac{\pi\mu_o M_d d^3}{6kT}\right)\right]\right) \qquad H_1 \neq 0 \;\; H_2 \approx 0 \quad (3.20)$$

$$\Delta P = \frac{M_s 6kT}{\pi M_d d^3}\left(\left[\ln\left(\frac{\pi\mu_o M_d d^3}{6kT}\right)\right] - \left[\ln\left(\frac{\pi\mu_o M_d d^3}{6kT}\right)\right]\right) = 0 \qquad H_1 \approx 0 \;\; H_2 \approx 0 \quad (3.21)$$

$$\Delta P = \frac{M_s 6kT}{\pi M_d d^3}\left(\left[\ln\left(\frac{\pi\mu_o M_d d^3}{6kT}\right)\right] - \left[\ln\left(\frac{\sinh\left[\frac{\pi\mu_o M_d d^3 H_2}{6kT}\right]}{H_2}\right)\right]\right). \qquad H_1 \approx 0 \;\; H_2 \neq 0 \quad (3.22)$$

Since the magnetic field of the permanent magnet was measured to be very small at a distance of 8 cm from the edge of the pole face, approximately 30 Gauss, the three cases listed above are used for comparison to the experimental results. Additionally, examination of (3.21) indicates the need of a gradient-field to produce a pressure drop. If H is the same at both P_1 and P_2 then M will also be the same at these points and ΔP will be zero. By plugging in appropriate values of the constants, as determined in the discussion of ferrofluid magnetization in Chapter 2, we can get the theoretical value of the pressure drop. It is noted that for the same magnetic field value the calculated pressure drop using (3.20) and (3.22) has the same magnitude but opposite sign. Values corresponding to MSG W11 ferrofluid include $\mu_o M_d = 0.56$ Tesla, $\mu_o M_s = 0.01873$ Tesla, $T = 299$ K, and $\mu_o H = 0.15$ Tesla. We consider three different values of particle size determined during magnetization experiments. The three values from Table 2.6 are $d_{min} = 6$ nm, $d_{avg} = 8$ nm, and $d_{max} = 12$ nm. Thus, the predicted value of pressure drop, in units of Pa, can be in the range from 0.09 p.s.i. to

0.25 p.s.i. found by using d_{min} and d_{max}, with an expected average of 0.17 p.s.i. found using d_{avg}. These values agree well with the 0.15 and 0.16 p.s.i. pressure drop magnitudes found experimentally and listed in Table 3.6.

Although the method just used for calculating a theoretical pressure drop agreed well with the experimental data, it was dependent upon choosing a ferrofluid particle size. A method for gross approximation of the pressure drop, independent of this choice of particle size, uses the fact that the calculation of $\bar{M}$ involves taking the area under the magnetization curve. Mathematically this is

$$P = \mu_o \frac{1}{H} \times (\text{area under magnetization curve}) \times \text{H}. \tag{3.23}$$

The area under the magnetization curve can be approximated with a lower bound by estimating the magnetization to be a linear function of H, and therefore taking the area of the triangle connecting the origin and the point of interest. Similarly, the upper bound can be taken by estimating the magnetization to be a constant, independent of H. The area under the magnetization curve would then simply be the area of the rectangle with vertices at (0,0), (0,M), (H,0), and (H,M). Using these two methods with the value of magnetization for MSG W11, determined by the experiments of Chapter 2, to be 135 Gauss at a field strength of 1.5 kGauss, we get a lower limit of 0.12 p.s.i., and an upper limit of 0.24 p.s.i. Again, these numbers bound the measured values.

The same two theoretical calculations may be used for comparing the experimental and theoretical data of EFH1 ferrofluid. Using (3.20) and (3.22) with the three particle sizes, $d_{min} = 7$ nm, $d_{avg} = 11$ nm, and $d_{max} = 13$ nm, as given in Table 2.6, the theoretical pressure drops are 0.25 p.s.i., 0.46 p.s.i. and 0.52 p.s.i. respectively. The values of the constants used in

the calculation are the same as those for MSG W11 except that now $\mu_o M_s = 0.03652$ Tesla. Using (3.23) with the previously measured value of $\mu_o M = 0.0298$ Tesla at $\mu_o H = 0.15$ Tesla gives lower and upper bounds for the pressure drop of 0.26 and 0.52 p.s.i. The experimental values do fall within this range. It is noted that for all magnet positions other than 0 cm and 34 cm the recorded pressure drops are almost 0 p.s.i., as would be predicted by (3.21).

It has been shown that the current experimental setup is well described by the ferrohydrodynamic Bernoulli equation with application of a gradient field between two points. Experimental data was also taken for the case of non-zero flow rate, which should not be compared to Bernoulli's equation because the flow has low Reynolds number and therefore viscosity is important, but which did result in a similar trend to that of the stationary fluid experiment described. With or without fluid flow a noticeable effect on pressure drop was only seen when the permanent magnet was placed directly over P_1 or P_2. When the magnet is placed at other positions along the tubing length the value of H at P_1 and P_2 is approximately the same, zero, and thus no pressure drop is induced, as required by (3.21).

3.3 Magnetic Field Effects in Ferrofluid Tubing Flows

3.3.1 Magnetic Field Tangential to Flow

The motivation for this set of experiments was to compare and understand previous work by Energy International (EI) which examined applications of ferrofluids to power transformers. In contrast, the experiments of this chapter will be used to consider the possibility of designing ferrofluid pumps which create volumetric flow without the need for mechanical forces. The results of the EI work demonstrated that when ferrofluid was mechanically pumped through closed tubing, the pressure drop between two points could be raised by

Experimental Conditions for Ferrofluid Tubing Flow					
Researcher	***H* Direction** (to flow)	***H* Magnitude** (Gauss)	**Frequency** (Hz)	**Flow rate** (L/min)	**Result** (% ΔP)
EI	Tangent	150-1,500	60, 400, 1000	0.33-1.4	+13.6
Author	Tangent	0-2000	dc, 60	0-2	Null
EI	Perpendicular	150-1,500	60, 400, 1000	0.33-1.4	+23,-9.1
Author	Perpendicular	0-2000	dc, 60	0-2	Null
EI	Traveling wave	11	60	0.550	Null

Table 3.7: A tabular comparison of the experiments conducted by Energy International (EI) and the present author. The flow rates investigated in this thesis were laminar, while EI studied both laminar and turbulent flow regimes. EI uses a single water-based ferrofluid with $\mu_o M_s = 150$ Gauss, while this thesis focuses on work with an oil-based ferrofluid with $\mu_o M_s = 365$ Gauss, and a water-based ferrofluid with $\mu_o M_s = 187$ Gauss. The overlap of certain experimental parameters allows for comparison of the results from the separate experiments.

applying a solenoidal magnetic field linearly polarized in the direction of flow. Experiments were completed in both laminar and turbulent regimes, and indicated that the maximum magnetically induced increase in pressure drop was 13.6% [19]. A decrease in pressure drop was not reported. Table 3.7 lists the different experiments conducted in this thesis and by EI.

The experimental setup in this thesis consisted of non-magnetic flexible tubing fed through the air gap of two electromagnets placed side-by-side. A schematic of one electromagnet is shown in Figure 3.6. Two pressure transducers were placed in the flow loop on opposite sides of the electromagnets and the pressure difference between the two points recorded. The pressure drop was measured as a function of volumetric flow rate, magnetic field strength, and magnetic field frequency for the case of an oscillating field. A gaussmeter probe was taped to the tubing allowing measurement of the magnetic field along the axis of the electromagnets,

as well as being positioned approximately in the center of the magnets so as to record the maximum value of magnetic field applied. The data shown in Figure 3.7 clearly indicates that the pressure drop across the length of tubing was not affected by the application of an external dc magnetic field. The results for tap water and MSG W11 are similar and are given in tabular form in Appendix C.1.

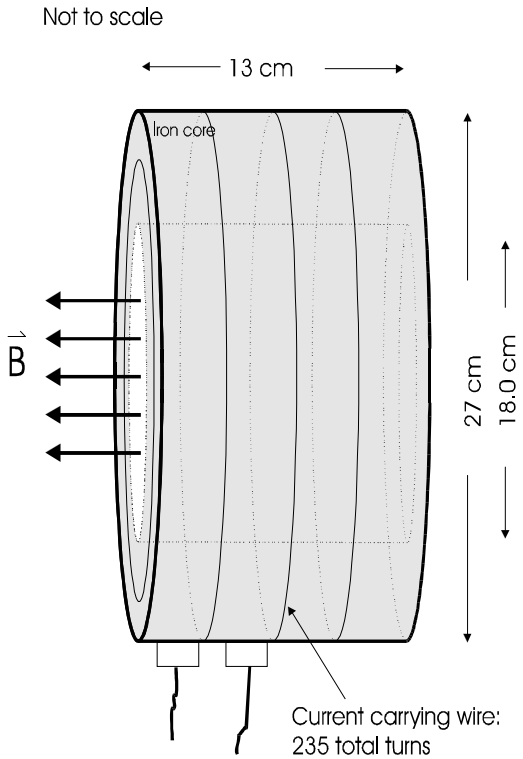

Figure 3.6: A schematic of the electromagnet used in the ferrofluid tubing flow and sheet flow experiments. The magnetic field is approximately 20 Gauss per ampere as measured at the radial and axial center of the magnet in air.

A qualitative measurement was also made with a 60 Hz oscillating magnetic field up to a strength of 115 Gauss rms. Magnetic field strengths much larger than this could not be generated by the available equipment. Additionally, fields above this value tended to cause

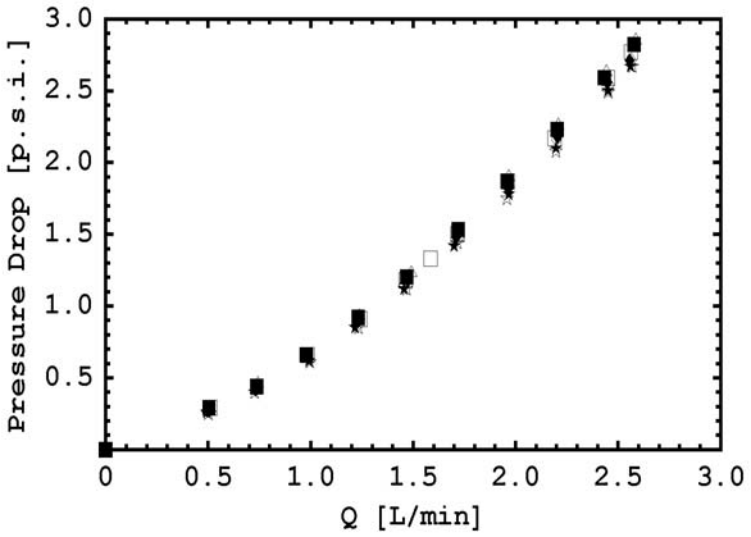

Figure 3.7: Measured pressure drop vs. flow rate for EFH1 hydrocarbon-based ferrofluid in the presence of an external dc magnetic field oriented parallel to the direction of flow. The magnetic field strengths are represented by: star-0 gauss, solid star-50 gauss, diamond-100 gauss, solid diamond-150 gauss, box-200 gauss, solid box-250 gauss, triangle-300 gauss.

large fluctuations in the flow meter output by inducing eddy currents within the instrument. As with the case of the dc magnetic field, preliminary data indicated no change in pressure drop with an applied oscillating magnetic field, and thus extensive data was not taken.

3.3.2 Magnetic Field Perpendicular to Flow

The work of Energy International again served as a basis for the experimental setup. Using a similar configuration to the one used here and shown in Figure 3.8 they observed cases of magnetically induced pressure increase or decrease when a magnetic field linearly polarized perpendicular to the direction of the flow was applied. The maximum pressure increase they report was 23%, while the maximum decrease was 9.1% [19].

The data collected for EFH1 ferrofluid are plotted in Figure 3.9. As the figure indicates

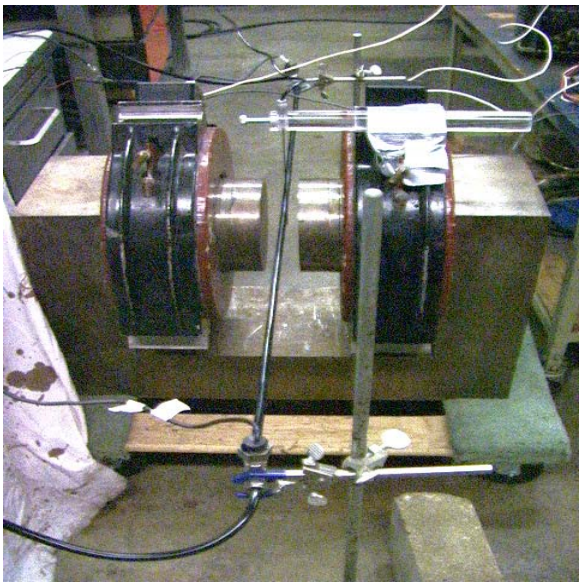

Figure 3.8: A magnetic field is applied in a direction perpendicular to the direction of mechanically forced flow. The first pressure transducer is in the bottom foreground of the picture, while the second is toward the top center of the frame. The magnetic field is applied from left to right in the frame, and a gaussmeter probe is suspended in the air gap next to the tubing.

there is not a strong dependence of pressure drop on the strength of the applied magnetic field. The very small effect seen may be due to gradients in the applied field as has been shown to cause pressure drops as discussed in section 3.2. Experimental data of EFH1 and MSG W11 are given in tabular form in Appendix C.2.

3.3.3 Experimental Comparison and Explanation of the Null Results

EI measured non-zero magnetic field induced pressure drops that were not replicated during the experiments of this thesis. EI did use a water-based ferrofluid with saturation magnetization of about 150 Gauss, comparable to the MSG W11 ferrofluid used here, but much weaker

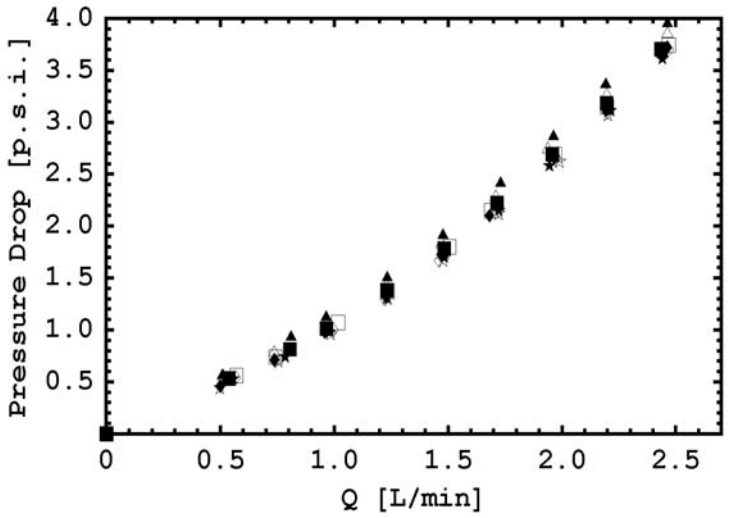

Figure 3.9: Measured pressure drop vs. flow rate for EFH1 hydrocarbon-based ferrofluid in the presence of an external dc magnetic field applied in a direction perpendicular to the direction of flow. The magnetic field strengths are represented by; star-0 gauss, solid star-100 gauss, diamond-200 gauss, solid diamond-300 gauss, box-400 gauss, solid box-500 gauss, triangle-1000 gauss, and solid triangle-2000 gauss.

than the 400 Gauss EFH1 ferrofluid used here. The frequency ranges and flow rates are not easily compared between experiments. EI used smaller diameter tubing than that used here, and thus many of the flow rates they used were turbulent. EI also performed a gradient-field test and found that their apparatus was not subject to large gradient-magnetic-field-induced pressure drops. However, application of a gradient field was the only way in which the experiments of this thesis were shown to exhibit a pressure drop or increase. As such the observations indicate that non-mechanical ferrofluid pumping is not induced by application of a dc magnetic field parallel or perpendicular to the tube flow direction. It is likely that the differing results of the experiments of EI and this investigator are due to various differences in the experimental setup for each case. The experiments done are not conclusive however,

and future work should strongly consider a much wider array of experimental parameters, particularly magnetic field amplitudes and frequencies.

3.4 Preliminary Investigation of a Ferrofluid Pump

Previous work [34] indicates that a ferrofluid drop placed in a circular grooved track, wider than the drop diameter, will move along the circular track when exposed to a rotating magnetic field imposed by a stator motor winding. In an attempt to build on this work, a grooved track was made that was not a complete circle, but instead terminated at both ends by a circular reservoir, as shown in Figure 3.10. Reservoir A was filled to a height of approximately 1/4 inch with ferrofluid while the channel and reservoir B remained empty. A spatially uniform rotating magnetic field was then applied using a 2-pole stator winding with the purpose of moving the ferrofluid from reservoir A to reservoir B. It was observed that some of the ferrofluid could be moved, but that after a short time the amount of fluid in reservoir A and reservoir B was approximately equal and would remain so indefinitely. Even so, the motion of the fluid was magnetic field induced, as the fluid moved between the reservoirs at much greater speed than could be created by the vertical pressure difference within the fluid column of reservoir A. Observations also showed that the fluid along the inner wall would co-rotate with the magnetic field, while fluid on the outer wall would counter-rotate with the magnetic field, as shown schematically in Figure 3.11. Starting in reservoir A, the fluid would proceed along the inner channel wall to reservoir B, and then back again along the outer channel wall, with a net mass flux of zero through any cross-section of the channel. The parameters tested were not exhaustive, yet the findings were independent of magnetic field rotation direction, rotation frequency (0-500 Hz), magnetic field magnitude,

and the ferrofluid type (both water-based and oil-based were used).

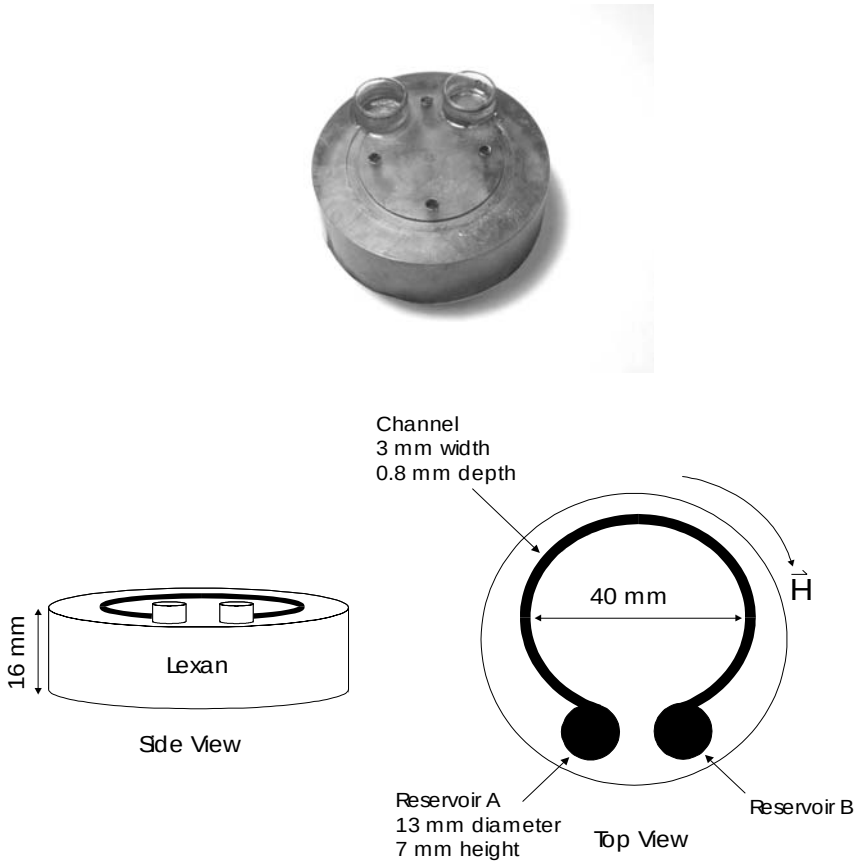

Figure 3.10: A magnetic field based design of a ferrofluid flow channel. The spatially uniform, rotating magnetic field is applied in-plane with the channel. Fluid flows through the channel along the channel walls, with a net zero volume flux. Note that the photograph is of an early version of the pump in which the channel entered the reservoirs perpendicularly, while the sketch depicts a design in which the channel enters the reservoirs tangentially. Both designs were used experimentally with similar results.

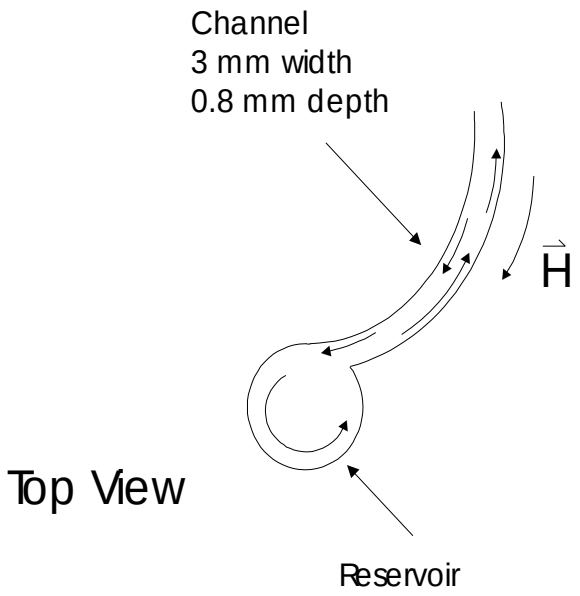

Figure 3.11: A close-up view of the channel of the ferrofluid pump of Figure 3.10. The arrows within the channel and reservoir indicate the direction of flow corresponding to the indicated direction of magnetic field rotation. The behavior suggests that ferrofluid particles are rolling along the channel walls, inducing flow in the direction of the rolling motion.

A theoretical investigation similar to the experiments just described offers some insight into the net zero flow results. Rinaldi and Zahn modeled the case of a rectangular duct (width s) of ferrofluid mechanically driven and exposed to a spatially uniform rotating magnetic field [20]. The key points of that analysis will be summarized here. They begin with the ferrofluid magnetic relaxation equation

$$\frac{\partial \vec{M}}{\partial t} + (\vec{v} \cdot \vec{\nabla})\, \vec{M} - \vec{\omega} \times \vec{M} + \frac{1}{\tau}[\vec{M} - \chi_o \vec{H}] = 0 \tag{3.24}$$

for which $\vec{M}$ is the time dependent fluid magnetization, $\vec{v}$ is the fluid velocity, $\vec{\omega}$ is the particle spin velocity, $\tau = \tau_{eff}$ is the effective relaxation time of (2.20), and χ_o is the

effective magnetic susceptibility. Applying a spatially uniform rotating magnetic field

$$\vec{H} = Re\left[\left(\hat{H}_x\hat{x} + \hat{H}_z\hat{z}\right)e^{j\Omega t}\right] \tag{3.25}$$

in which Ω is the frequency of oscillation, and using the torque density, $\vec{T} = \mu_o\left(\vec{M} \times \vec{H}\right)$, leads to the approximate time-average torque in the small spin velocity limit

$$\langle T_y \rangle = T_o + \alpha\omega_y, \qquad \omega_y\tau \ll 1 \tag{3.26}$$

where T_o and α are complicated functions of H_x, H_z, τ, Ω, and χ_o. The authors then postulate a system operating in the creeping flow limit, i.e. inertia is negligible, and arrive at an expression for the flow velocity within the channel

$$\begin{aligned} v_z(x) &= \frac{x(x-s)}{2\eta_{eff}}\frac{\partial p'}{\partial z} \\ &+ \frac{(\eta_{eff}-\eta-\zeta)}{2\square(\eta+\zeta)\eta_{eff}}\left(\frac{\partial p'}{\partial z}\left[\frac{(1+\cos\square s)(1-\cos\square x)-\sin\square s\sin\square x}{\sin\square s}s\right]\right. \\ &+ \left.\frac{\eta_{eff}T_o}{s\zeta}\left[\frac{(1-\cos\square s)(2x-s+s\cos\square x)-s\sin\square s\sin\square x}{\sin\square s + 2\frac{(\eta_{eff}-\eta-\zeta)}{\square s(\eta+\zeta)}(1-\cos\square s)}\right]\right) \end{aligned} \tag{3.27}$$

for which η_{eff} is the effective ferrofluid viscosity, η is the dynamic viscosity, $\zeta = \frac{3}{2}\eta\phi$ is the vortex viscosity, ϕ is the volume fraction of magnetic solid particles to carrier liquid and surfactant, and $\dfrac{\partial p'}{\partial z}$ is the pressure gradient. The parameters $\square$ and η_{eff} are defined as

$$\square = \left(\frac{4\zeta^2\eta_{eff}}{(\eta_{eff}-\eta-\zeta)(\eta+\zeta)\eta'}\right)^{1/2} \tag{3.28}$$

$$\eta_{eff} = \eta + \frac{a\zeta}{\alpha - 4\zeta} \tag{3.29}$$

where η' is called the spin viscosity. By integrating over the channel width, s, they arrive at an expression for the flow rate. Interestingly, the velocity term containing T_o integrates to

zero, thus the flow rate Q is

$$Q = \int_o^s v dx = \frac{s^3}{12\eta_{eff}} \frac{\partial p^{'}}{\partial z} \left[1 + 6 \frac{\eta_{eff} - \eta - \zeta}{(\square s)^2(\eta + \zeta)} \left(2 - \frac{\square s(1 + \cos \square s)}{\sin \square s} \right) \right]. \tag{3.30}$$

If the pressure gradient, $\frac{\partial p'}{\partial z}$, is set to zero, as in the ferrofluid pump experiments of Figure 3.10, then the net flow rate is zero. Experimentally we see the same result, with flows in opposite directions that produce a net flow of zero. It seems likely that the reason Rinaldi and Zahn arrive at a net zero magnetic field induced flow rate is because of the circulating flow in the channel, as observed in the experiments of this section.

3.5 Discussion

This chapter began with a brief characterization of fluid parameters, including density, viscosity, surface tension, Reynolds number, and entrance length. Experiments were conducted in which magnetic and non-magnetic liquids were mechanically forced through a tubing system, while simultaneously being exposed to a magnetic field either parallel or perpendicular to the flow direction. The magnetic source was placed symmetrically between two pressure transducers and the pressure drop across the length of tubing measured as a function of flow rate and magnetic field strength. There was no observed magnetic field induced pressure change. The null results of the experiments using an applied magnetic field parallel or perpendicular to the ferrofluid flow through a closed tubing system are in contrast with the findings of Energy International (EI) [19], who recorded magnetic field induced pressure decreases and increases for similar experiments. The experiments of this chapter were repeated several times, all producing the same null result. It is possible that the magnetic effects reported by EI were caused by asymmetries in the magnetic field, i.e. gradient field

effects. The application of gradient fields non-symmetrically located about the position of the pressure transducers was the only situation in which this author could replicate a magnetic field induced pressure change. While the magnetic field magnitudes used by EI were up to 3 times larger than those used here, the water-based ferrofluid EI used had a saturation magnetization of $\mu_o M_s = 150$ Gauss, significantly smaller than that of the EFH1 used for the experiments of this chapter. The data taken here indicated that magnetic field pumping of ferrofluid is not possible with linearly polarized magnetic fields. Future experiments should rigorously investigate a much broader range of magnetic field magnitudes and frequencies.

A design for a macro-scale ferrofluid pump was presented and tested. The experimental observations indicate that a spatially uniform rotating magnetic field cannot be used to pump ferrofluid in open-channel flow with a non-zero flow rate, but that fluid circulation within the channel system is easily obtained. Zahn and Rinaldi have developed theory for the planar duct analog to the described experiments, which predicts no magnetically induced change in volumetric flux [20] above the already present mechanical-forced flow. Their prediction is in agreement with the findings here.

The distinction between net flow and fluid motion is important. The experiments of open channel flow with a ferrofluid provide clear evidence that ferrofluids can be induced into motion by spatially uniform rotating magnetic fields. Such a system, if scaled down, may be used as a MEMS mixer or fluid circulator, with the intent of stirring small amounts of fluids that otherwise may not mix. There may also be potential applications to devices for cooling and enhanced heat transfer. It should also be pointed out that while volumetric mass flow was not obtained using dc magnetic fields, or spatially uniform rotating magnetic fields, application of spatially non-uniform rotating or traveling wave magnetic fields may

properly create a net volume ferrofluid flow. This area should receive future consideration.

Chapter 4

Ferrofluid Sheets and Jets

The behavior of ferrofluid jets impacting a solid circular surface to create an expanding sheet flow in the presence of applied direct current (dc) and alternating current (ac) magnetic fields is investigated for experimental configurations with an applied magnetic field either parallel or perpendicular to the cylindrical jet axis. The experiments lead to a set of new and non-intuitive results in the field of free surface flows, and are explained qualitatively and theoretically where possible. Although this section of the thesis was not undertaken with an express interest in MEMS applications, a few of the results may lend themselves to future attempts to understand micro-fluidic jets.

4.1 Introduction

Thin liquid sheets may be generated when a laminar jet strikes a solid circular surface, as shown in Figure 4.1 [35, 36, 37]. Upon impact the fluid is ejected radially outward in the form of a thin sheet. The sheet has a radius much greater than the radius of both the impacting surface and initial jet, and takes a circular form if the initial jet has a circular cross-section and the angle of impact is 90^o. There is a lip on the surface of impact with an adjustable

height that controls the angle between the sheet and impactor at the point of separation. This angle is termed the take-off angle and is shown in Figure 4.2, with a photograph of the adjustable lip in Figure 4.3. Raising or lowering the adjustable lip controls the take-off angle, and thus allows for selection of the resulting sheet shape between a stable expanding sheet and a sagging sheet or bell.

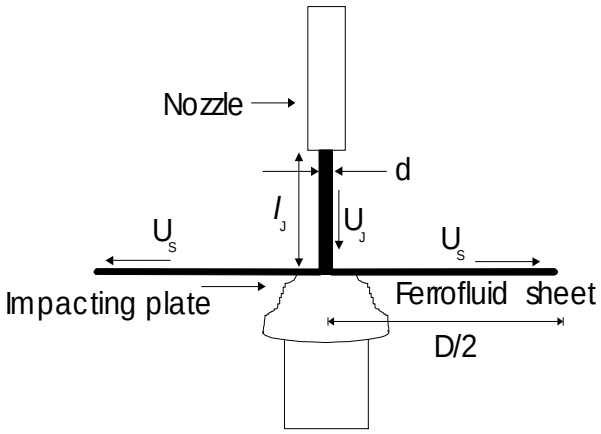

Figure 4.1: The experimental configuration used with a jet impacting a solid surface to form a radially expanding thin sheet. U_J is the velocity of the jet, U_s is the velocity within the sheet, l_J is the jet length, d is the diameter of the jet, and D is the diameter of the sheet. The entire flow is housed in a 6 inch wide hexagonal test cell, seen in Figures 4.8 and 4.18.

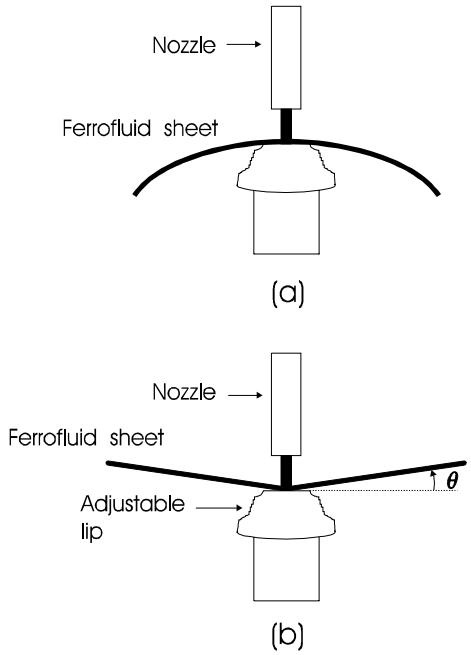

Figure 4.2: (a)When the adjustable lip is lowered the take-off angle θ is slightly negative and the resulting flow can take a sagging or bell shape, but (b) when the lip is raised, $\theta \geq 0$, the resulting flow is an expanding thin circular sheet [35].

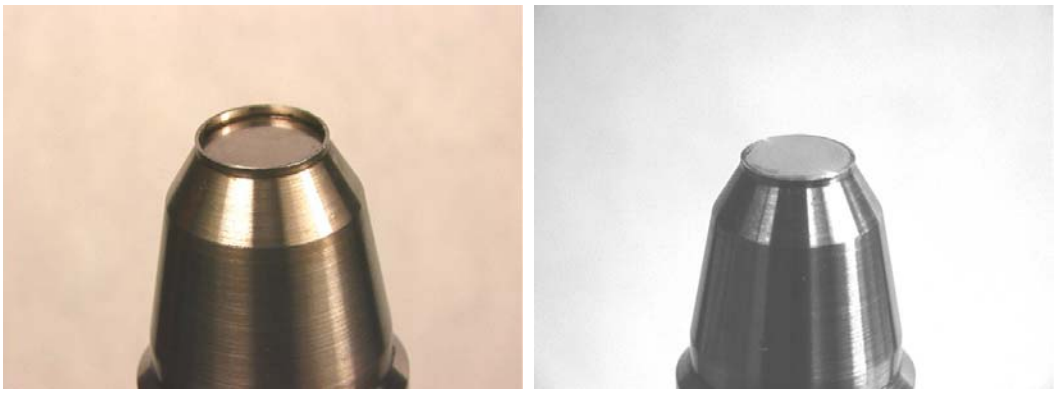

Figure 4.3: (Left) The impactor shown with a raised lip. (Right) Lowered lip. The diameter of the impacting plate is 10 mm, and the thickness of the lip adds 1 mm to the radius all the way around with an adjustable height from zero to ~ 3 mm.

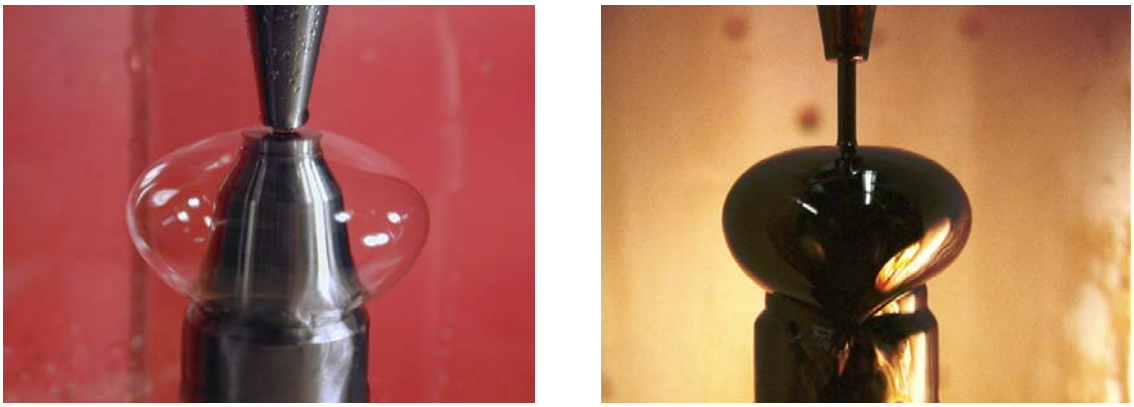

Figure 4.4: The influence of gravity is sometimes important in the case of waterbells. (Left) A traditional waterbell viewed from the side. (Right) A ferrofluid bell viewed from the side.

The system is governed by three dimensionless groups which prescribe the relative importance of forces acting on the sheet. Neglect of gravity is justified by examination of the dimensionless Froude number, which is defined as

$$\text{Froude Number} = Fr = \frac{U_s^2}{gD} = \frac{\text{inertial force}}{\text{gravitational force}} \tag{4.1}$$

where U_S is the velocity within the sheet, g is the gravitational acceleration constant, and D is the diameter of the sheet. Using Table 4.1 and taking values representative of our experiments, $U_s = 170$ cm/sec, $g = 980$ cm/s^2, and $D = 2$ cm gives $Fr \approx 10$ indicating inertial forces are an order of magnitude larger than gravitational forces. Gravity does play a role in the case of related sagging sheets and water bells [36], which are not the focus of this work, but of which two examples are shown in Figure 4.4. In these cases gravity acts to pull the sheet downward, and it eventually closes upon itself forming a hollow bell of water. The magnitude of the gravitational effect is not always large, however, and the dynamics of bell formation can proceed even in cases where gravity is negligible [36].

Two more dimensionless groups describing the system are the Reynolds number, and the

Quantity	Symbol	Value	Units
Volumetric Flow Rate	Q	0.5-1.0	L/min
		8-17	cm^3/sec
Fluid Velocity	U_J, U_s, U	170-340	cm/sec
Jet Length	l_j	1-30	mm
Jet Diameter	d	2.5	mm
Ferrofluid Density	ρ	1.17	g/cm^3
Ferrofluid Dynamic Viscosity	η	≈ 5	centipoise (cP)
Ferrofluid Surface Tension	σ	0.026	N/m
		26	dyne/cm
Froude Number	Fr	~ 10	dimensionless
Reynolds Number	Re	$\sim 10^3$	dimensionless
Weber Number	We	$\sim 10^3$	dimensionless
Permeability of Free Space	μ_o	$4\pi \times 10^{-7}$	henry/m
Relative Ferrofluid Permeability	$\mu_r = \frac{\mu}{\mu_o}$	2.6	dimensionless

Table 4.1: Physical parameters and dimensions for the experimental investigations of ferrofluid jets and sheets with EFH1 hydrocarbon-based ferrofluid.

Weber number, defined as

$$\text{Reynolds Number} = Re = \frac{\rho U_J d}{\eta} = \frac{U_J d}{\nu} = \frac{\text{inertial force}}{\text{viscous force}} \tag{4.2}$$

$$\text{Weber Number} = We = \frac{\rho U_s^2}{\sigma/d} = \frac{\rho d U_s^2}{\sigma} = \frac{\text{inertial force}}{\text{surface tension force}}. \tag{4.3}$$

In (4.2) and (4.3), ρ is the mass density of the fluid, U_J is the jet speed at impact, d represents the diameter of the jet, η is the dynamic viscosity of the fluid, $\nu = \eta/\rho$ is the kinematic viscosity, and σ is the interfacial surface tension. Again substituting representative values from Table 4.1 of $U_J = 170$ cm/sec, $d = 0.25$ cm, and $\nu = 0.05$ cm^2/sec, gives $Re \approx 10^3$, allowing us to neglect viscous effects.

Two types of sheet can arise according to the magnitude of We: 1) for $We < 1000$ a

circular form with well-defined edges, referred to as the smooth regime [37, 38, 39], and 2) for $We > 1000$ an unstable flapping sheet whose edges are much less well defined [38]. The two regimes are significantly different in that for the smooth regime the sheet radius increases linearly with We, while in the flapping regime the sheet radius decreases approximately as $We^{-1/3}$ [37]. Note in Figure 4.1 that U_s is the velocity of fluid within the sheet, and U_J is the velocity within the incident jet. These two values differ slightly due to an energy loss at the point of jet impact, however experimental work [37] has shown that depending on the fluid parameters the velocity within the sheet is commonly 90% of the jet velocity, so that for our purposes the velocity of the system from this point on is referred to as $U_J = U_s \equiv U$. A mathematical formulation of the sheet radius in both the smooth and flapping regimes that takes into account energy loss at the point of impact will not be given here, as we assume lossless conditions, but can be found in previous work [37, 38].

4.1.1 Smooth Sheets

The smooth regime of circular liquid sheets is well understood experimentally and theoretically [37, 40, 41]. Specifically, the sheet thickness and radius can be predicted. An important property of these flows is that the velocity within the sheet has been experimentally shown to be approximately constant [37]. Thus, as a consequence of mass conservation the sheet necessarily thins as one moves from the sheet center to the sheet edge

$$Q = \frac{\pi U_J d^2}{4} = 2\pi r h U_s = \text{constant} \tag{4.4}$$

where Q is the volumetric flow rate, r is the radial position within the circular sheet, and h is the sheet thickness. Rearranging terms in (4.4) and using $U_J = U_s = U$ gives the sheet

thickness as a function of radius

$$h(r) = \frac{Q}{2\pi r U}. \tag{4.5}$$

Using values from Table 4.1 of $Q = 1.0$ L/min, and $U = 3.40$ m/s, as well as a typical sheet radius of $r = 0.01$ m indicates $h \approx 0.1$ mm.

The Taylor Radius

The sheet radius may be approximated by considering the dominant forces acting within the system, namely inertia, F_I, and curvature-dependent surface tension, F_c. Viscous forces are neglected due to the large Reynolds number. Gravitational forces are neglected due to a large Froude number. Balancing inertia and surface tension at the sheet edge indicates

$$F_c \approx F_I \qquad \text{at} \;\; \mathrm{r} = \mathrm{r_T} \tag{4.6}$$

$$2\sigma \approx \rho U^2 h(r = r_T) \tag{4.7}$$

$$\Rightarrow r_T \approx \frac{\rho U Q}{4\pi\sigma} \tag{4.8}$$

where σ is the surface tension of the fluid, and r_T is called the Taylor radius. Realizing that $Q = \pi d^2 U/4$ and recalling (4.3) produces the linear dependence on Weber number [37]

$$r_T \approx \frac{We \;\; d}{16}. \tag{4.9}$$

Fluid flows from the point of jet impact to the Taylor radius and then is ejected outward in the form of droplets. In the smooth regime the drops are ejected in a regular manner.

Bernoulli's Method

A more formal development of the predicted sheet radius entails application of Bernoulli's equation to the schematic in Figure 4.5. Firstly, we note that at point a the curvature of

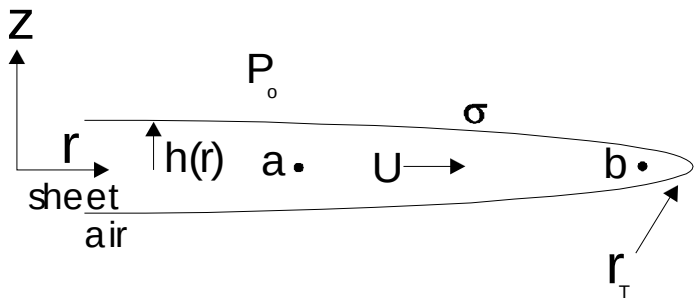

Figure 4.5: Application of Bernoulli's equation to a radially expanding fluid sheet of thickness h. The sheet flows with radial velocity U through an ambient fluid of atmospheric pressure p_o, extending to the Taylor radius, r_T. Surface tension, σ, acts everywhere at the sheet surface.

the sheet is small so that we approximate $p_a \approx p_o$, where p_o is atmospheric pressure. Next we apply Bernoulli's equation, (3.6), at points a and b

$$p_a + \frac{1}{2}\rho U_a^2 + \rho g z_a = p_b + \frac{1}{2}\rho U_b^2 + \rho g z_b. \tag{4.10}$$

Since $z_a = z_b$ these gravity terms drop out of the equation. Further, at the edge of the sheet we may define $U_b \approx 0$, which leaves

$$p_a + \frac{1}{2}\rho U_a^2 = p_b = p_o + \frac{1}{2}\rho U_a^2. \tag{4.11}$$

As mentioned earlier, the velocity within the sheet is approximately constant, however there is an acceleration period and deceleration period near the point of impact and near the Taylor radius, respectively. Thus setting $U_b \approx 0$ is consistent with our assertion of generally constant velocity within the sheet.

We can also formulate the pressure at point b in terms of the surface tension as

$$p_b = p_o + \sigma\left(\frac{1}{r_1} + \frac{1}{r_2}\right) \tag{4.12}$$

in which $r_1 \approx h(r = r_{max})$ is the first radius of curvature, and $r_2 = r_{max}$ is the second radius of curvature, corresponding to the maximum radial extension of the sheet. Since $r_2 \gg r_1$ we can ignore the r_2 term and write

$$p_b = p_o + \frac{\sigma}{r_1} = p_o + \frac{\sigma}{h(r = r_{max})}. \tag{4.13}$$

Using (4.5) and (4.13) in (4.11) results in

$$p_o + \frac{2\pi r_{max} U \sigma}{Q} = p_o + \frac{1}{2}\rho U_a^2 \tag{4.14}$$

in which $U_a = U$ since the velocity within the sheet is approximately constant. Solving (4.14) for r_{max} yields

$$r_{max} = r_T = \frac{\rho U Q}{4\pi\sigma} \tag{4.15}$$

which is the Taylor radius, r_T, found by scaling arguments in (4.8).

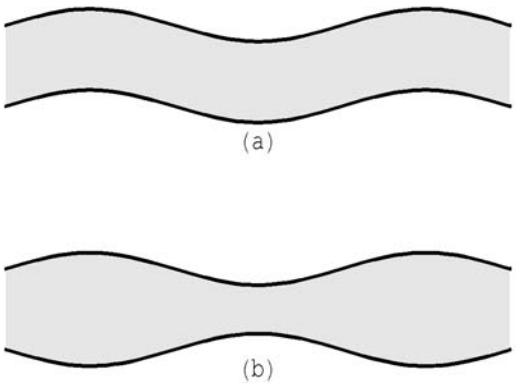

Figure 4.6: (a) Anti-symmetric and (b) symmetric modes of oscillation for interfacial waves on a fluid sheet.

4.1.2 Flapping Sheets

Previous work has shown that a thin fluid sheet may support two types of waves, symmetric and anti-symmetric as shown in Figure 4.6 [38, 40, 41].

Anti-symmetric capillary waves may be generated in which the upper and lower surfaces of the sheet oscillate in phase with each other. Symmetric waves may also be generated producing oscillations of the upper and lower surfaces which are 180^o out of phase with each other [41]. The presence of surface waves is often detectable by eye as shown in Figure 4.7.

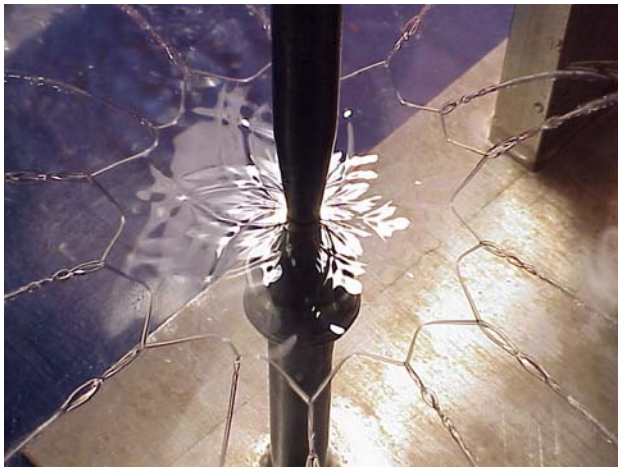

Figure 4.7: By proper choice of fluid properties two details of fluid sheet flows can be enhanced. First, the presence of capillary waves is clearly visible near the center of the sheet surface. Secondly, the sheet forms sharp points from which fluid jets are ejected. Picture by J. W. M. Bush [42].

In the smooth regime these small-signal sheet waves are present but are not sufficiently amplified in the short travel time from the sheet center to the sheet edge to be dynamically significant. Therefore they do not significantly effect the sheet radius as given by (4.8). However, as the fluid velocity is increased the surface wave oscillations become very large

due to the Kelvin-Helmholtz instability described in section 4.2.4, causing the sheet to break up before it is able to reach the Taylor radius. The breakup of the sheet into drops also becomes less regular than in the smooth regime and the sheet edges become blurred. There may be an accompanying auditory crackling since the wavelength of the instability is within the appropriate range of human hearing [38], which is approximately 20-20,000 Hz [43, p. 444]. The flapping regime will be discussed further in section 4.2.4.

4.2 Magnetic Field Effects

We now extend the dynamics considered in section 4.1 through use of a laminar ferrofluid jet with magnetic permeability μ in an imposed magnetic field. Magnetic field orientations along and perpendicular to the jet axis are investigated and considered in turn in what follows.

4.2.1 Experiment 1: Magnetic Field Perpendicular to Jet Axis

Deformation of the Sheet

A magnetic field is applied in a direction perpendicular to the flow of the incoming jet, and thus in-plane with the sheet flow, as shown in Figure 4.8. The magnetic field is produced by means of two coils, each of 235 turns, placed on either side of the acrylic test cell housing the flow. Figure 4.9 shows a series of photographs which demonstrate the behavior of the initially circular sheet ($\mid \vec{B} \mid = 0$) with increasing magnetic field strength. The sheet deforms by contracting in the direction parallel to the applied field and elongating in the direction perpendicular to the applied field. The resulting shape can be approximated by an ellipse with major axis perpendicular to the field and minor axis parallel. The surface of the sheet transitions from its initially smooth profile to a more complex pattern of capillary waves,

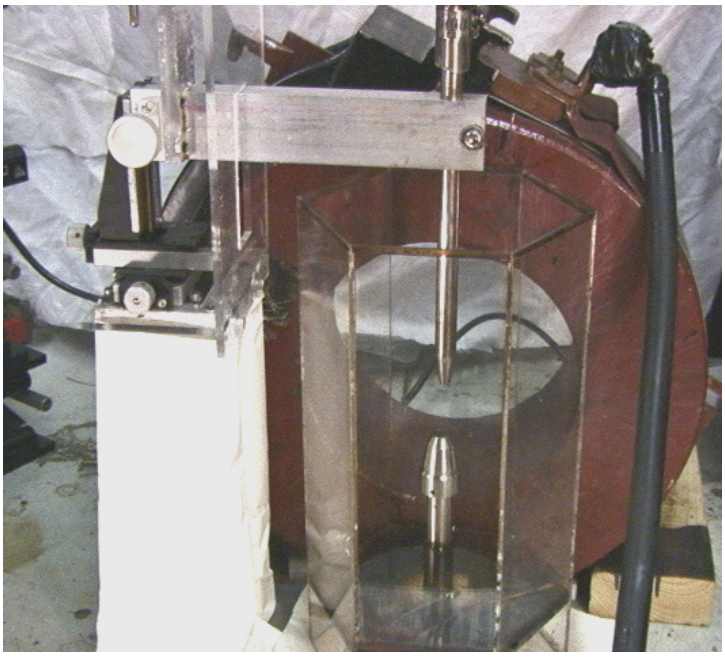

Figure 4.8: The experimental setup for applying a magnetic field tangential to the radial sheet flow and perpendicular to the vertical ferrofluid jet. The test cell containing the flow is placed between two electromagnets (only one is pictured) which generate a magnetic field parallel to the plane of the ferrofluid sheet.

eventually leading to the formation of sharp tips at the end of the major axis at large field strength. In certain instances fluid chains, as described by Bush and Hasha [44], were created at the sheet tips as seen in Figure 4.10. In addition to the noticeable magnification of waves on the sheet, the sheet itself is no longer flat, but instead develops a downward curvature.

Deformation of the Jet

It was observed that the extent of deformation undergone by the sheet increased with the jet length, as defined in Figure 4.1. Evidence of this behavior is seen by comparison of Figure 4.9, with long jet length $l_J = 30$ mm, with Figure 4.11 with short jet length $l_J =$

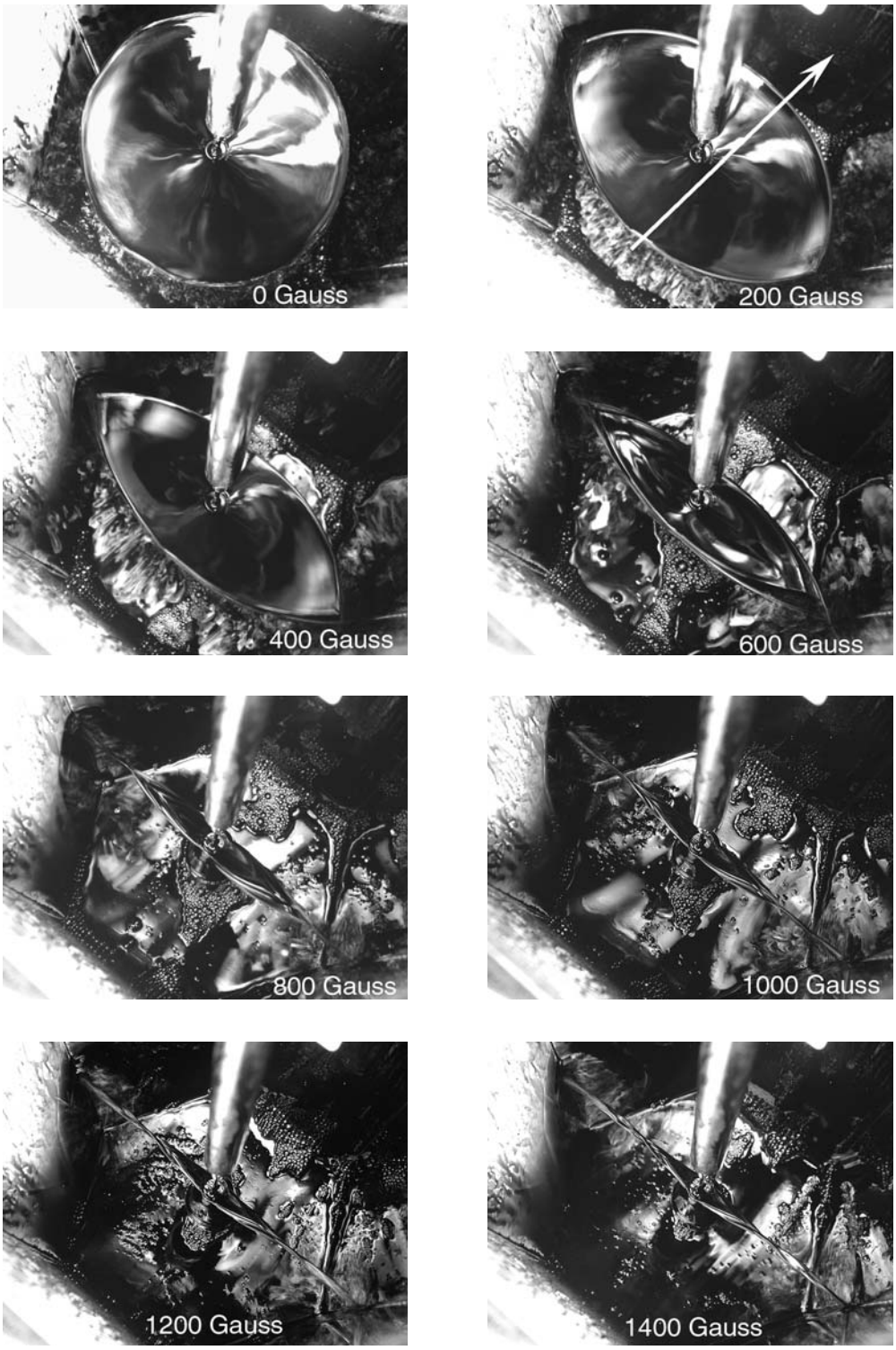

Figure 4.9: Top view of a ferrofluid sheet with a magnetic field applied in plane with the sheet and perpendicular to the incident fluid jet, in the direction indicated by the arrow. The approximate applied magnetic field values are indicated. The jet length, l_j, is 30 mm.

Figure 4.10: A close-up view of a ferrofluid chain at the tip of a lenticular ferrofluid sheet.

6 mm. It is obvious from these photographs that there is considerable deformation of the sheet for the case of the long jet length, while the case of the short jet length shows minimal sheet deformation. This jet-length dependent distortion prompted a detailed investigation of the jet behavior, which revealed that the jet cross-section is distorted from circular by the applied magnetic field. We observed that the cross-section of the jet is elongated in the direction of the applied magnetic field, and so is opposite to that of the corresponding sheet as in Figure 4.12 and illustrated in Figure 4.13.

These observations of jet deformation from a circular to elliptical cross-section are analogous to the theoretical predictions of Shcherbinin in considering an electrically conducting, non-magnetic, liquid jet carrying electrical current and exposed to a uniform magnetic field perpendicular to the direction of flow [45]. Similarly to the elongation of a ferrofluid droplet in a uniform magnetic field, jet elongation in the direction of applied magnetic field perpendicular to axial flow should be described by the Ferrohydrodynamic Bernoulli equation [1].

We have noted experimentally in Figures 4.9 and 4.12 that the jet deforms to a lens-like

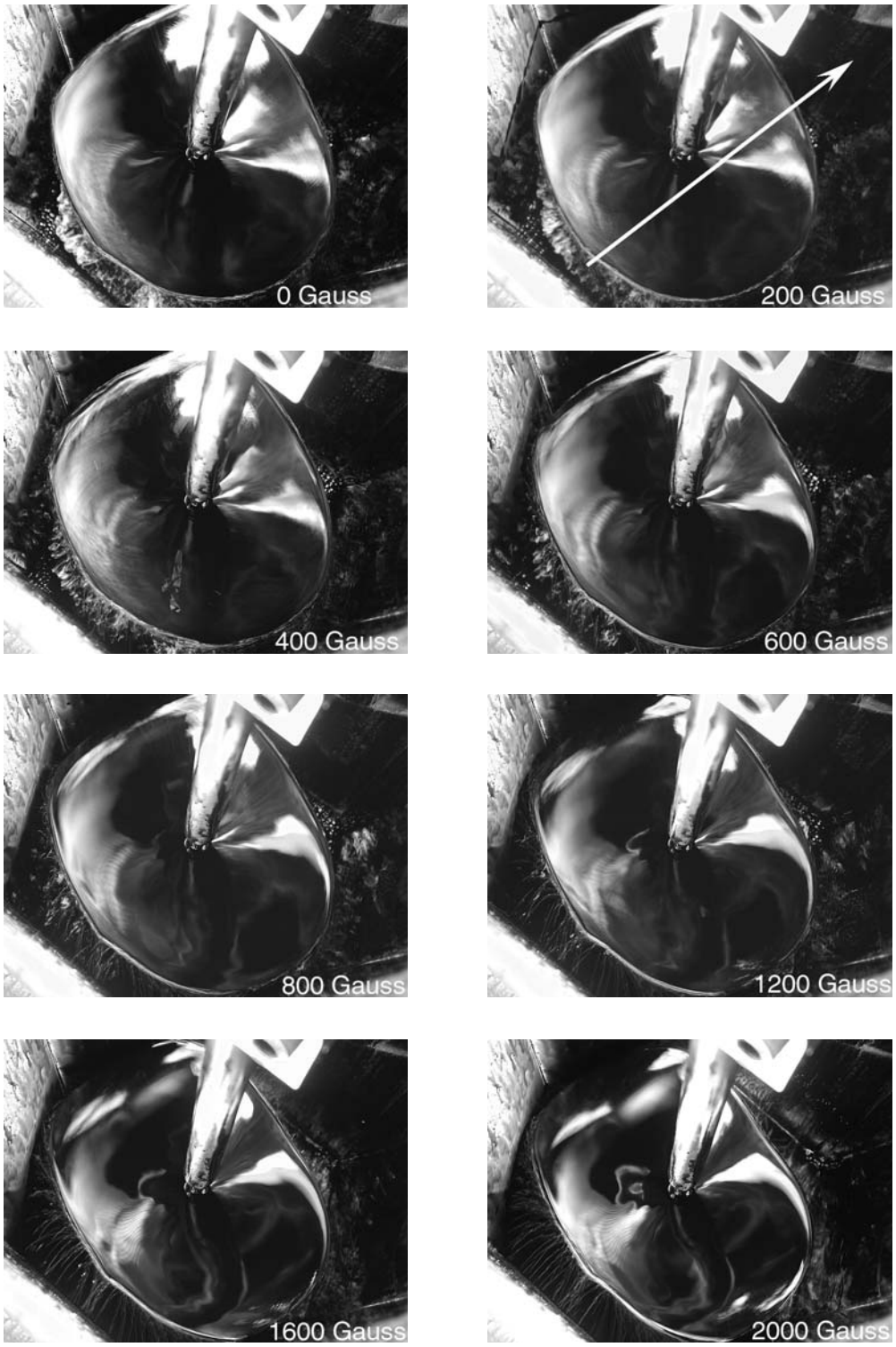

Figure 4.11: A magnetic field is applied in plane with the ferrofluid sheet and perpendicular to the incident fluid jet, in the direction indicated by the arrow. The approximate applied magnetic field values are given for each picture. The ferrofluid jet length, l_j, is 6 mm.

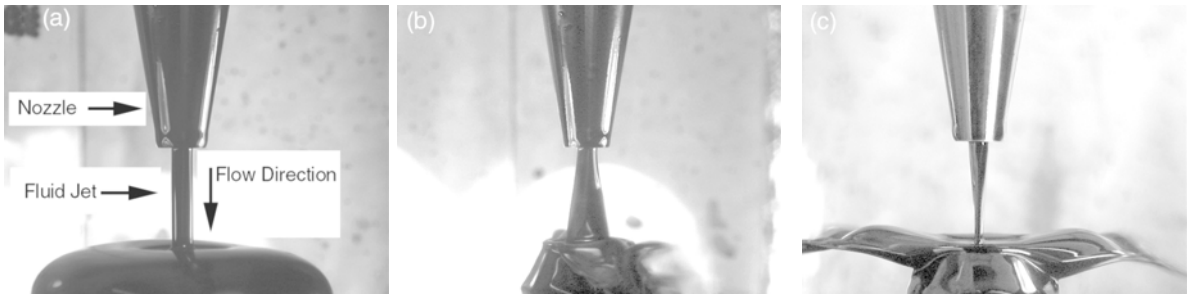

Figure 4.12: A ferrofluid jet of length 12 mm with (a) no magnetic field, (b) a magnetic field applied right to left, and (c) a view at 90^o to (b) so that the magnetic field is directed out of the page.

Figure 4.13: (Left) The cross-section of the ferrofluid jet and sheet are mutually circular in the absence of an applied magnetic field, but (Right) when a magnetic field is applied the long axis of the jet cross-section is parallel to the magnetic field while the long axis of the sheet cross-section is oriented perpendicularly to the magnetic field.

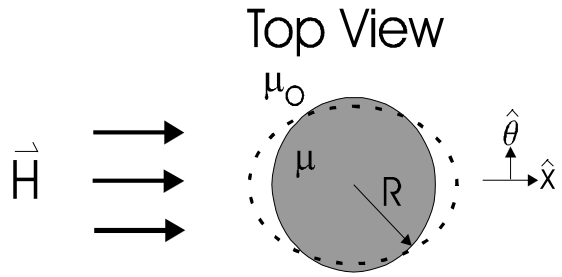

Figure 4.14: A uniform magnetic field applied perpendicularly to the axis of an infinite circular cylinder of ferrofluid (solid circle) of radius R and magnetic permeability μ will elongate the cross-section of the cylinder to an approximately elliptical shape with long axis in the direction of the magnetic field, as illustrated by the dashed line.

shape perpendicularly oriented to a similar shape of the resulting sheet. To theoretically explain these effects, consider the two-dimensional problem of an infinitely long cylinder of ferrofluid of radius R. We apply a uniform x-directed magnetic field at $r = \infty$ as shown in Figure 4.14. In cylindrical coordinates this is represented mathematically by

$$\vec{H}_{applied} = H_o\hat{x} = H_o(\cos\theta\hat{r} - \sin\theta\hat{\theta}) \tag{4.16}$$

where $\vec{H}$ is the magnetic field, and $\hat{r}$ and $\hat{\theta}$ are the radial and θ-directed unit vectors. In the absence of electric currents Ampere's Law in the magnetostatic limit $\left(\frac{\partial\vec{D}}{\partial t} \approx 0\right)$ indicates that the curl of the magnetic field is zero so that the magnetic field can be defined as the negative gradient of a magnetic scalar potential ψ

$$\vec{\nabla} \times \vec{H} = \vec{J} = 0 \Rightarrow \vec{H} = -\vec{\nabla}\,\psi. \tag{4.17}$$

Gauss' Law for magnetic fields and the constitutive relation $\vec{B} = \mu\,\vec{H}$ then give for constant μ

$$\vec{\nabla} \cdot \vec{B} = \vec{\nabla} \cdot (\mu\,\vec{H}) = \mu(\vec{\nabla} \cdot \vec{H}) = 0 \quad \Rightarrow \vec{\nabla} \cdot \vec{H} = 0. \tag{4.18}$$

Since the magnetic permeability within the ferrofluid and the ambient air are assumed to be spatially constant (4.18) requires that the magnetic scalar potential in each region must satisfy Laplace's equation

$$\nabla^2 \psi = 0. \tag{4.19}$$

Laplace's equation can be solved using (4.16) in cylindrical coordinates with the boundary conditions that the field is finite at $r = 0$, the normal (radial) component of $\vec{B}$, B_r, is continuous at the $r = R$ cylinder boundary, and the tangential component of $\vec{H}$, H_θ, is continuous at the $r = R$ cylinder boundary. The magnetic field is then

$$\vec{H} = \begin{cases} \dfrac{2\mu_o H_o}{(\mu + \mu_o)}(\cos\theta\hat{r} - \sin\theta\hat{\theta}) = \dfrac{2\mu_o H_o}{\mu_o + \mu}\hat{x} & r < R \\ H_o \left[\left(1 + \dfrac{R^2(\mu - \mu_o)}{r^2(\mu + \mu_o)} \right) \cos\theta\hat{r} - \left(1 - \dfrac{R^2(\mu - \mu_o)}{r^2(\mu + \mu_o)} \right) \sin\theta\hat{\theta} \right] & r > R \end{cases} \tag{4.20}$$

where μ_o is the magnetic permeability of free space, and r is the radial distance from the center of the cylinder.

The magnetic body force for the system is given by

$$\vec{F} = -\frac{1}{2} H^2 \vec{\nabla} \mu \tag{4.21}$$

which is identically zero within the ferrofluid volume since μ is spatially constant. There is, however, a magnetic surface force at the $r = R$ boundary since the magnetic permeability changes from μ to μ_o. This magnetic surface force can be evaluated using the Maxwell Stress tensor for the force density of (4.21) [33, 46]

$$T_{ij} = \mu H_i H_j - \delta_{ij} \frac{1}{2} \mu H_k H_k. \tag{4.22}$$

Here we have introduced the Einstein index notation where i, j, and k represent the orthogonal axes of the coordinate system and may take on any of the values x, y, z, r, or θ. The

physical meaning of T_{ij} is a force per unit area in the i^{th} direction acting on a surface whose normal is in the j^{th} direction. The Kronecker delta is defined as

$$\delta_{ij} = \begin{cases} 0, & \text{if } i \neq j \\ 1, & \text{if } i = j. \end{cases} \tag{4.23}$$

The shear stress is given by the jump in $T_{\theta r} = \mu H_\theta H_r$ across the $r = R$ interface

$$\begin{aligned} \Delta(T_{\theta r}(r = R)) &= T_{\theta r}(r = R_+) - T_{r\theta}(r = R_-) \\ &= \mu_o H_r(r = R_+) H_\theta(r = R_+) - \mu H_r(r = R_-) H_\theta(r = R_-) = 0. \end{aligned} \tag{4.24}$$

This equation evaluates to zero by applying the boundary conditions of continuous normal $\vec{B}$, $\mu_o H_r(r = R_+) = \mu H_r(r = R_-)$, and continuous tangential $\vec{H}$, $H_\theta(r = R_+) = H_\theta(r = R_-)$. The jump in radial magnetic stress at the ferrofluid/air boundary is

$$\Delta(T_{rr}(r = R)) = T_{rr}(r = R_+) - T_{rr}(r = R_-) \tag{4.25}$$

$$= \frac{\mu_o}{2}\left[H_r^2(r = R_+) - H_\theta^2(r = R_+)\right] - \frac{\mu}{2}\left[H_r^2(r = R_-) - H_\theta^2(r = R_-)\right]. \tag{4.26}$$

Using (4.20) to evaluate (4.26) produces

$$\Delta(T_{rr}(r = R)) = \frac{2\mu_o(\mu - \mu_o)}{(\mu + \mu_o)^2} H_o^2(\mu \cos^2\theta + \mu_o \sin^2\theta). \tag{4.27}$$

Evaluating (4.27) at the angles $\theta = 0, \pi$ and $\theta = \pm\frac{\pi}{2}$ shows that the magnetic stress is greater in the direction of the applied field than perpendicular to this direction

$$\frac{\Delta(T_{rr}(r = R))|_{\theta=0,\pi}}{\Delta(T_{rr}(r = R)|_{\theta=\pm\frac{\pi}{2}}} = \frac{\mu}{\mu_o}. \tag{4.28}$$

The larger stress acts to force fluid outward at $\theta = 0$ and π, in effect elongating the cross-section of the jet parallel to the applied field, as seen experimentally in Figure 4.12.

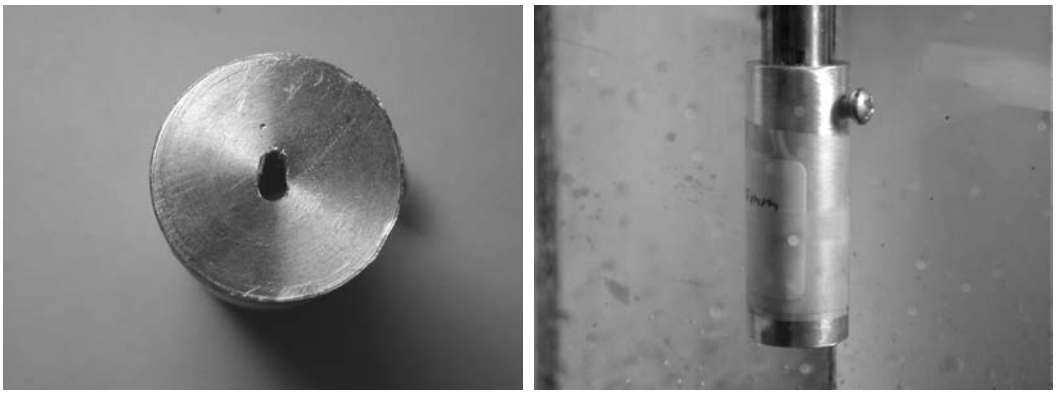

Figure 4.15: (Left) Photograph of the nozzle adapter with elliptical orifice of aspect ratio 3.3:2.0 used for making jets with an elliptical cross-section. (Right) The elliptical nozzle adapter attached to the circular nozzle.

The analysis just presented is only applicable to a jet of circular cross-section, since as soon as the jet deforms from circular the magnetic fields of (4.20) no longer hold. However, from the analysis we gain an intuitive feel for the behavior, indicating that the jet should continue to elongate in the direction of the applied magnetic field, even after deformed from its initially circular cross-section.

4.2.2 Flip-flop of the Jet and Sheet

Considering the observations in section 4.2.1 lead to the hypothesis that the dominant magnetic effect is on changing the cross-section of the incident jet, which in turn determines the shape of the resulting sheet.

To test this hypothesis, several nozzles of approximately elliptical cross-section were fashioned so as to be placed over the nozzle of circular cross section used up to this point. The nozzle shown in Figure 4.15 has an aspect ratio of 3.3:2.0.

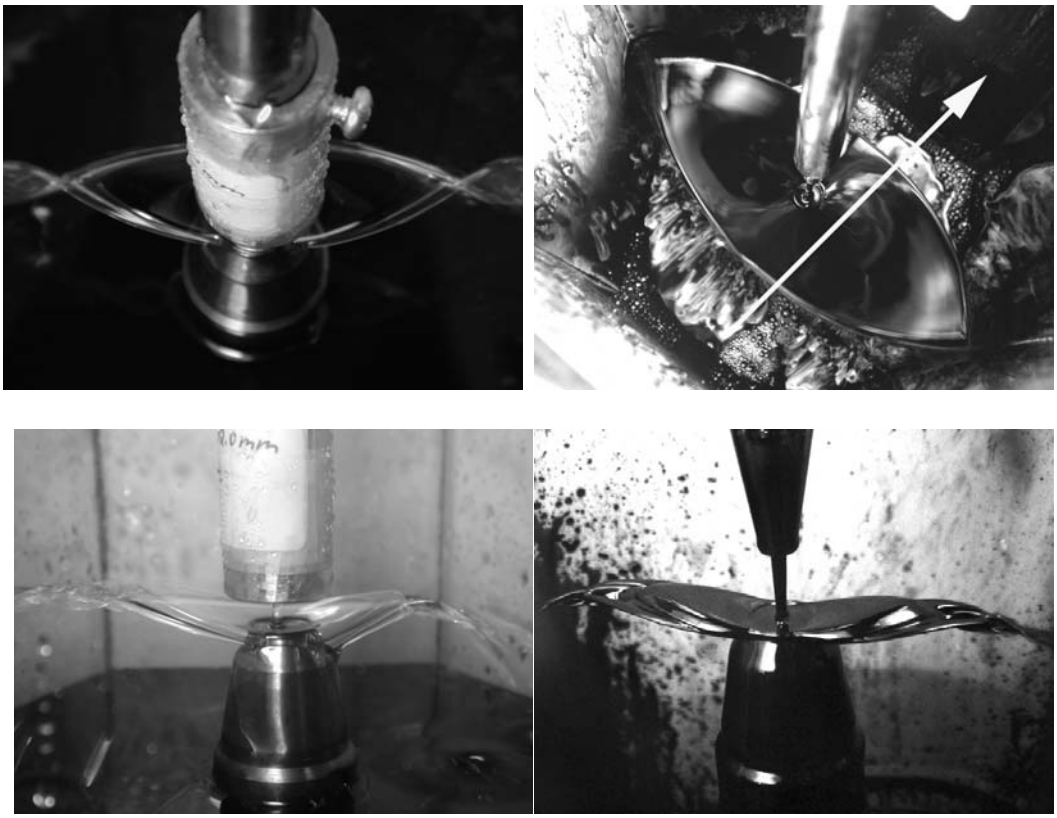

Figure 4.16: (Top Left) A lens-shaped fluid sheet created with glycerol/water and an elliptical nozzle with its cross-section long axis oriented from top to bottom in the plane of the picture as viewed from above (perpendicular to sheet long axis) and (Top Right) similar to a ferrofluid sheet created with a circular nozzle and a magnetic field applied in the direction of the arrow. (Bottom Left) A side view of the glycerol/water sheet with the long axis of the elliptical nozzle oriented into and out of the page and (Bottom Right) a side view of the analogous ferrofluid sheet.

Using this nozzle adapter, laminar jets of non-magnetic liquid and elliptical cross-section were investigated in the absence of magnetic fields. A non-magnetic glycerol/water solution of approximate ratio 9:1 by volume was used. The sheets formed in these cases were again lens-like and oriented with long axis perpendicular to the long axis of the nozzle as shown in Figure 4.16, in agreement with the stated hypothesis. It is noteworthy that there were minor

differences between the magnetic and non-magnetic flows, specifically in the appearance of surface waves and patterns. These differences could be due to any of the differences between the experiments such as the fluid viscosities, flow rates, take-off angle, and the presence of the magnetic field in the case of the ferrofluid flows.

To qualitatively explain the physical mechanism governing the flip-flop at the point of impact we begin with previously understood phenomena. In particular, the cross-section of a jet issuing from an elliptical orifice is known to oscillate along the length of the jet [47, pp. 355-60]. Several forces may be acting on the jet depending on the details of the configuration. These forces include inertia, viscosity, gravity, and surface tension. In the case of a vertical jet in a gravitational field the jet will accelerate downward, with conservation of mass requiring a decrease in the area of the jet cross-section. This phenomena need not be considered in explaining the oscillation of the cross-section [47]. Viscosity will act to damp the oscillations but again is not important in describing the source of the oscillation. Thus, only surface tension and inertia need be considered in describing the simple oscillation mentioned.

As the jet emerges from the elliptical orifice its free surface is dominated by surface tension, which acts to deform the elliptical cross-section to a circular form. However, in the process there is a radial velocity induced within the jet which proceeds to force the cross-section beyond the circular form into an ellipse oriented perpendicular to that of the original. The process will repeat until the oscillations are damped [48]. Figure 4.17 provides a visual depiction of the oscillation process. The important concept is that where the radial velocity goes to zero, surface tension acts to direct the cross-section toward a circular shape, but an overshoot will lead to a cross-section orientation opposite that from which it was

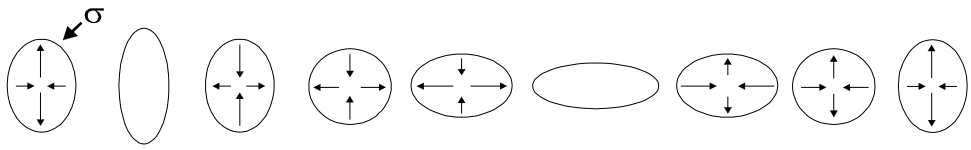

Figure 4.17: The cross-section of an oscillating elliptical jet governed by surface tension, σ, and inertia. The arrows indicate the changing direction of the radial flow over the course of a single oscillation cycle.

immediately before the velocity went to zero.

The flip-flop of the jet and sheet at the impactor can be explained by similar reasoning. At the impactor a no-slip boundary condition must be applied to all components of the velocity, i.e. the radial velocity is forced to zero. The radial inertial force of the jet is then zero and surface tension acts alone. As in Figure 4.17, when surface tension is the lone force, the jet will proceed toward a circular cross-section, and in so doing will overshoot the targeted circular shape and arrive at a cross-section orientation that is perpendicular to the orientation immediately before jet impact.

In addition to working with dc magnetic fields, ac magnetic fields were also applied in the setup discussed. At low field oscillation frequencies (1 Hertz) the forms assumed by the sheet and jet appeared no different than those of the dc case described, yet the entire progression from circular to elliptical and back to circular could be observed within a short time. At higher field frequencies (60 Hertz) the fluid could not respond to the dynamics of the applied field, but rather would respond to the root mean square (rms) magnetic field

and therefore would assume a single form identical to that with dc magnetic fields.

We note that the jet and sheet forms presented thus far are independent of the magnetic field polarity since the magnetic force on ferrofluids is proportional to the square of the field.

4.2.3 Elliptical Hydraulic Jumps

The well-known phenomenon of a hydraulic jump occurs when a fluid flow is forced to abruptly slow its speed, leading to an abrupt increase in depth of the flow. For exploratory purposes we created a circular hydraulic jump using a laminar cylindrical liquid jet impacting a large basin. The liquid was a non-magnetic glycerol/tap water mixture. An elliptical nozzle, similar to that shown in Figure 4.15, was then used to create a laminar jet of elliptical cross-section, which upon impact with the basin created an elliptical hydraulic jump that had its long axis oriented perpendicularly to the long axis of the incident jet. This is another display of the flip-flop behavior described for the liquid sheet configuration. These results imply that the flip-flop behavior is not confined to the sheet experiments detailed in this thesis, but is likely present in various fluid systems involving impact of an elliptical jet on a surface. The flip-flop behavior might also be found in the impact of malleable solid materials of elliptical shape.

4.2.4 Experiment 2: The Kelvin-Helmholtz Instability

A dc magnetic field is applied parallel to the incident jet axis, and thus perpendicular to the sheet flow as seen in Figure 4.18. The setup consists of placing the container housing the flow inside a single electromagnet from the previous experiment. The photographs in Figure 4.19 show that as the magnetic field is increased the sheet decreases in radius with a noticeable

Figure 4.18: The test cell is placed inside the vertical magnetic field created by the electromagnetic. The ferrofluid jet is aligned with the magnetic field while the resulting radial sheet flow is perpendicular to the magnetic field.

roughening of the surface and edge. The shape of the sheet remains approximately circular. It is also noteworthy that the decrease in sheet radius is not initiated until a critical magnetic field strength is applied, as the data indicate in Figure 4.20.

The dominant physical mechanism of the sheet breakup is the enhancement of the unstable anti-symmetric surface waves (flapping regime) caused by application of the magnetic field, as will be demonstrated by analysis of the ferrohydrodynamic Kelvin-Helmholtz theory. Interestingly, the magnetic field induced instability under consideration is the convective analog to the well known peaking instability exhibited by a stationary ferrofluid layer exposed to a magnetic field normal to the fluid/air interface [1] as shown in Figure 4.21.

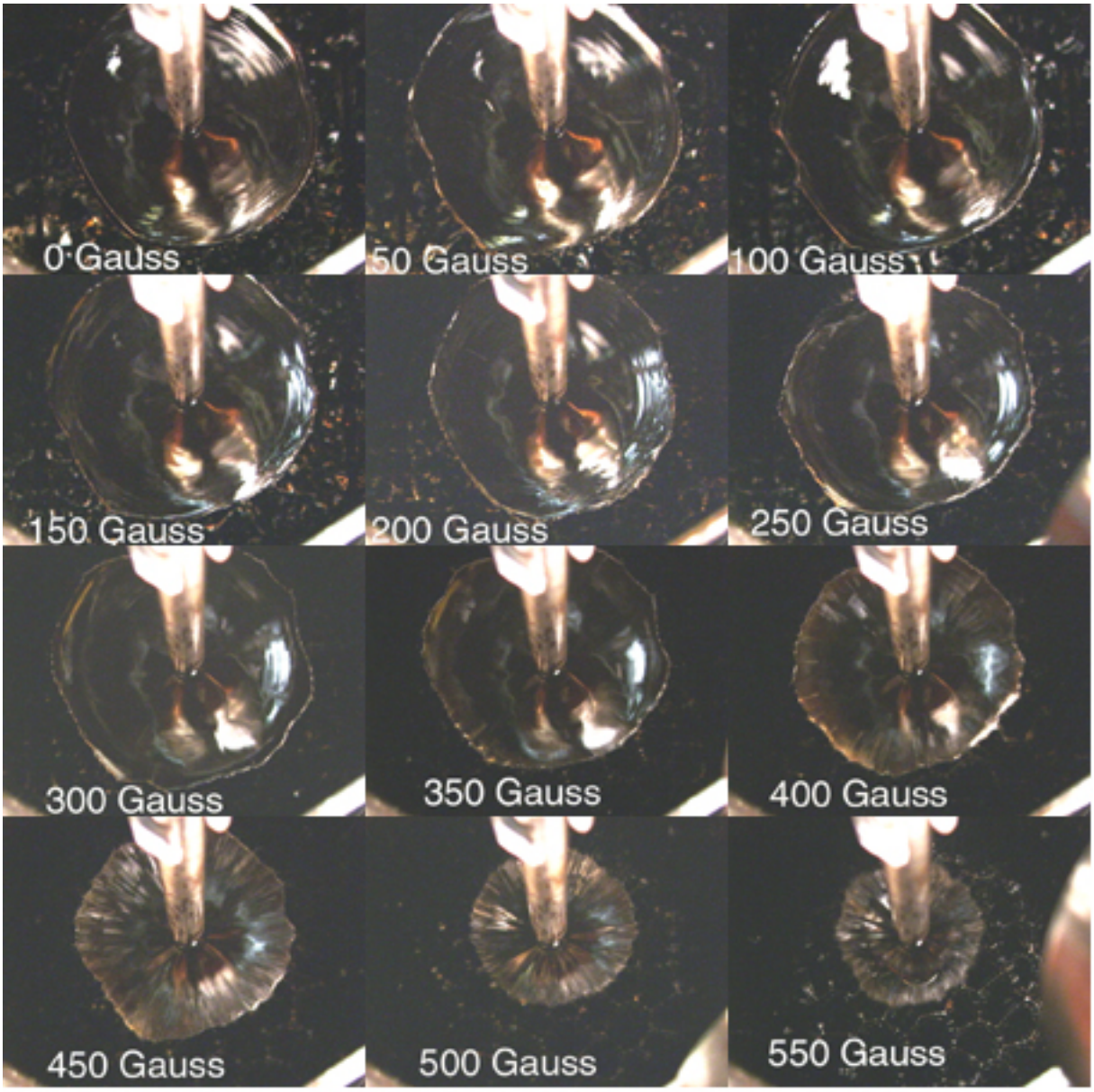

Figure 4.19: Top view of an EFH1 ferrofluid sheet in the presence of a magnetic field applied out of the page. The approximate magnetic field values are listed in each frame. In the last frame the formation of hexagonal peaks, similar to Figure 4.21, can be seen behind the sheet.

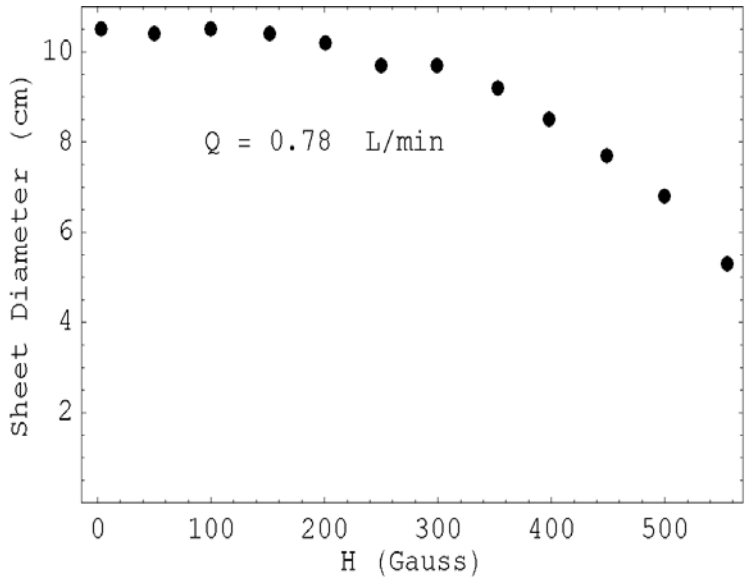

Figure 4.20: The measured diameter of an EFH1 hydrocarbon-based ferrofluid sheet exposed to a perpendicular magnetic field decreases with increasing magnetic field strength above a threshold magnetic field value of approximately 200 Gauss. These data points correspond to a series of photographs similar to those shown in Figure 4.19.

Figure 4.21: The Kelvin-Helmholtz instability becomes the Rayleigh-Taylor instability for an initially flat, stationary ferrofluid layer that assumes the shown hexagonal array of peaks. The magnetic field is applied normal to the fluid interface, or equivalently out of the page.

Bernoulli Analysis of the Sheet in a Perpendicular Magnetic Field

Referring to Figure 4.5 we may apply a Bernoulli analysis to our system, taking into account the magnetic surface stresses due to the applied spatially uniform perpendicular magnetic field, $\vec{B}= B_z\hat{z}$. There is no magnetic body force to consider as seen from (4.21). At point a we write the pressure as

$$p_a - p_o = T_{xxa} - T_{xxo} \tag{4.29}$$

in which T_{xxa} and T_{xxo} are the magnetic stress tensor components at point a, and just above the sheet surface, respectively. The magnetic stress tensor components are given in (4.22). After explicitly writing the tensor components (4.29) becomes

$$p_a = p_o + \frac{1}{2}B_z^2\left(\frac{1}{\mu} - \frac{1}{\mu_o}\right) \tag{4.30}$$

where we have used the fact that the normal magnetic field component, B_z, is continuous across the interface. The pressure at point b, p_b, is given by (4.12)

$$p_b = p_o + \sigma\left(\frac{1}{r_1} + \frac{1}{r_2}\right) \tag{4.31}$$

in which we have assumed that the jump in magnetic stress across the sheet/air interface at point b is negligibly small. Since $r_2 = r_{max} \gg r_1$ we ignore the r_2 term. At this point we assume that $r_1 = \alpha h$, where α is a constant multiplier. In the Bernoulli analysis of section 4.1.1 we set $\alpha = 1$. However, in reality the sheet edge is bounded by a cylindrical rim which may have a radius much greater than, or less than, the sheet thickness [44]. By allowing α to remain an unknown we may later adjust its value to match our experimental data. The pressure of (4.31) is then given by

$$p_b = p_o + \frac{\sigma}{\alpha h}. \tag{4.32}$$

Relating the pressure at the points a and b with Bernoulli's equation, (3.6), produces

$$p_a + \frac{1}{2}\rho U_a^2 + z_a = p_b + \frac{1}{2}\rho U_b^2 + z_b. \tag{4.33}$$

Since $z_a = z_b$ these gravity terms again drop out of the equation. Additionally, as explained in section 4.1.1 we assume that $U_b \approx 0$ and define $U_a = U$. Substituting in the pressures p_a from (4.30) and p_b from (4.32), leads to the relation

$$\frac{1}{2}B_z^2\left(\frac{1}{\mu} - \frac{1}{\mu_o}\right) + \frac{1}{2}\rho U^2 = \frac{\sigma}{\alpha h}. \tag{4.34}$$

Substituting (4.5) for h and rearranging terms leads to a formulation of the sheet radius as a function of magnetic field

$$r = \frac{\alpha Q}{2\pi U\sigma}\left[\frac{1}{2}\rho U^2 - \frac{B_z^2}{2\mu\mu_o}(\mu - \mu_o)\right] = r_T\left[1 - \frac{B_Z^2}{\rho U^2\mu\mu_o}(\mu - \mu_o)\right]. \tag{4.35}$$

If $B_z = 0$ we get back the result of (4.8) and (4.15). Otherwise, since the term involving B_z is always negative the magnetic field will serve to decrease the sheet radius, as is seen experimentally in Figure 4.19. The experimental sheet diameter is plotted with the theory of (4.35) in Figure 4.22. Note that in this plot, to match the first experimental data point with the theoretical value when $B_z = 0$, we set $\alpha = 0.43$. If $\alpha = 0.5$ this would imply that the radius of curvature at the sheet edge is half the sheet thickness at the edge, or equivalently $r_1 = \frac{1}{2}h$. Without this adjustment the theoretical value for $B_z = 0$ would be approximately twice the experimental value. The adjustment causes no change in the slope of the theoretical line.

From Figure 4.22 we see that the sheet diameter, derived from Bernoulli law considerations, does not accurately predict the magnetic field dependence of the experimental data. In particular, the initial value of the sheet radius ($H = 0$), and the slope of the theoretical

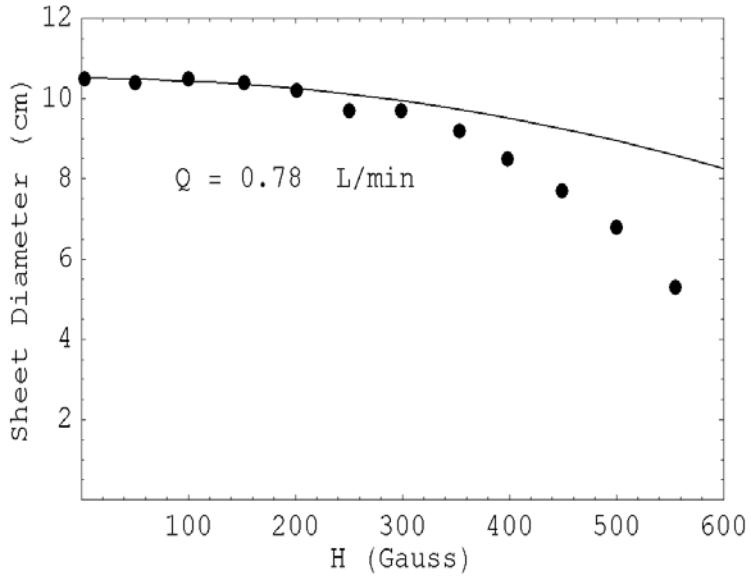

Figure 4.22: The measured diameter (dots) of an EFH1 hydrocarbon-based ferrofluid sheet exposed to a perpendicular magnetic field decreases with increasing magnetic field strength above a threshold magnetic field value of approximately 200 Gauss. These data points are also shown in Figure 4.20. The theoretical diameter (solid line) of Eq. (4.35) is plotted as well. Note that the theoretical line has been adjusted to match the first experimental data point (r_T), and otherwise would have a value approximately twice as large as the experimental data for $H = 0$.

curve are inadequate. The most likely reason for this is that until now we have assumed the only effect of the magnetic field is to add a stress at the upper and lower interfaces. This would indeed be the case if the sheet remained in the smooth regime while the magnetic field is applied. However, the photographic evidence of Figure 4.19 indicates that the sheet surface becomes significantly rougher upon application of the magnetic field. The analysis that follows considers the effect of the applied magnetic field on the sheet surface waves, indicating that the sheet transitions from the smooth regime to the flapping regime when the magnetic field is applied and the flow rate is held constant.

In this section we have introduced the parameter α to describe the sheet rim radius. Future work should thoroughly investigate the effect of the magnetic field on the rim dynamics.

4.2.5 Magnetic Field Effects on the Kelvin-Helmholtz Instability

Governing Equations

We intend to derive the dispersion relation describing the magnetic field effect on the wavelength of instability for the surface waves on the ferrofluid sheet. The general class of problems involving magnetic forces on a single fluid interface has been treated by Melcher [49, p. 80]. We extend the analysis to a fluid with both an upper and lower interface.

We begin by modeling the general ferrohydrodynamic problem shown in Figure 4.23 of a two-dimensional planar configuration of a sheet of fluid with mass density ρ, magnetic permeability μ, and pressure p moving at relative velocity U through an ambient fluid of mass density ρ_o, magnetic permeability μ_o, and pressure p_o. Note that the geometry is now posed in Cartesian coordinates whereas the Bernoulli discussion of Figure 4.5 was posed in cylindrical coordinates. Furthermore the current discussion will consider variations only in the x and z directions, with no variation in the y-direction. The effects of gravity are neglected due to a large Froude number. Surface tension, σ, is present at both the upper and lower interfaces and it is assumed that a uniform x-directed magnetic flux density, $\vec{B}= B_o\hat{x}$, and a uniform tangential magnetic field, $\vec{H}= H_o\hat{z}$, are applied. The fluids are assumed inviscid. We proceed with a linear stability analysis of the system assuming that the interfacial deflections ξ_1 and ξ_2 are small, allowing neglect of terms of second and higher order in these parameters. The Navier-Stokes equations for incompressible and inviscid flow

are

$$\rho\left[\frac{\partial\,\vec{v}}{\partial t}+(\vec{v}\cdot\vec{\nabla})\,\vec{v}\right]=-\,\vec{\nabla}\,p,\quad \vec{\nabla}\cdot\vec{v}=0 \tag{4.36}$$

where p is the fluid pressure, and $\vec{v}$ is the fluid velocity. There is no magnetic force density since the magnetic permeability is constant within the fluid.

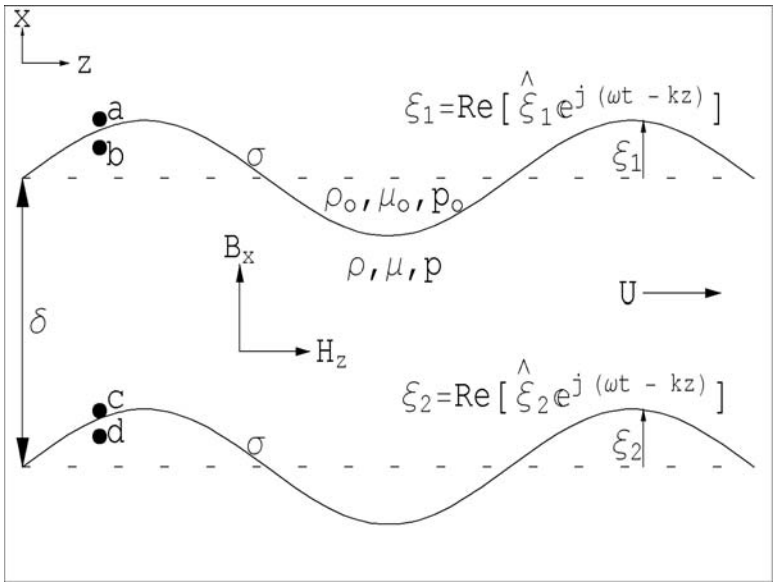

Figure 4.23: The two-dimensional Kelvin-Helmholtz configuration of a ferrofluid layer moving through an ambient fluid at velocity U with an imposed spatially uniform magnetic field with components perpendicular and tangential to the free interfaces. The interfacial displacements are ξ_1 and ξ_2.

Equilibrium ($\xi_1 = \xi_2 = 0$)

We begin by examining the conditions required to make the state $\xi_1 = \xi_2 = 0$ an equilibrium state. In the absence of viscous and magnetic body forces, the dynamics of the upper and lower interfaces are described by a balance of pressure, surface tension, and magnetic surface stresses, T_{ij}. For the case when $\xi_1 = \xi_2 = 0$ we can find the equilibrium pressure at points a,

b, c, and d, which are located just above and below the upper and lower interfaces. Realizing that surface tension has no effect on a flat interface the equilibrium force balance is

$$P_b - P_a + T_{xxa} - T_{xxb} = 0 \tag{4.37}$$

$$P_d - P_c + T_{xxc} - T_{xxd} = 0. \tag{4.38}$$

Applying (4.22) at each interface the magnetic surface stress on a material with magnetic permeability μ_m is

$$T_{xx} = \frac{\mu_m}{2}\left(H_x^2 - H_z^2\right) \tag{4.39}$$

where $\mu_m = \mu_o$ at the points a and d in air, and $\mu_m = \mu$ at the points b and c in the ferrofluid. The jump in magnetic stress at the upper and lower interfaces is then given by

$$\begin{aligned} T_{xxa} - T_{xxb} &= \frac{\mu_o}{2}\left[\left(\frac{B_x}{\mu_o}\right)^2 - H_z^2\right] - \frac{\mu}{2}\left[\left(\frac{B_x}{\mu}\right)^2 - H_z^2\right] \\ &= \frac{B_x^2}{2}\left(\frac{1}{\mu_o} - \frac{1}{\mu}\right) + \frac{H_z^2}{2}(\mu - \mu_o) \qquad (4.40) \\ T_{xxc} - T_{xxd} &= -\left(T_{xxa} - T_{xxb}\right) \qquad (4.41) \end{aligned}$$

for which we have used the fact that B_x and H_z are continuous across each interface. The equilibrium pressures in (4.37) and (4.38) can then be written in terms of the equilibrium magnetic fields using $P_a = P_d = P_o$ as atmospheric pressure

$$P_b = P_c = P_o - \frac{B_x^2}{2}\left(\frac{1}{\mu_o} - \frac{1}{\mu}\right) - \frac{H_z^2}{2}(\mu - \mu_o). \tag{4.42}$$

Thus, $\xi_1 = \xi_2 = 0$ is an equilibrium state with uniform equilibrium pressure. Recognize that since $\mu > \mu_o$ both B_x and H_z tend to lower the pressure within the fluid.

Linear Analysis of Interfacial Perturbations

Now that the equilibrium conditions are established the system dynamics are examined for a small displacement from equilibrium (non-zero ξ_1 and ξ_2), in the presence of spatially uniform magnetic fields. In this situation the fluid and magnetic quantities take on perturbation terms, written as

$$\vec{H} = \left(\frac{B_x}{\mu_m} + h_x\right)\hat{x} + (H_z + h_z)\,\hat{z} \tag{4.43}$$

$$\vec{v}_T = U\hat{z} + \vec{v} = U\hat{z} + v_x\hat{x} + v_z\hat{z} \tag{4.44}$$

$$p_T = P + p \tag{4.45}$$

where uppercase letters imply equilibrium terms and lowercase letters imply perturbation terms on the right hand side of the above equations. The quantities $\vec{v}_T$ and p_T are the total fluid velocity and pressure, respectively. The perturbation velocities at the upper and lower interfaces are directly related to the interfacial deflections by

$$v_{x1} = \frac{\partial \xi_1}{\partial t} + U\frac{\partial \xi_1}{\partial z} \tag{4.46}$$

$$v_{x2} = \frac{\partial \xi_2}{\partial t} + U\frac{\partial \xi_2}{\partial z}. \tag{4.47}$$

We assume interfacial deflections of the form $\xi_1 = \mathrm{Re}[\tilde{\xi_1}e^{j(\omega t - kz)}]$ and $\xi_2 = \mathrm{Re}[\tilde{\xi_2}e^{j(\omega t - kz)}]$ so that all perturbations of the system are of the form $\exp j(\omega t - kz)$, where $j = \sqrt{-1}$, $\omega = 2\pi f$ is the radian frequency of oscillation corresponding to the frequency f, and $k = \frac{2\pi}{\lambda}$ is the wavenumber corresponding to the spatial wavelength λ. The adopted form for the perturbations allows (4.46) and (4.47) to be written in terms of complex amplitudes (designated by a '~') as

$$\tilde{v}_{x1} = j(\omega - kU)\tilde{\xi_1} \tag{4.48}$$

$$\tilde{v}_{x2} = j(\omega - kU)\tilde{\xi}_2. \tag{4.49}$$

Since the magnetoquasistatic magnetic field is curl-free in the absence of electrical currents, the perturbation magnetic field, $\vec{h}$, is defined as the negative gradient of a perturbation magnetic scalar potential, ψ, satisfying Laplace's equation

$$\vec{h} = -\vec{\nabla}\,\psi \tag{4.50}$$

$$\vec{\nabla} \cdot \vec{h} = 0 \tag{4.51}$$

$$\Rightarrow \nabla^2\psi = 0. \tag{4.52}$$

The magnetic field perturbations at each interface can then be related to the scalar potential at each interface through the transfer relation [33]

$$\begin{pmatrix} \tilde{h}_{xb} \\ \tilde{h}_{xc} \end{pmatrix} = k \begin{pmatrix} -\coth k\delta & \frac{1}{\sinh k\delta} \\ \frac{-1}{\sinh k\delta} & \coth k\delta \end{pmatrix} \begin{pmatrix} \tilde{\psi}_b \\ \tilde{\psi}_c \end{pmatrix} \tag{4.53}$$

where δ is the equilibrium layer thickness separating the upper and lower interfaces. A similar relationship holds at the points a and d, in the limit where $\delta \to \infty$. This limit gives

$$\tilde{h}_{xa} = k\tilde{\psi}_a \tag{4.54}$$

$$\tilde{h}_{xd} = -k\tilde{\psi}_d \tag{4.55}$$

where, without loss of generality, we take k to be positive. The linearized form of (4.36) in the ferrofluid is

$$\rho\frac{\partial\,\vec{v}}{\partial t} + U\frac{\partial\,\vec{v}}{\partial z} = -\vec{\nabla}\,p. \tag{4.56}$$

Taking the divergence of this equation indicates that the perturbation pressure also satisfies Laplace's equation

$$\nabla^2 p = 0. \tag{4.57}$$

Using (4.57) we similarly find that the pressure and velocity at the interfaces are related by the transfer relation [33]

$$\begin{pmatrix} \tilde{p}_b \\ \tilde{p}_c \end{pmatrix} = \frac{j(\omega - kU)\rho}{k} \begin{pmatrix} -\coth k\delta & \frac{1}{\sinh k\delta} \\ \frac{-1}{\sinh k\delta} & \coth k\delta \end{pmatrix} \begin{pmatrix} \tilde{v}_{xb} \\ \tilde{v}_{xc} \end{pmatrix}. \tag{4.58}$$

At this point we have related the perturbation magnetic field to the perturbation magnetic scalar potential, and the perturbation pressure to the perturbation velocity. Boundary conditions are used to relate these quantities to the interfacial perturbation deflections, ξ_1 and ξ_2.

Magnetic Boundary Conditions

The perturbation surface normals for the upper and lower boundaries, respectively, to first order are

$$\vec{n}_1 = \hat{x} - \frac{\partial \xi_1}{\partial z}\hat{z} \tag{4.59}$$

$$\vec{n}_2 = \hat{x} - \frac{\partial \xi_2}{\partial z}\hat{z}. \tag{4.60}$$

Applying the magnetic boundary condition requiring a continuous normal component of $\vec{B}$ at the upper surface gives to first order

$$\vec{n}_1 \cdot \left[\vec{B}_a - \vec{B}_b\right] = 0 = (\hat{x} - \frac{\partial \xi_1}{\partial z}\hat{z}) \cdot [(\mu_o h_{xa} - \mu h_{xb})\hat{x} + ((\mu_o - \mu)H_z\hat{z}]$$
$$\Rightarrow \mu_o \tilde{h}_{xa} - \mu \tilde{h}_{xb} + jk\tilde{\xi}_1(\mu_o - \mu)H_z = 0. \tag{4.61}$$

Similarly, for the lower interface

$$\vec{n}_2 \cdot \left[\vec{B}_c - \vec{B}_d\right] = 0 = (\hat{x} - \frac{\partial \xi_2}{\partial z}\hat{z}) \cdot [(\mu_o h_{xc} - \mu h_{xd})\hat{x} + ((\mu - \mu_o)H_z\hat{z}]$$
$$\Rightarrow \mu \tilde{h}_{xc} - \mu_o \tilde{h}_{xd} + jk\tilde{\xi}_2(\mu - \mu_o)H_z = 0. \tag{4.62}$$

The boundary condition of continuous tangential $\vec{H}$ at the upper boundary requires, to first order

$$\begin{aligned}
\vec{n}_1 \times \left[\vec{H}_a - \vec{H}_b \right] &= 0 \\
&= \left(\hat{x} - \frac{\partial \xi_1}{\partial z} \hat{z} \right) \times \left[\left(\frac{1}{\mu_o} - \frac{1}{\mu} \right) B_x + h_{xa} - h_{xb} \right] \hat{x} + (h_{za} - h_{zb}) \hat{z} \\
&\Rightarrow \left(\tilde{h}_{za} - \tilde{h}_{zb} \right) - jk\tilde{\xi}_1 B_x \left(\frac{1}{\mu_o} - \frac{1}{\mu} \right) = 0 \qquad (4.63)
\end{aligned}$$

and similarly for the lower boundary is

$$\begin{aligned}
\vec{n}_2 \times \left[\vec{H}_c - \vec{H}_d \right] &= 0 \\
&= \left(\hat{x} - \frac{\partial \xi_2}{\partial z} \hat{z} \right) \times \left[\left(\frac{1}{\mu} - \frac{1}{\mu_o} \right) B_x + h_{xc} - h_{xd} \right] \hat{x} + (h_{zc} - h_{zd}) \hat{z} \\
&\Rightarrow \left(\tilde{h}_{zc} - \tilde{h}_{zd} \right) - jk\tilde{\xi}_2 B_x \left(\frac{1}{\mu} - \frac{1}{\mu_o} \right) = 0. \qquad (4.64)
\end{aligned}$$

The perturbation magnetic field components are related to the scalar potentials at the boundaries using (4.53)

$$\begin{aligned}
\tilde{h}_{xa} &= k\tilde{\psi}_a & (4.65) \\
\tilde{h}_{xb} &= k \left[-\coth k\delta \tilde{\psi}_b + \frac{\tilde{\psi}_c}{\sinh k\delta} \right] & (4.66) \\
\tilde{h}_{xc} &= k \left[-\frac{\tilde{\psi}_b}{\sinh k\delta} + \coth k\delta \tilde{\psi}_c \right] & (4.67) \\
\tilde{h}_{xd} &= -k\tilde{\psi}_d & (4.68) \\
\tilde{h}_{za} &= jk\tilde{\psi}_a & (4.69) \\
\tilde{h}_{zb} &= jk\tilde{\psi}_b & (4.70) \\
\tilde{h}_{zc} &= jk\tilde{\psi}_c & (4.71) \\
\tilde{h}_{zd} &= jk\tilde{\psi}_d. & (4.72)
\end{aligned}$$

Combining (4.65)-(4.72) with (4.61)-(4.64) leads to a system of four equations in the four unknowns $\tilde{\psi}_a$, $\tilde{\psi}_b$, $\tilde{\psi}_c$, and $\tilde{\psi}_d$

$$\begin{aligned}
\tilde{h}_{za} - \tilde{h}_{zb} - jk\tilde{\xi}_1 B_x \left(\frac{1}{\mu_o} - \frac{1}{\mu}\right) &= 0 \Rightarrow \tilde{\psi}_a - \tilde{\psi}_b = B_x \left(\frac{1}{\mu_o} - \frac{1}{\mu}\right)\tilde{\xi}_1 && (4.73)\\
\mu_o\tilde{h}_{xa} - \mu\tilde{h}_{xb} + jk\tilde{\xi}_1(\mu_o - \mu)H_z &= 0 \Rightarrow \mu_o\tilde{\psi}_a - \mu\left(-\coth k\delta\tilde{\psi}_b + \frac{\tilde{\psi}_c}{\sinh k\delta}\right) \\
&= jH_z(\mu - \mu_o)\tilde{\xi}_1 && (4.74)\\
\tilde{h}_{zc} - \tilde{h}_{zd} - jk\tilde{\xi}_2 B_x \left(\frac{1}{\mu} - \frac{1}{\mu_o}\right) &= 0 \Rightarrow \tilde{\psi}_c - \tilde{\psi}_d = B_x \left(\frac{1}{\mu} - \frac{1}{\mu_o}\right)\tilde{\xi}_2 && (4.75)\\
\mu\tilde{h}_{xc} - \mu_o\tilde{h}_{xd} + jk\tilde{\xi}_2(\mu - \mu_o)H_z &= 0 \Rightarrow \mu_o\tilde{\psi}_d - \mu\left(\coth k\delta\tilde{\psi}_d - \frac{\tilde{\psi}_b}{\sinh k\delta}\right) \\
&= -jH_z(\mu - \mu_o)\tilde{\xi}_2. && (4.76)
\end{aligned}$$

Solving the system we obtain the magnetic scalar potentials, $\tilde{\psi}$, as a function of the interfacial deflections, $\tilde{\xi}$, at the points a, b, c, and d

$$\tilde{\psi}_a = \frac{\frac{(\mu - \mu_o)}{\sinh k\delta}\left[(-B_x - jH_z\mu)\mu_o\tilde{\xi}_2 + (B_x + jH_z\mu)\mu_o\tilde{\xi}_1\cosh k\delta + (B_x\mu + jH_z\mu_o^2)\tilde{\xi}_1\sinh k\delta\right]}{\mu_o(\mu^2 + \mu_o^2 + 2\mu\mu_o\coth k\delta)} \tag{4.77}$$

$$\tilde{\psi}_b = -\frac{(\mu - \mu_o)\left[(B_x - jH_z\mu)\mu_o\tilde{\xi}_1 + \mu(B_x - jH_z\mu)\tilde{\xi}_1\coth k\delta + \frac{\mu(B_x + jH_z\mu)\tilde{\xi}_2}{\sinh k\delta}\right]}{\mu(\mu^2 + \mu_o^2 + 2\mu\mu_o\coth k\delta)} \tag{4.78}$$

$$\tilde{\psi}_c = -\frac{(\mu - \mu_o)\left[(B_x + jH_z\mu)\mu_o\tilde{\xi}_2 + \mu(B_x + jH_z\mu)\tilde{\xi}_2\coth k\delta + \frac{\mu(B_x - jH_z\mu)\tilde{\xi}_1}{\sinh k\delta}\right]}{\mu(\mu^2 + \mu_o^2 + 2\mu\mu_o\coth k\delta)} \tag{4.79}$$

$$\tilde{\psi}_d = \frac{\frac{(\mu - \mu_o)}{\sinh k\delta}\left[(-B_x + jH_z\mu)\mu_o\tilde{\xi}_1 + (B_x - jH_z\mu)\mu_o\tilde{\xi}_2\cosh k\delta + (B_x\mu - jH_z\mu_o^2)\tilde{\xi}_2\sinh k\delta\right]}{\mu_o(\mu^2 + \mu_o^2 + 2\mu\mu_o\coth k\delta)}. \tag{4.80}$$

Interfacial Force Balance

A force balance at the upper and lower interfaces takes the general form

$$(p_a - p_b)\, n_{1i} = (T_{ija} - T_{ijb})\, n_{1j} - \sigma\, \vec{\nabla} \cdot \vec{n_1}\, n_{1i} \tag{4.81}$$

$$(p_c - p_d)\, n_{2i} = (T_{ijc} - T_{ijd})\, n_{2j} - \sigma\, \vec{\nabla} \cdot \vec{n_2}\, n_{2i}. \tag{4.82}$$

Each of these terms must be expressed as a function of $\tilde{\xi}_1$ and $\tilde{\xi}_2$. Beginning with the pressure terms we combine (4.58) with (4.48) and (4.49) to get

$$\tilde{p}_a = \frac{-\rho_o \omega^2}{k} \tilde{\xi}_1 \tag{4.83}$$

$$\tilde{p}_b = \frac{-\rho(\omega - kU)^2}{k} \left[-\tilde{\xi}_1 \coth k\delta + \frac{\tilde{\xi}_2}{\sinh k\delta} \right] \tag{4.84}$$

$$\tilde{p}_c = \frac{-\rho(\omega - kU)^2}{k} \left[-\tilde{\xi}_1 \sinh k\delta + \frac{\tilde{\xi}_2}{\coth k\delta} \right] \tag{4.85}$$

$$\tilde{p}_d = \frac{\rho_o \omega^2}{k} \tilde{\xi}_2. \tag{4.86}$$

Moving next to the magnetic stress tensor terms, the x-component of the first term on the right hand side of (4.81) and (4.82) is expanded as

$$T_{xj} n_j = T_{xx} n_x + T_{xy} n_y + T_{xz} n_z \tag{4.87}$$

for which T_{xy} is zero since $H_y = h_y = 0$. Considering only first-order terms, (4.87) can be written in terms of complex amplitudes at either interface in the form

$$\tilde{T_{xj}} n_j = \mu \left(H_x \tilde{h}_x - H_z \tilde{h}_z \right) + \mu H_x H_z j k \tilde{\xi}. \tag{4.88}$$

It is important to note that the '~' is over the entire term $\tilde{T_{xj}} n_j$ because there can be a small signal complex amplitude contribution from either the stress tensor or the interface normal.

The jump in magnetic stress can then be written for the upper and lower interfaces as

$$\left(\tilde{T_{xja}} - \tilde{T_{xjb}}\right) n_j = B_x \left(\tilde{h}_{xa} - \tilde{h}_{xb}\right) - H_z \left(\mu_o \tilde{h}_{za} - \mu \tilde{h}_{zb}\right) \tag{4.89}$$

$$\left(\tilde{T_{xjc}} - \tilde{T_{xjd}}\right) n_j = B_x \left(\tilde{h}_{xc} - \tilde{h}_{xd}\right) - H_z \left(\mu \tilde{h}_{zc} - \mu_o \tilde{h}_{zd}\right). \tag{4.90}$$

Finally, we note that the surface tension terms in (4.81) and (4.82) depend on $\vec{\nabla} \cdot \vec{n} = k^2 \tilde{\xi}$. Substituting the terms for pressure, magnetic stress, and surface tension back into (4.81) and (4.82) requires that

$$\tilde{p}_a - \tilde{p}_b = B_x \left(\tilde{h}_{xa} - \tilde{h}_{xb}\right) - H_z \left(\mu_o \tilde{h}_{za} - \mu \tilde{h}_{zb}\right) - \sigma k^2 \tilde{\xi}_1 \tag{4.91}$$

$$\tilde{p}_c - \tilde{p}_d = B_x \left(\tilde{h}_{xc} - \tilde{h}_{xd}\right) - H_z \left(\mu \tilde{h}_{zc} - \mu_o \tilde{h}_{zd}\right) - \sigma k^2 \tilde{\xi}_2. \tag{4.92}$$

Dispersion Relations

Writing all the terms of (4.91) as a function of $\tilde{\xi}_1$ and $\tilde{\xi}_2$ gives the relationship at the upper interface

$$\begin{aligned} & \tilde{\xi}_1 \left[\frac{\rho_o \omega^2}{k} + \frac{\rho}{k}(\omega - kU)^2 \coth k\delta - \sigma k^2 \right. \\ + \quad & \left. \frac{k(\mu - \mu_o)^2}{\sinh k\delta} \left(\frac{(B_x^2 - H_z \mu^2)\mu_o \cosh k\delta + \mu(B_x^2 - H_z^2 \mu_o^2) \sinh k\delta}{\mu \mu_o (\mu^2 + \mu_o^2 + 2\mu\mu_o \coth k\delta)} \right) \right] \\ + \quad & \tilde{\xi}_2 \left[\frac{-\rho(\omega - kU)^2}{k \sinh k\delta} - \frac{k(\mu - \mu_o)^2}{\sinh k\delta} \frac{(B_x + j\mu H_z)^2}{\mu(\mu^2 + \mu_o^2 + 2\mu\mu_o \coth k\delta)} \right] = 0. \end{aligned} \tag{4.93}$$

The corresponding relationship at the lower interface is derived by writing (4.92) in terms of $\tilde{\xi}_1$ and $\tilde{\xi}_2$

$$\begin{aligned} & \tilde{\xi}_2 \left[\frac{\rho_o \omega^2}{k} + \frac{\rho}{k}(\omega - kU)^2 \coth k\delta - \sigma k^2 \right. \\ + \quad & \left. \frac{k(\mu - \mu_o)^2}{\sinh k\delta} \left(\frac{(B_x^2 - H_z \mu^2)\mu_o \cosh k\delta + \mu(B_x^2 - H_z^2 \mu_o^2) \sinh k\delta}{\mu \mu_o (\mu^2 + \mu_o^2 + 2\mu\mu_o \coth k\delta)} \right) \right] \\ + \quad & \tilde{\xi}_1 \left[\frac{-\rho(\omega - kU)^2}{k \sinh k\delta} - \frac{k(\mu - \mu_o)^2}{\sinh k\delta} \frac{(B_x - j\mu H_z)^2}{\mu(\mu^2 + \mu_o^2 + 2\mu\mu_o \coth k\delta)} \right] = 0. \end{aligned} \tag{4.94}$$

These equations may be written more simply as

$$A_1\tilde{\xi}_1 + A_2\tilde{\xi}_2 = 0 \tag{4.95}$$

$$A_2^*\tilde{\xi}_1 + A_1\tilde{\xi}_2 = 0 \tag{4.96}$$

where A_2^* is the complex conjugate of A_2, meaning that all j are replaced by $-j$. Solving either (4.95) or (4.96) for the ratio of interfacial deflections produces

$$\frac{\tilde{\xi}_1}{\tilde{\xi}_2} = \frac{-A_2}{A_1} = \frac{-A_1}{A_2^*} \tag{4.97}$$

which has the solution

$$A_1^2 = |A_2|^2 \rightarrow A_1 = \pm|A_2|. \tag{4.98}$$

Using (4.98) in (4.95) or (4.96) produces the relationship

$$\frac{\tilde{\xi}_1}{\tilde{\xi}_2} = \mp\frac{A_2}{|A_2|} = \mp\frac{|A_2|}{A_2^*}. \tag{4.99}$$

If A_2 is real, as is true in the four cases $B_x = 0$, $H_z = 0$, $B_x \neq 0$ but $H_z = 0$, and $B_x = 0$ but $H_z \neq 0$, then

$$\frac{\tilde{\xi}_1}{\tilde{\xi}_2} = \mp 1. \tag{4.100}$$

However, if A_2 is complex, as in the case for an oblique applied magnetic field, $B_x \neq 0$ and $H_z \neq 0$, then the ratio of interfacial deflections, $\tilde{\xi}_1/\tilde{\xi}_2$, is a complex number, so that there will be a phase difference between the upper and lower interfacial deflections.

Case 1: $B_x = H_z = 0$

As a check of our result we set $B_x = H_z = 0$ in (4.93) and (4.94) and then obtain the classic fluid mechanic result found previously by Squire [40] and Villermaux and Clanet [38].

Combining (4.93)-(4.98) gives

$$\frac{\rho_o\omega^2}{k} + \frac{\rho(\omega - kU)^2}{k}\left(\coth k\delta \pm \frac{1}{\sinh k\delta}\right) - \sigma k^2 = 0 \tag{4.101}$$

where the + sign corresponds to $\tilde{\xi}_1 = -\tilde{\xi}_2$, and the − sign corresponds to $\tilde{\xi}_1 = \tilde{\xi}_2$.

As shown in (4.100), when $B_x = H_z = 0$ both A_1 and A_2 are real, so that $A_2 = A_2^*$. The only two wave modes possible are the symmetric mode of displacement, $\tilde{\xi}_1 = -\tilde{\xi}_2$, and the anti-symmetric mode of displacement, $\tilde{\xi}_1 = \tilde{\xi}_2$, both shown in Figure 4.6. Treating the symmetric case when $\tilde{\xi}_1 = -\tilde{\xi}_2$ we have

$$\frac{\rho_o\omega^2}{k} + \frac{\rho(\omega - kU)^2}{k}\left(\coth k\delta + \frac{1}{\sinh k\delta}\right) - \sigma k^2 = 0 \tag{4.102}$$

which is a simple quadratic equation in ω. Using the identity $\left(\coth k\delta + \frac{1}{\sinh k\delta}\right) = \coth\frac{k\delta}{2}$ and solving for ω produces

$$\omega = \frac{2\rho kU\coth\frac{k\delta}{2} \pm \sqrt{\left(2\rho kU\coth\frac{k\delta}{2}\right)^2 - 4\left(\rho_o + \rho\coth\frac{k\delta}{2}\right)\left(\rho k^2U^2\coth\frac{k\delta}{2} - \sigma k^3\right)}}{2\left(\rho_o + \rho\coth\frac{k\delta}{2}\right)}. \tag{4.103}$$

Instability occurs when the term under the square root is negative. The incipience of instability occurs when this term is zero, or equivalently

$$\left(\rho kU\coth\frac{k\delta}{2}\right)^2 - \left(\rho_o + \rho\coth\frac{k\delta}{2}\right)\left(\rho k^2U^2\coth\frac{k\delta}{2} - \sigma k^3\right) = 0. \tag{4.104}$$

Using the Weber number as defined in (4.3) and defining $\rho_r = \frac{\rho_o}{\rho}$, (4.104) reduces to

$$We = \frac{k\delta}{\rho_r}\left[\rho_r\tanh\frac{k\delta}{2} + 1\right]. \tag{4.105}$$

Since there is a wavenumber, k, that will satisfy this equation for all $We \geq 0$, all non-zero We have a range of k that are unstable. However, Squire states, 'An investigation

of the symmetrical disturbances...showed that long waves of this type are unstable. The degree of instability was, however, found to be very much less than for the anti-symmetrical disturbances...' [40]. For this reason we now focus on the conditions for instability of the anti-symmetric mode, $\tilde{\xi}_1 = \tilde{\xi}_2$. For this case the dispersion relation of (4.98) is

$$\frac{\rho_o \omega^2}{k} + \frac{\rho(\omega - kU)^2}{k}\left(\coth k\delta - \frac{1}{\sinh k\delta}\right) - \sigma k^2 = 0. \tag{4.106}$$

Using the identity that $\left(\coth k\delta - \dfrac{1}{\sinh k\delta}\right) = \tanh\dfrac{k\delta}{2}$ we solve the quadratic equation for ω as

$$\omega = \frac{2\rho kU \tanh\frac{k\delta}{2} \pm \sqrt{\left(2\rho kU \tanh\frac{k\delta}{2}\right)^2 - 4\left(\rho_o + \rho\tanh\frac{k\delta}{2}\right)\left(\rho k^2U^2\tanh\frac{k\delta}{2} - \sigma k^3\right)}}{2\left(\rho_o + \rho\tanh\frac{k\delta}{2}\right)}. \tag{4.107}$$

The onset of instability occurs when

$$\left(\rho kU\tanh\frac{k\delta}{2}\right)^2 - \left(\rho_o + \rho\tanh\frac{k\delta}{2}\right)\left(\rho k^2U^2\tanh\frac{k\delta}{2} - \sigma k^3\right) = 0. \tag{4.108}$$

Again rewriting this in terms of the Weber number and the density ratio, $\rho_r = \dfrac{\rho_o}{\rho}$, gives

$$We = \frac{k\delta}{\rho_r}\left[\rho_r \coth\frac{k\delta}{2} + 1\right]. \tag{4.109}$$

For real $k \geq 0$, the minimum value of We is 2, at $k\delta = 0$. Therefore, for 0 □ We □ 2 there is no solution for $k\delta$ and the mode is stable. Yet, for $We > 2$ the mode is unstable for a range of wavenumbers.

Case 2: $B_x \neq 0, H_z = 0$

As shown in (4.100), when $H_z = 0$ the condition $A_2 = A_2^*$ is met and again only two wave modes are possible, the symmetric ($\tilde{\xi}_1 = -\tilde{\xi}_2$) and anti-symmetric ($\tilde{\xi}_1 = \tilde{\xi}_2$) modes. To

model the experiments described in section 4.2.4 containing only a magnetic field directed perpendicularly to the ferrofluid layer we set $H_z = 0$ and obtain the dispersion relation

$$\begin{aligned} \frac{\rho_o\omega^2}{k} + \frac{\rho(\omega - kU)^2}{k}\left(\coth k\delta \pm \frac{1}{\sinh k\delta}\right) - \sigma k^2 \\ + \frac{k(\mu-\mu_o)^2 B_x^2\left[\cosh k\delta + \frac{\mu}{\mu_o}\sinh k\delta \pm 1\right]}{\mu \sinh k\delta(\mu^2 + \mu_o^2 + 2\mu\mu_o \coth k\delta)} &= 0 \end{aligned} \tag{4.110}$$

in which the upper + signs correspond to $\tilde{\xi}_1 = -\tilde{\xi}_2$, and the lower − signs correspond to $\tilde{\xi}_1 = \tilde{\xi}_2$. Assuming first that $\tilde{\xi}_1 = -\tilde{\xi}_2$ the dispersion relation is

$$\frac{\rho_o\omega^2}{k} + \frac{\rho(\omega - kU)^2}{k}\left(\coth\frac{k\delta}{2}\right) - \sigma k^2 + \frac{k(\mu-\mu_o)^2 B_x^2\left[\cosh k\delta + \frac{\mu}{\mu_o}\sinh k\delta + 1\right]}{\mu \sinh k\delta(\mu^2 + \mu_o^2 + 2\mu\mu_o \coth k\delta)} = 0. \tag{4.111}$$

This quadratic equation can be solved for ω with the result

$$\omega = \frac{\rho kU \coth\frac{k\delta}{2} \pm \sqrt{\left(\rho kU \coth\frac{k\delta}{2}\right)^2 - \left(\rho_o + \rho\coth\frac{k\delta}{2}\right)(f_1)}}{\left(\rho_o + \rho\coth\frac{k\delta}{2}\right)} \tag{4.112}$$

$$f_1 = \rho k^2 U^2 \coth\frac{k\delta}{2} - \sigma k^3 + \frac{k^2(\mu-\mu_o)^2 B_x^2\left[\cosh k\delta + \frac{\mu}{\mu_o}\sinh k\delta + 1\right]}{\mu\sinh k\delta\,(\mu^2 + \mu_o^2 + 2\mu\mu_o\coth k\delta)}. \tag{4.113}$$

The onset of instability occurs when the term under the square root in (4.112) is zero, or explicitly when

$$\left(\rho kU\coth\frac{k\delta}{2}\right)^2 = \left(\rho_o + \rho\coth\frac{k\delta}{2}\right)(f_1). \tag{4.114}$$

Next we consider the situation when $\tilde{\xi}_1 = \tilde{\xi}_2$ with the dispersion relation derived from (4.98) as

$$\frac{\rho_o\omega^2}{k} + \frac{\rho(\omega - kU)^2}{k}\left(\tanh\frac{k\delta}{2}\right) - \sigma k^2 + \frac{k(\mu-\mu_o)^2 B_x^2\left[\cosh k\delta + \frac{\mu}{\mu_o}\sinh k\delta - 1\right]}{\mu \sinh k\delta(\mu^2 + \mu_o^2 + 2\mu\mu_o \coth k\delta)} = 0. \tag{4.115}$$

Solving this quadratic for ω produces

$$\omega = \frac{\rho kU \tanh\frac{k\delta}{2} \pm \sqrt{\left(\rho kU \tanh\frac{k\delta}{2}\right)^2 - \left(\rho_o + \rho\tanh\frac{k\delta}{2}\right)(f_2)}}{\left(\rho_o + \rho\tanh\frac{k\delta}{2}\right)} \tag{4.116}$$

$$f_2 \;=\; \rho k^2 U^2 \tanh\frac{k\delta}{2} - \sigma k^3 + \frac{k^2(\mu-\mu_o)^2 B_x^2\left[\cosh k\delta + \frac{\mu}{\mu_o}\sinh k\delta - 1\right]}{\mu \sinh k\delta\,(\mu^2+\mu_o^2+2\mu\mu_o\coth k\delta)}. \quad (4.117)$$

The onset of instability occurs when the square root term in (4.116) is zero, explicitly written as

$$\left(\rho k U \tanh\frac{k\delta}{2}\right)^2 = \left(\rho_o + \rho\tanh\frac{k\delta}{2}\right)(f_2). \quad (4.118)$$

It is clear from (4.112) and (4.116) that increasing the magnetic field, B_x, destabilizes both the symmetric and anti-symmetric modes. The destabilization would transition the sheet from the smooth regime to the flapping regime, inducing surface roughening and a decrease in sheet radius, in qualitative agreement with the experimental observations presented.

Due to the constraints of the magnet size and test cell size only a narrow range of flow parameters could be investigated for the case of a magnetic field perpendicular to the sheet flow. Further work should include an increase of the parameters tested.

4.3 Discussion

An experimental investigation into the behavior of ferrofluid jet and sheet flows in the presence of magnetic fields has been presented. Vertical laminar jets of elliptical cross-section, imposed either by an elliptical nozzle with non-magnetic liquids or a magnetic field transverse to a ferrofluid jet, are found to lead to new and interesting sheet flows when striking a flat, horizontal impacting surface. In particular, a ferrofluid jet of initially circular cross-section will be deformed such that the cross-section will lengthen in the direction of a magnetic field applied perpendicular to the jet axis. As such the ferrofluid jet, now of elliptical cross-section, will give rise to a sheet of elliptical cross-section after impact. However, the cross-section of the sheet and jet are oriented perpendicularly to each other, a so called flip-flop. The

flip-flop between the long axis of the cross-section of the incident jet and the sheet flow off the impactor is qualitatively explained using jet oscillation theory with surface tension and inertia as the two dynamic forces. Such elliptical sheets are reproduced using non-magnetic liquid jets issuing from an elliptical orifice and then impacting the solid plate. Furthermore, the flip-flop behavior was reproduced in a hydraulic jump setup with a non-magnetic liquid, showing that the phenomenon is not limited to sheet flows, but is likely present in many situations involving the impact of a jet of non-circular cross-section.

Finally, we have presented experimental evidence of a perpendicular magnetic field enhanced Kelvin-Helmholtz instability with ferrofluid sheet flows. Specifically, a ferrofluid sheet is made to transition from a smooth regime to a flapping regime by application of a magnetic field perpendicular to the sheet at all points. In this situation the surface waves are destabilized, leading to a decrease in sheet diameter and a roughening of the sheet edges. Further work should entail accurate measurement and calculation of the growth rate of the instability in the magnetic field enhanced flapping regime, so as to compare directly with the presented Kelvin-Helmholtz theory. Additionally, theoretical examination of the sheet dynamics under the influence of a tangential magnetic field should be investigated, as well as the case of an oblique magnetic field relative to the sheet flow.

The results of this chapter may be applied to the control and deformation of ferrofluid jets used in printing processes. Also, the results may provide insight into processes requiring the coating of materials with thin ferrofluid layers. Another useful experiment would be to examine ferrofluid hydraulic jumps to determine if the jump characteristics, such as radius and height, can be controlled magnetically. Lastly, although only mentioned briefly here, the breakup of fluid sheets into droplets has been studied by previous investigators. Application

of a magnetic field in the experiments described herein may alter the shape and size of the droplets, which may have potential applications to printing and similar fields. A study focusing on the breakup of ferrofluid sheets into droplets would thus be appropriate.

Chapter 5

Concluding Remarks

This thesis has focused on three experimental investigations: ferrofluid characterization through magnetization measurements, ferrofluid tube and channel flow, and ferrofluid free surface flows in the form of jets and sheets.

Ferrofluids may be characterized by measuring the fluid magnetization as a function of magnetic field. Values of saturation magnetization and magnetic volume fraction can be easily and accurately derived from these measurements. The particle diameter range can be estimated by analysis of the linear and saturation magnetization regimes. The accuracy of the diameter values was not better than 1 nm, however, and it is recommended that for higher accuracy a direct imaging method also be used, such as electron microscopy. The geometrical demagnetizing factor of the ferrofluid samples was not able to be determined with reasonable accuracy from the experimental measurements, although several methods for doing so are presented and may be useful in experiments that demonstrate greater accuracy than those included here. Theoretical means of determining the demagnetizing effect are currently recommended.

The experiments of ferrofluid flow through tubing and open channel systems indicate

that ferrofluid may aid in mixing processes, and that in general ferrofluid flow is controllable through the application of static and oscillatory external magnetic fields. Spatially uniform, and spatially symmetrical magnetic fields do not raise or lower the pressure drop across a length of ferrofluid tube flow. However, non-symmetrical fields can readily create pressure increases and decreases. Magnetic fields that are spatially non-uniform are likely better at producing a net volume flux than are spatially uniform fields, which induce flow through magnetic torque and which were found to create a zero net flux. Future work should investigate a wider range of magnetic field geometries, frequencies, magnitudes, and directions in determining whether ferrofluids can be pumped without the aid of mechanical parts.

Ferrofluid dynamics have been examined experimentally and shown to produce non-intuitive and novel results in the form of ferrofluid jets and sheets of magnetically controllable size and shape. The sheet flows may be transferred from the smooth regime to the flapping regime by application of a magnetic field oriented perpendicularly to the sheet surface. The circular sheets may further be deformed to elliptical, or lens-like, shapes by application of a magnetic field tangential to the sheet flow. This change in sheet shape is driven by a magnetic field induced change in the shape of the incident jet. Also noteworthy is the apparent flip-flop between the cross-section of an impacting elliptical jet and the cross-section of the flow after impact. This behavior was documented not only for magnetic field induced elliptical ferrofluid sheets, but also for elliptical non-magnetic sheets, jets, and hydraulic jumps.

Looking forward, ferrofluids still possess many dynamics not fully explained here which warrant further investigation for the purpose of increasing the knowledge base of the fluids, as well as for potential applications. Of particular interest should be the relationship between wall effects and ferrofluid flow influenced by rotating and oscillating magnetic fields. It is

likely that the ferrofluid particles can be set into rotating motion, so that when in contact with a solid surface they create a flow along the surface wall. Effective design of channel systems may thus lead to complex and useful flow behavior. Control and analysis of ferrofluid jets and droplet size may also prove insightful to industries including printing, watermarking, and spray theory. Due to the small size of the ferrofluid particles many of the potential applications listed could have applications to MEMS and NEMS devices.

Appendix A

Magnetization Plots of Ferrofluid Samples

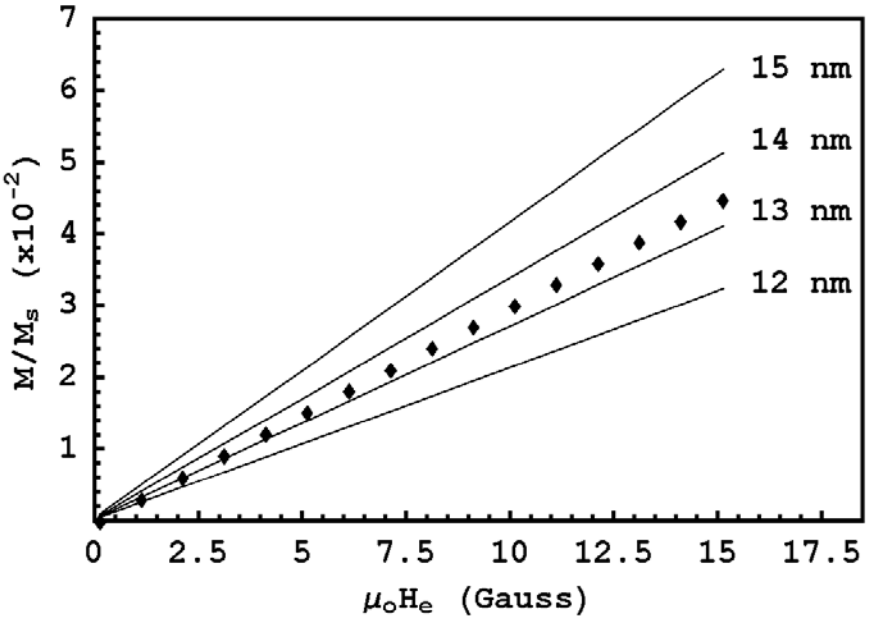

Figure A.1: Theoretical Langevin fit of measured NF 1273 wax ferrofluid low-field magnetization data for various particle sizes using $D = 0.211$. Data (diamonds) taken at 26.7^o C indicates a best-fit largest particle diameter of d_{max} ~13 nm.

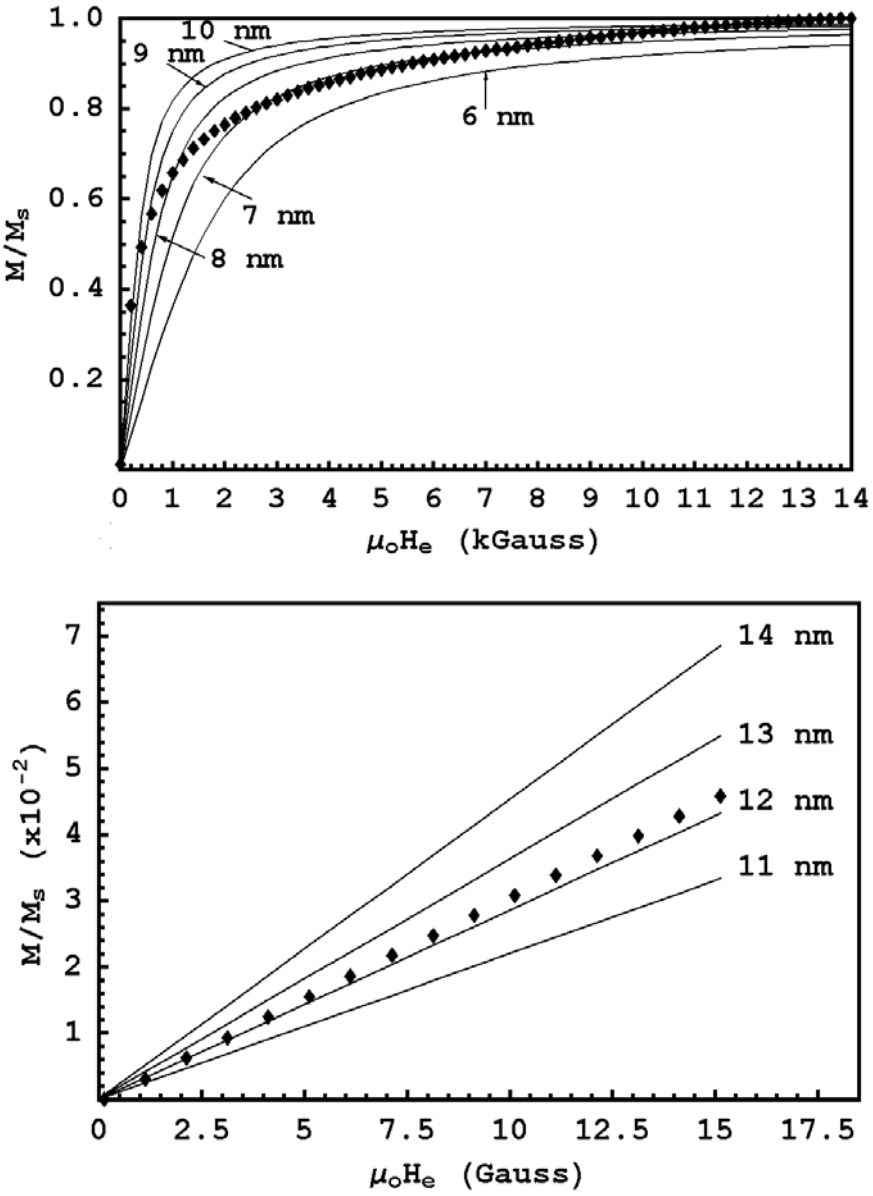

Figure A.2: (Top) Theoretical Langevin fit of measured MSG W11 water-based ferrofluid high-field magnetization data for various particle sizes using $D = 0.211$. Data (diamonds) taken at 26.3^o C indicates a best-fit average particle diameter of d_{avg} ∼8 nm. (Bottom) Theoretical Langevin fit of measured MSG W11 water-based ferrofluid low-field magnetization data for various particle sizes using $D = 0.211$. Data (diamonds) taken at 26.2^o C indicates a best-fit largest particle diameter of d_{max} ∼12 nm.

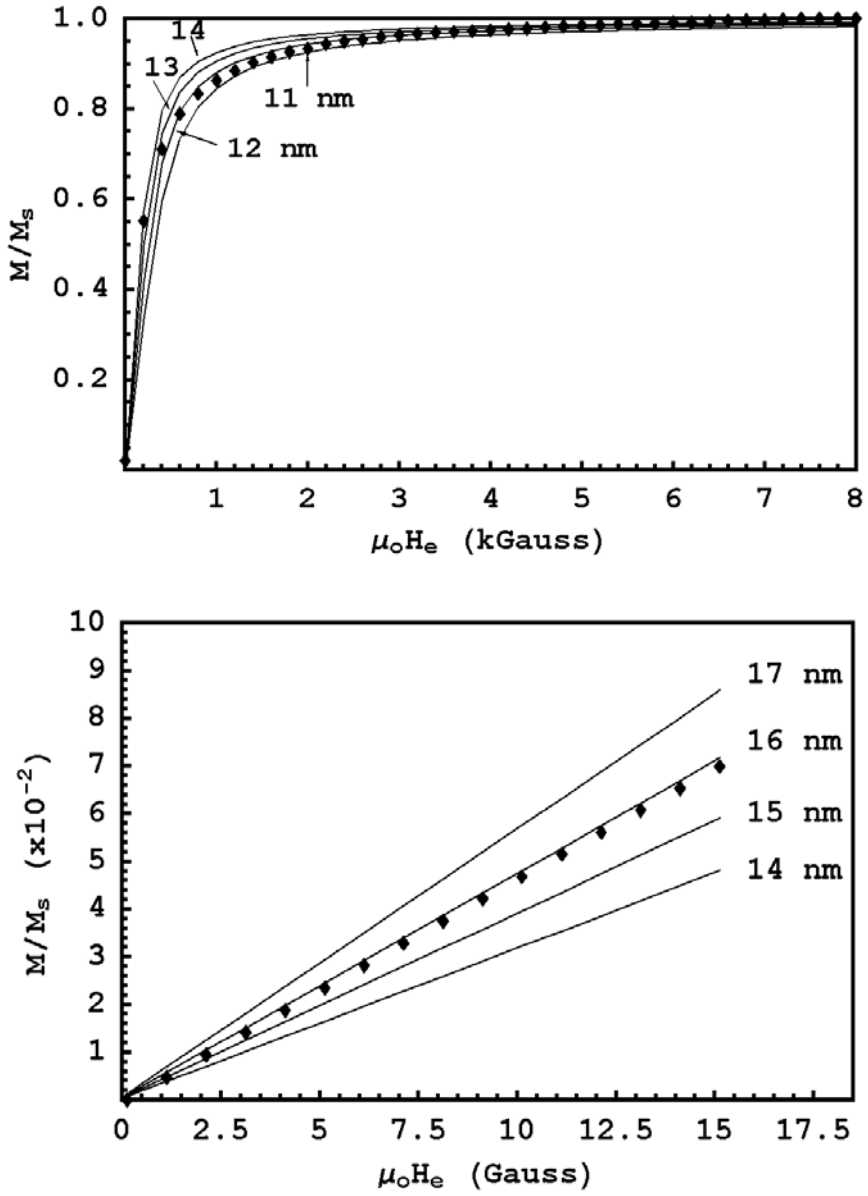

Figure A.3: (Top) Theoretical Langevin fit of measured NBF 1677 display cell ferrofluid high-field magnetization data for various particle sizes using $D = 0.211$. Data (diamonds) taken at 50.2^o C indicates a best-fit average particle diameter of d_{avg} ∼13 nm. (Bottom) Theoretical Langevin fit of measured NBF 1677 display cell ferrofluid low-field magnetization data for various particle sizes using $D = 0.211$. Data (diamonds) taken at $26.4\ ^o$ C indicates a best-fit largest particle diameter of d_{max} ∼16 nm.

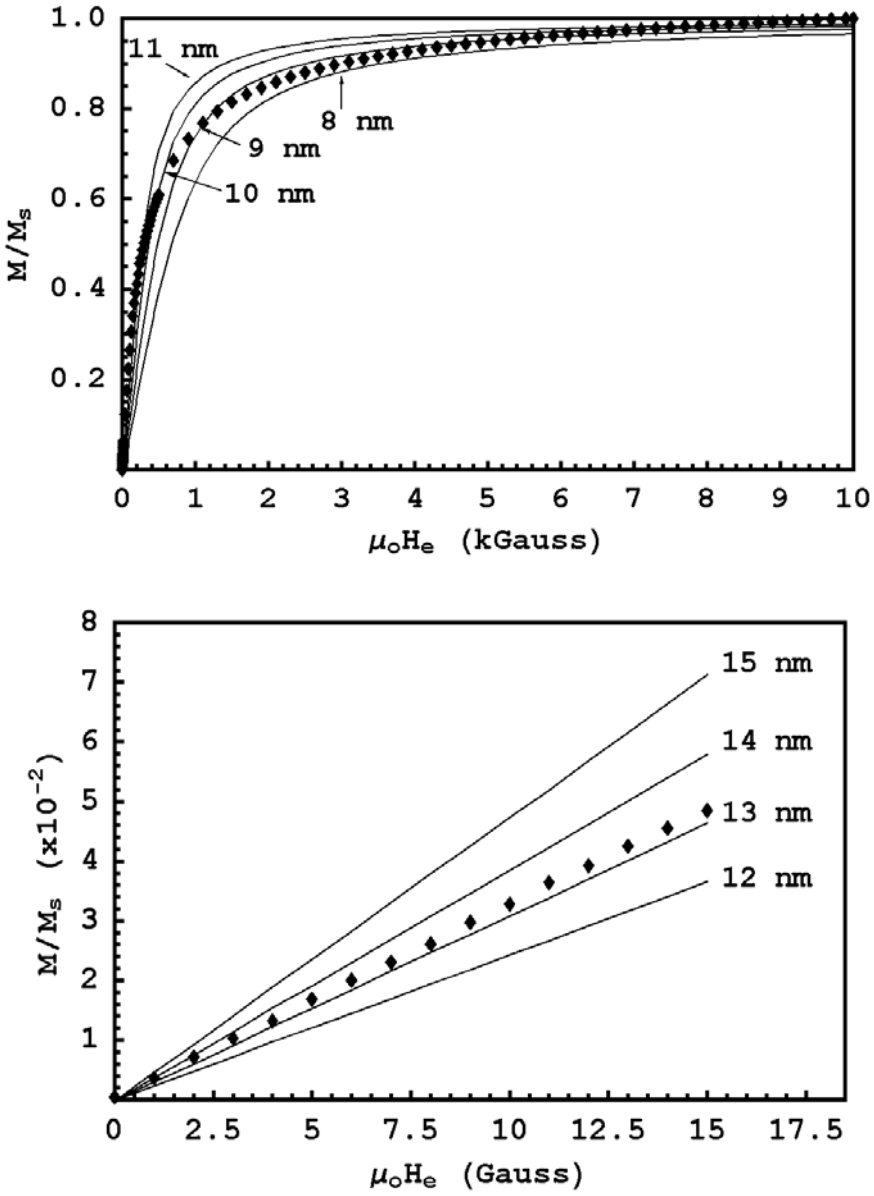

Figure A.4: (Top) Theoretical Langevin fit of measured EFH1 hydrocarbon-based ferrofluid high-field magnetization data for various particle sizes using $D = 0.211$. Data (diamonds) indicates a best-fit average particle diameter of d_{avg} ∼11 nm. (Bottom) Theoretical Langevin fit of measured EFH1 hydrocarbon-based ferrofluid low-field magnetization data for various particle sizes using $D = 0.211$. Data (diamonds) indicates a best-fit largest particle diameter of d_{max} ∼13 nm. Both trials were done at room temperature.

Appendix B

Experimental Procedures

B.1 Brookfield Viscometer Measurement Procedure

Adapted from Brookfield Viscometer Manual # M/92-021-L1199 [28, p. 13]

1. Mount the guard leg on the DV-I+ Viscometer (LV and RV series). Attach the spindle to the lower shaft. Lift the shaft slightly, holding it firmly with one hand while screwing the spindle on with the other. Avoid putting side thrust on the shaft.

2. Insert and center spindle in the test material until the fluid's level is at the immersion groove in the spindle's shaft. With a disc-type spindle, it is sometimes necessary to tilt the spindle slightly while immersing to avoid trapping air bubbles on its surface.

3. To make a viscosity measurement, select the desired speed setting. Allow time for the indicated reading to stabilize. The time required for stabilization will depend on the speed at which the viscometer is running and the characteristics of the sample fluid. For maximum accuracy, readings below 10% of maximum torque should be avoided.

B.2 Cannon-Fenske Opaque Viscometer Procedure

Taken from the instrument data sheets provide by VWR International.

1. If there is a possibility of lint, dust, or other solid materials in the liquid sample, filter the sample through a fine screen mesh.

2. To charge the sample into the viscometer, invert the instrument and apply suction to tube G, immersing tube A in the liquid sample, and draw liquid into the capillary F. Adjust liquid to mark E, turn the instrument to its normal vertical position and wipe clean.

3. Align the viscometer vertically in the bath, if a self aligning holder is not used. When the liquid begins to fill bulb B, stop the flow by plugging tube A.

4. Allow approximately 10 minutes for the sample to come to the bath temperature at 40^oC and 15 minutes at 100^oC.

5. To measure efflux time, remove plug from tube A and measure the time for the leading edge of the meniscus to pass from mark H to mark I. Using a second timer, measure the time required from mark I to mark J.

6. Calculate the kinematic viscosity of the sample in centiStokes by multiplying the efflux time for bulb C times the constant for the lower bulb.

7. Check the results by multiplying the efflux time for bulb D times the constant for the upper bulb.

B.3 Method of Propagation of Errors

Adapted from Taylor [50, jacket cover].

If q is the sum or difference of the various quantities $x, ... \ y, ...$and z with error $\delta x, \ \delta y, \ \delta z$

then

$$\delta q \begin{cases} = & \sqrt{(\delta x)^2 + ... + (\delta y)^2 + ... + (\delta z)^2} & \text{for independent random errors} \\ \square & \delta x + ... + \delta y + ... + \delta z & \text{always.} \end{cases}$$

If w is the product or quotient of the various quantities $x, ... \, y, ...$ and z with error $\delta x, \ \delta y, \ \delta z$ then

$$\frac{\delta w}{|w|} \begin{cases} = & \sqrt{(\frac{\delta x}{|x|})^2 + ... + (\frac{\delta y}{|y|})^2 + ... + (\frac{\delta z}{|z|})^2} & \text{for independent random errors} \\ \square & \frac{\delta x}{|x|} + ... + \frac{\delta y}{|y|} + ... + \frac{\delta z}{|z|} & \text{always.} \end{cases}$$

Appendix C

Experimental Tube Flow Data

C.1 Magnetic Field Tangential To Flow Direction

Pressure Drop vs. Flow rate for Tap Water		
Magnetic Field (Gauss)	**Q (L/min)**	**Δp (p.s.i.)**
0	0	0
	0.544	0.10
	0.793	0.19
	1.077	0.32
	1.329	0.48
	1.594	0.65
	1.881	0.87
	2.130	1.11
	2.393	1.37
	2.656	1.65
	2.929	1.98
	3.194	2.31

Pressure Drop vs. Flow rate for Tap Water (Cont'd.)		
Magnetic Field (Gauss)	**Q (L/min)**	**Δp (p.s.i.)**
50	0	0
	0.547	0.09
	0.799	0.17
	1.067	0.30
	1.327	0.46
	1.597	0.66
	1.870	0.89
	2.128	1.13
	2.401	1.41
	2.661	1.68
	2.937	2.01
	3.179	2.32
100	0	0
	0.541	0.08
	0.804	0.17
	1.072	0.31
	1.327	0.46
	1.592	0.66
	1.852	0.88
	2.114	1.13
	2.401	1.41
	2.664	1.67
	2.924	1.97
150	0	0
	0.554	0.09
	0.801	0.16
	1.072	0.30
	1.332	0.46
	1.602	0.65
	1.849	0.89
	2.120	1.13
	2.390	1.39
	2.659	1.68
	2.937	2.00
	3.173	2.29

Pressure Drop vs. Flow rate for Tap Water (Cont'd.)		
Magnetic Field (Gauss)	**Q (L/min)**	**Δp (p.s.i.)**
200	0	0
	0.539	0.09
	0.799	0.17
	1.059	0.30
	1.334	0.46
	1.592	0.67
	1.865	0.90
	2.133	1.13
	2.390	1.38
	2.656	1.67
	2.929	1.99
	3.186	2.32
250	0	0
	0.531	0.09
	0.801	0.18
	1.061	0.30
	1.340	0.46
	1.608	0.66
	1.852	0.87
	2.128	1.14
	2.390	1.39
	2.661	1.69
	2.924	1.99
	3.189	2.33

Pressure Drop vs. Flow rate for Tap Water (Cont'd.)		
Magnetic Field (Gauss)	**Q (L/min)**	**Δp (p.s.i.)**
300	0	0
	0.541	0.09
	0.801	0.18
	1.061	0.32
	1.332	0.47
	1.600	0.65
	1.852	0.87
	2.128	1.13
	2.396	1.4
	2.666	1.69
	2.916	1.98
	3.197	2.33

Table C.1: Pressure drop versus flow rate as a function of applied magnetic field for tap water. The magnetic field is applied tangential to the direction of flow, as described in section 3.3.1.

Pressure Drop vs. Flow rate for MSG W11		
Magnetic Field (Gauss)	**Q (L/min)**	**Δp (p.s.i.)**
0	0	0
	0.542	0.14
	0.807	0.25
	1.057	0.39
	1.335	0.58
	1.588	0.78
	1.861	1.11
	2.127	1.44
	2.400	1.80
	2.655	2.20
	2.923	2.64
	3.183	3.10
50	0	0
	0.539	0.13
	0.804	0.26
	1.065	0.40
	1.330	0.56
	1.598	0.79
	1.859	1.11
	2.127	1.44
	2.397	1.81
	2.650	2.20
	2.918	2.64
	3.205	3.15
100	0	0
	0.528	0.13
	0.804	0.26
	1.067	0.40
	1.325	0.57
	1.596	0.79
	1.864	1.11
	2.124	1.44
	2.387	1.81
	2.652	2.19
	2.934	2.66
	3.202	3.16

Pressure Drop vs. Flow rate for MSG W11 (Cont'd.)		
Magnetic Field (Gauss)	**Q (L/min)**	**Δp (p.s.i.)**
150	0	0
	0.555	0.15
	0.810	0.27
	1.070	0.41
	1.330	0.58
	1.588	0.79
	1.861	1.12
	2.121	1.45
	2.397	1.84
	2.663	2.24
	2.926	2.66
	3.197	3.15
200	0	0
	0.552	0.16
	0.804	0.27
	1.073	0.41
	1.341	0.60
	1.596	0.80
	1.856	1.11
	2.121	1.46
	2.397	1.84
	2.652	2.23
	2.918	2.68
	3.194	3.15
250	0	0
	0.539	0.14
	0.804	0.26
	1.057	0.40
	1.338	0.58
	1.593	0.80
	1.864	1.13
	2.124	1.46
	2.397	1.85
	2.652	2.22
	2.926	2.67
	3.186	3.16

Pressure Drop vs. Flow rate for MSG W11 (Cont'd.)		
Magnetic Field (Gauss)	**Q (L/min)**	**Δp (p.s.i.)**
300	0	0
	0.550	0.15
	0.810	0.27
	1.078	0.42
	1.328	0.59
	1.604	0.81
	1.864	1.13
	2.121	1.46
	2.384	1.83
	2.650	2.23
	2.934	2.70
	3.194	3.15

Table C.2: Pressure drop versus flow rate as a function of applied magnetic field for MSG W11 water-based ferrofluid. The magnetic field is applied tangential to the direction of flow, as described in section 3.3.1.

Pressure Drop vs. Flow rate for EFH1		
Magnetic Field (Gauss)	**Q (L/min)**	**Δp (p.s.i.)**
0	0	0
	0.500	0.25
	0.727	0.40
	0.996	0.61
	1.233	0.85
	1.467	1.12
	1.716	1.44
	1.958	1.75
	2.197	2.08
	2.451	2.49
	2.570	2.67
50	0	0
	0.493	0.26
	0.737	0.42
	0.991	0.62
	1.216	0.85
	1.455	1.12
	1.699	1.42
	1.967	1.78
	2.197	2.10
	2.451	2.50
	2.561	2.67
100	0	0
	0.496	0.28
	0.735	0.43
	0.986	0.64
	1.238	0.89
	1.455	1.15
	1.721	1.48
	1.970	1.83
	2.199	2.16
	2.456	2.54
	2.565	2.71

Pressure Drop vs. Flow rate for EFH1 (Cont'd.)		
Magnetic Field (Gauss)	**Q (L/min)**	**Δp (p.s.i.)**
150	0	0
	0.496	0.27
	0.730	0.42
	0.986	0.65
	1.228	0.90
	1.474	1.18
	1.711	1.48
	1.963	1.82
	2.204	2.18
	2.448	2.56
	2.556	2.71
200	0	0
	0.510	0.29
	0.737	0.44
	0.984	0.66
	1.242	0.91
	1.462	1.18
	1.584	1.33
	1.716	1.50
	1.963	1.87
	2.190	2.17
	2.451	2.59
	2.563	2.77
250	0	0
	0.505	0.29
	0.737	0.44
	0.979	0.66
	1.233	0.92
	1.469	1.20
	1.721	1.53
	1.960	1.87
	2.204	2.23
	2.434	2.59
	2.578	2.82

Pressure Drop vs. Flow rate for EFH1 (Cont'd.)		
Magnetic Field (Gauss)	**Q (L/min)**	**Δp (p.s.i.)**
300	0	0
	0.510	0.29
	0.742	0.46
	0.976	0.66
	1.238	0.93
	1.491	1.23
	1.716	1.53
	1.965	1.90
	2.209	2.26
	2.443	2.63
	2.587	2.85

Table C.3: Pressure drop versus flow rate as a function of applied magnetic field for EFH1 hydrocarbon-based ferrofluid. The magnetic field is applied tangential to the direction of flow, as described in section 3.3.1.

C.2 Magnetic Field Perpendicular to Flow Direction

Pressure Drop vs. Flow rate for MSG W11		
Magnetic Field (Gauss)	**Q (L/min)**	**Δp (p.s.i.)**
0	0	0
	0.563	0.21
	0.839	0.37
	1.094	0.56
	1.328	0.75
	1.598	1.04
	1.859	1.52
	2.124	1.97
	2.400	2.52
	2.671	3.06
100	0	0
	0.542	0.20
	0.815	0.35
	1.073	0.54
	1.341	0.76
	1.593	1.03
	1.874	1.51
	2.116	1.93
	2.384	2.45
	2.676	3.04

Pressure Drop vs. Flow rate for MSG W11 (Cont'd.)		
Magnetic Field (Gauss)	**Q (L/min)**	**Δp (p.s.i.)**
200	0	0
	0.560	0.21
	0.842	0.38
	1.094	0.56
	1.333	0.76
	1.601	1.04
	1.861	1.44
	2.135	1.96
	2.392	2.46
	2.668	3.04
300	0	0
	0.558	0.21
	0.810	0.36
	1.073	0.56
	1.335	0.77
	1.620	1.07
	1.872	1.43
	2.132	1.93
	2.390	2.44
	2.674	3.04
400	0	0
	0.558	0.20
	0.818	0.36
	1.075	0.55
	1.330	0.77
	1.598	1.04
	1.869	1.40
	2.121	1.87
	2.411	2.46
	2.666	3.01

Pressure Drop vs. Flow rate for MSG W11 (Cont'd.)		
Magnetic Field (Gauss)	**Q (L/min)**	**Δp (p.s.i.)**
525	0	0
	0.547	0.22
	0.839	0.39
	1.073	0.56
	1.330	0.78
	1.614	1.07
	1.888	1.44
	2.137	1.87
	2.400	2.44
	2.695	3.08
1040	0	0
	0.600	0.26
	0.826	0.40
	1.089	0.59
	1.351	0.82
	1.617	1.09
	1.885	1.44
	2.137	1.81
	2.379	unstable reading
	2.682	2.99
2050	0	0
	0.528	0.23
	0.855	0.44
	1.102	0.63
	1.322	0.84
	1.596	1.09
	1.872	1.44
	2.137	1.84
	2.371	2.22

Table C.4: Pressure drop versus flow rate for MSG W11 water-based ferrofluid as a function of applied magnetic field strength. The magnetic field is oriented perpendicular to the direction of flow, as described in section 3.3.2.

Pressure Drop vs. Flow rate for EFH1		
Magnetic Field (Gauss)	**Q (L/min)**	**Δp (p.s.i.)**
0	0	0
	0.498	0.44
	0.754	0.70
	0.984	0.96
	1.235	1.30
	1.477	1.67
	1.721	2.12
	1.989	2.62
	2.202	3.07
	2.439	3.58
100	0	0
	0.557	0.53
	0.786	0.74
	0.981	0.98
	1.230	1.31
	1.484	1.70
	1.723	2.15
	1.945	2.58
	2.214	3.11
	2.441	3.61
200	0	0
	0.566	0.54
	0.740	0.70
	0.996	1.00
	1.223	1.30
	1.460	1.67
	1.723	2.16
	1.972	2.65
	2.199	3.10
	2.468	3.70

Pressure Drop vs. Flow rate for EFH1 (Cont'd.)		
Magnetic Field (Gauss)	**Q (L/min)**	**Δp (p.s.i.)**
300	0	0
	0.500	0.46
	0.737	0.71
	0.959	0.98
	1.228	1.32
	1.469	1.73
	1.682	2.10
	1.967	2.66
	2.194	3.12
	2.463	3.72
400	0	0
	0.571	0.56
	0.742	0.74
	1.018	1.07
	1.235	1.37
	1.506	1.80
	1.689	2.15
	1.970	2.69
	2.197	3.15
	2.470	3.74
500	0	0
	0.539	0.53
	0.806	0.81
	0.967	1.01
	1.233	1.38
	1.484	1.78
	1.716	2.22
	1.958	2.69
	2.197	3.18
	2.436	3.70

Pressure Drop vs. Flow rate for EFH1 (Cont'd.)		
Magnetic Field (Gauss)	**Q (L/min)**	**Δp (p.s.i.)**
1040	0	0
	0.513	0.55
	0.737	0.78
	0.967	1.07
	1.228	1.42
	1.472	1.83
	1.709	2.28
	1.938	2.74
	2.197	3.26
	2.463	3.85
2030	0	0
	0.508	0.56
	0.810	0.93
	0.964	1.12
	1.233	1.50
	1.477	1.91
	1.731	2.41
	1.963	2.86
	2.192	3.36
	2.463	3.95

Table C.5: Pressure drop versus flow rate for EFH1 hydrocarbon-based ferrofluid as a function of applied magnetic field strength. The magnetic field is oriented perpendicular to the direction of flow, as described in section 3.3.2.

Appendix D

Unit Conversions

SI Prefixes		
Factor	**Prefix**	**Symbol**
10^{9}	giga	G
10^{6}	mega	M
10^{3}	kilo	k
10^{1}	deka	da
10^{-2}	centi	c
10^{-3}	milli	m
10^{-6}	micro	μ
10^{-9}	nano	n
10^{-12}	pico	p

Physical Constants			
Quantity	**Symbol**	**Value**	**Units**
Magnetic Permeability of Free Space	μ_o	$4\pi \times 10^{-7}$	H/m
Boltzmann Constant	k	1.38×10^{-23}	J/K

Basic Units of Common Quantities			
Quantity	**Unit**	**Abbreviation**	**Basic Units**
Time	second	s	s
Frequency	Hertz	Hz	s^{-1}
Mass	gram	g	g
Length	meter	m	m
Length	inch	in	in
Length	feet	ft	ft
Force	Newton	N	$kg - m/s^2$
Energy	Joule	J	$kg - m^2/s^2$
Torque	Newton-meter	N-m	$kg - m^2/s^2$
Pressure	Pascal	Pa	$kg/m - s^2$
Pressure	pound per square inch	p.s.i.	lbf/in^2
Dynamic Viscosity	centipoise	cP	g/cm-s
Dynamic Viscosity	Pascal second	Pa-s	$kg/m - s$
Temperature	kelvin	K	K
H	Oersted	Oe	A/m
B	Tesla	T	$kg/s^2 - A$
B	Gauss	G	$kg/s^2 - A$
Inductance	Henry		$kg - m^2/s^2 - A^2$
Magnetic Flux	Weber	Wb	$kg - m^2/s^2 - A$
Electrical Charge	Coulomb	C	C
Electrical Current	Ampere	A	C/s
Potential Difference	Volt	V	W/A
Power	Watt	W	$J/s = kg - m^2/s^3$

Conversions of General Mechanics				
Quantity	**Symbol**	**S.I.**	**cgs**	**English**
Length	l,L,r	1 m	100 cm	39.4 in
Velocity	v	$1 \frac{m}{s}$	100 cm/s	3.28 ft/s
Volume	V	$1\ m^3$	$10^6\ cm^3$	$35.3\ ft^3$
Mass	M	1 kg	1000 g	0.068 slug
Pressure	P	6895 Pa		$1 \frac{lbf}{in^2}$
Force	F	1 N		10^5 dyne

Conversions of Fluid Mechanics			
Quantity	**Symbol**	**S.I.**	**cgs**
Dynamic Viscosity	η	$1\ \frac{\mathrm{kg}}{\mathrm{m}-\mathrm{s}}$	$10\ \frac{\mathrm{g}}{\mathrm{cm}-\mathrm{s}}$ (poise)
Kinematic Viscosity	ν	$10^{-4}\frac{\mathrm{m}^2}{\mathrm{s}}$	$1\ \frac{\mathrm{cm}^2}{\mathrm{s}}$ (stoke)
Surface Tension	σ	1 N/m	10^3 dyne/cm
Volumetric Flux Rate	Q	$1\ \frac{\mathrm{m}^3}{\mathrm{s}}$	$10^6\frac{\mathrm{cm}^3}{\mathrm{s}}$

Conversions of Thermodynamics	
Quantity	**Equation**
Temperature	$^{\mathrm{o}}\mathrm{F} = {}^{\mathrm{o}}\mathrm{C} \times \frac{9}{5} + 32$
Temperature	$^{\mathrm{o}}\mathrm{C} = (^{\mathrm{o}}\mathrm{F} - 32) \times \frac{5}{9}$
Temperature	$\mathrm{k} = {}^{\mathrm{o}}\mathrm{C} + 273$

Bibliography

[1] Rosensweig, R. E., 1985. *Ferrohydrodynamics*, Dover Publications, Inc., Mineola, New York.

[2] Rosensweig, R. E., 2001. *Ferrofluids: Introduction*, Eds.: Buschow K. H. J., Cahn R. W., Flemings M. C., Ilschner B., Kramer E. J., Mahajan S., Encyclopedia of Materials: Science and Technology, Volume 4. Elsevier, Oxford, pp. 3093-3102.

[3] Xerox corporation. Website visited 2/8/2003. http://www.xipo.com

[4] Ziolo, R. F., Giannelis, E. P., Weinstein, B. A., O'Horo, M. P., Ganguly, B. N., Mehrotra, V., Russell, M. W., and Heiffman, D. R., 1992. Matrix-Mediated Synthesis of Nanocrystalline γ-Fe_2O_3: A New Optically Transparent Magnetic Material, *Science*, **257** (5067), 219-222.

[5] Pérez-Castillejos, R., Plaza, J. A., Esteve, J., Losantos, P., Acero, M.C., Can, C., and Serra-Mestres, F., 2000. The use of ferrofluids in micromechanics, *Sensors and Actuators*, **84**, 176-180.

[6] Bibik, E. E., Matgullin, B. Y., Raikher, Y. L., and Shliomis, M. I., 1973. The magnetostatic properties of colloidal magnetite, *Magnetohydrodynamics*, **9** (1), 58-62.

[7] Rosensweig, R. E., 1996. Negative Viscosity in a Magnetic Fluid, *Science*, **271**, 614-615.

[8] Zahn, M., and Wainman, P., 1993. Effects of fluid convection and particle spin on ferrohydrodynamic pumping in traveling wave magnetic fields, *Journal of Magnetism and Magnetic Materials*, **122**, 323-328.

[9] Cowley, M. D., and Rosensweig, R. E., 1967. The interfacial stability of a ferromagnetic fluid, *Journal of Fluid Mechanics*, **30** (4), 671-88.

[10] Rosensweig, R. E., Zahn, M., and Vogler, T., 1978. Stabilization of fluid penetration through a porous medium using a magnetizable fluid. *Thermomechanics of magnetic fluids*, B. Berkovsky, Ed., Hemisphere, Washington, D.C. 195-211.

[11] Zahn, M., and Rosensweig, R. E., 1980. Stability of magnetic fluid penetration through a porous medium with uniform magnetic field oblique to the interface. *IEEE Trans. Magnetics*, MAG-16 (2), 275-282.

[12] Rosensweig, R. E., Zahn, M., and Shumovich, R., 1983. Labyrinthine instability in magnetic and dielectric fluids. *J. Magnetism Magnetic Mater.*, **39** (1,2), 127-132.

[13] Zahn, M., Rosensweig, R. E., 1991. Magnetic and Dielectric Fluids in Porous Media. *Advances in Porous Media*, M. Corapcioglu, Ed., Elsevier, New York. 125-178.

[14] Lorenz, C., and Zahn, M., 2002. Hele-Shaw Ferrohydrodynamics for Rotating and Axial Magnetic Fields, presented at American Institute of Physics, Division of Fluid Dynamics 2002, Dallas, TX.

[15] Rosenthal, A., 2002. *Ferrofluid Flow and Torque Measurements in Rotating Magnetic Fields*, Master of Engineering Thesis for the Department of Electrical Engineering and Computer Science, Massachusetts Institute of Technology.

[16] Rosenthal, A. D., Rinaldi, C., Franklin, T., and Zahn, M., *Torque Measurements in Spin-Up Flow of Ferrofluids*, *Submitted to the Journal of Fluids Engineering January, 2003.*

[17] Lee, C. S., Lee, H., and Westervelt, R. M., 2001. Microelectromagnets for the control of magnetic nanoparticles, *Applied Physics Letters*, **79** (20), 3308-3310.

[18] Koser, H., Cros, F., Allen, M. G., and Lang, J. H., 2001. A high torque density MEMS magnetic induction machine, *International Conference on solid state sensors and actuators, Transducers, Munich, Germany*, 284-287.

[19] Energy International, Inc. May 2000 Phase I Final Report, Enhanced Cooling Using a Fluid Containing Magnetic Nanoparticles. Prepared for the National Science Foundation.

[20] Rinaldi, C. and Zahn, M., 2002. Effects of Spin Viscosity on Ferrofluid Duct Flow Profiles in Alternating and Rotating Magnetic Fields, *Journal of Magnetism and Magnetic Materials*, **252**, 172-175.

[21] The Merck Index 9th Ed., 1968. Merck & Company, Inc., Rahway, NJ.

[22] Zahn, M., 1979. *Electromagnetic Field Theory: a problem solving approach*, Krieger Publishing Company, Florida.

[23] Shliomis, M. I., 1974. Magnetic Fluids, *Phys-Usp*, **17** (2), 153-167.

[24] Onsager, L., 1936. Electric Moments of Molecules in Liquids, *Journal of the American Chemical Society*, **58**, 1486.

[25] Shen, L. F., Stachowiak, A., Fateen, S. E. K., Laibinis, P. E., and Hatton, T. A., 2001. Structure of alkanoic acid stabilized magnetic fluids. A small-angle neutron and light scattering analysis, *Langmuir*, **17**, 288-299.

[26] Bozorth, R. M., 1951. *Ferromagnetism*, IEEE Press, New York, 849.

[27] ADE Technologies, Inc., *Digital Measurement Systems Model 880 Vibrating Sample Magnetometer IBM PC Version Operating Manual*, Westwood, Massachusetts, 45.

[28] Brookfield Engineering Laboratories, Inc., *Digital Viscometer Model DV-I+ Operating Instructions Manual No. M/92-021-M0101*, Middleboro, Massachusetts.

[29] Roberson, J., and Crowe, C., *Engineering Fluid Mechanics*, 6th Edition, John Wiley & Sons, Inc., New York, 1997, 145.

[30] Personal communication with Brookfield Engineering Laboratories technician, Len Thibodeau. 8/30/02. Middleboro, Massachusetts.

[31] Batchelor, G. K., 1967. *An Introduction to Fluid Dynamics*, Cambridge University Press, Cambridge, 597.

[32] White, F. M., 1979. *Fluid Mechanics*, McGraw-Hill Book Company, New York, 310.

[33] Melcher, J. R., 1981. *Continuum Electromechanics*, The MIT Press, Cambridge, Massachusetts.

[34] Choi, Tae In, 1980. *Ferrofluid Motion In a Rotating Magnetic Field*, Thesis for the University of Florida Dept. of Electrical Engineering.

[35] Clanet, C., 2001. Dynamics and stability of water bells, *Journal of Fluid Mechanics*, **430**, 111-147.

[36] Taylor G. I., 1959. The dynamics of thin sheets of fluid I. Water Bells, *Proceedings of the Royal Society of London A*, **253**, 289-295.

[37] Clanet, C., and Villermaux, E., 2002. Life of a smooth liquid sheet, *Journal of Fluid Mechanics*, **462**, 307-340.

[38] Villermaux, E. and Clanet, C., 2002. Life of a Flapping Liquid Sheet, *Journal of Fluid Mechanics*, **462**, 341-363.

[39] Savart, F., 1833. Memoire sur le choc d'une veine liquide lancée contre un plan circulaire, *Ann. de chim*, **54**, 113-145.

[40] Squire, H. B., 1953. Investigation of the Instability of a Moving Liquid Film, *British Journal of Applied Physics*, **4**, 167-169.

[41] Taylor, G. I., 1959. The dynamics of thin sheets of fluid II. Waves on fluid sheets, *Proc. Roy. Soc. Lond. A*, **253**, 351-367.

[42] Buckingham, R. and Bush, J. W. M., 2001. Fluid Polygons, *Gallery of Fluid Motion, Physics of Fluids*, **12** (9).

[43] Tipler, P. A., 1991. *Physics: For Scientists and Engineers 3rd Ed.*, Worth Publishers, New York, New York.

[44] Bush, J. W. M., and Hasha, A., 2002. The collision of laminar jets: Fluid chains and fishbones, *Submitted to the Journal of Fluid Mechanics*.

[45] Shcherbinin, E. V., 1972. Elliptical Jets, *Magnitnaya-Gidrodinamika*, (2), 59-67.

[46] Griffiths, D. J., 1999. *Introduction to Electrodynamics*, Prentice Hall, New Jersey, 352.

[47] Strutt, J. W., Baron Rayleigh, 1945. *The Theory of Sound, Vol. II*, Dover Publications, New York.

[48] Bechtel, S. E., 1989. The Oscillation of Slender Elliptical Inviscid and Newtonian Jets: Effects of Surface Tension, Inertia, Viscosity, and Gravity, *Journal of Applied Mechanics*, **56**, 968-974.

[49] Melcher, James R., 1963 *Field-Coupled Surface Waves: A comparative study of surface-coupled electrohydrodynamic and magnetohydrodynamic systems*, MIT Press, Cambridge, Massachusetts.

[50] Taylor, J. R., 1997. *An Introduction to Error Analysis*, 2nd Edition, University Science Books Sausalito, California.